uc3m | Universidad Carlos III de Madrid

Bachelor's Degree in Aerospace Engineering
2016/2017

Bachelor's Thesis

Existence of Solitary Waves in the Hall-MHD model with Finite Larmor Radius effect

Enrique Bello Benítez

Advisor
Gonzalo Sánchez Arriaga

Contents

List of Figures

Chapter 1

Introduction

The Sun is the main celestial body in the Solar System and it is one of the principal players in many physical phenomena in the Earth, its surroundings and the nearby outer space. The Sun is made of gas, that becomes ionized due to the extremely high temperatures provoked by the nuclear fusion processes taking place in its core. This ionized gas is termed *plasma*. The solar plasma is not restricted to the surroundings of the Sun's core but its atmosphere extents up to more than 130 AU[1]. The solar atmosphere is composed of plasma escaping from the Sun which transports the Sun's magnetic field together with it. This flow of solar material is named *solar wind*. The solar wind and other phenomena with origin at the Sun —e.g. solar flares or coronal mass ejections— have detrimental effects on space probes, on astronauts or even at the Earth's surface level. Therefore, it is of paramount importance to understand the physics of the Sun —i.e. heliophysics— so that solar activity and other Sun-related events can be predicted and/or mitigated.

The project exposed in this thesis is performed in the context of better understanding the solar wind characteristics. To be precise, the subject of study is *magnetic holes*, which are events that have been measured in the solar wind by several space missions. The term *magnetic hole* was introduced by Turner et al. [3] in 1976 and they have been observed in the magnetosheaths of Earth, Saturn and Jupiter, in the surroundings of comet Halley and in the interplanetary solar wind. Magnetic holes are localized depressions in the magnetic field of the solar wind, as the reader can observed in Figure 1.1, which shows observations made by the Ulysses space probe. This mission is very cited in the literature and it is a great example of space mission focused on the study of the solar plasma in the interplanetary space. The phenomena of magnetic holes have been also addressed from the theoretical point of view. In particular, solitary wave solutions to conducting fluid models have been proposed as a theoretical explanation to the observations. *Solitary waves* are localized structures that propagate without deforming inside a medium in equilibrium. *Solitons* are a special type of solitary wave, solution to certain special sets of nonlinear differential equations called *integrable* and have interesting features. One of this characteristics is that two

[1] 1 AU is approximately equivalent to the average distance between the Sun and the Eart, i.e. about 150 million km.

colliding solitons keep their amplitudes, shapes and velocities after the collision; a result that is completely unexpected in nonlinear systems. This thesis studies the existence of solitary waves on certain non-integrable set of equations, so that they cannot be rigorously named solitons.

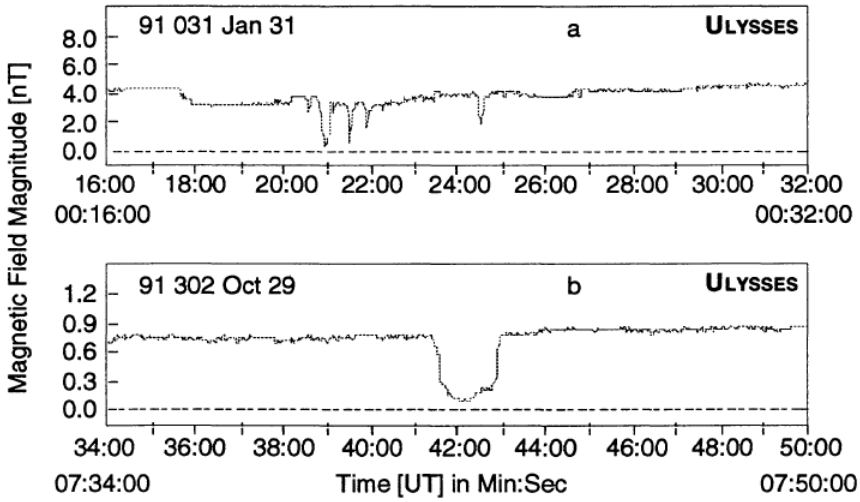

Figure 1.1: Examples of magnetic field intensity evolution when crossing a magnetic hole. Measured by Ulysses magnetometers.
Source: [4]

This project continues the work initiated by Einar Mjølhus in [5] on solitary wave solutions in the Magnetohydrodynamic model with Hall dispersion and Finite Larmor Radius effect —more compactly named FLR Hall MHD model—, using double adiabatic closure for pressure. The same author analyses solitary waves in the Hall MHD system in [1]. In both [5] and [1], the approach is the same: the conducting fluid equations are particularized for traveling wave solutions, yielding a dynamical system, on which the existence of solitary waves is analyzed. The inclusion of FLR effects results into a 5D singular system of ordinary differential equations, which suppose a significant increase in the complexity of the dynamical system if compared to the 2D system in the Hall MHD case. In [5] the FLR Hall MHD dynamical system is derived, it is explained how to deal with the singularity of the system, comments are made on numerical methods to obtain solitary wave solutions and some numerical solutions are shown and discussed. However, the author himself highlights that in no case the results in the article can be considered as a proof of the existence of solitary wave solutions in the FLR Hall MHD model. This thesis addresses the subject of existence of solitary waves in the FLR Hall MHD model and a rigorous demonstration of existence is provided, in certain conditions.

In the previous paragraphs the context of the project has been shortly described, together with a brief comment on the state-of-the-art of solitary waves in the FLR Hall MHD system —which will be discussed in depth in Chapter 2. The rest of the chapter addresses the subjects of solar physics and space observations

of the Sun with a greater level of detail.

1.1 Solar structure and solar wind

This section describes the internal structure of the Sun as well as its atmosphere, with emphasis on solar wind origin and characteristics. In the Sun internal structure several layers can be distinguished —see Figure 1.2— with temperature decreasing from interior to exterior —from 16 million K to 6,000 K— : the *core* in which the nuclear fusion of hydrogen into helium happens, the *radiative zone* and the *convective zone*.

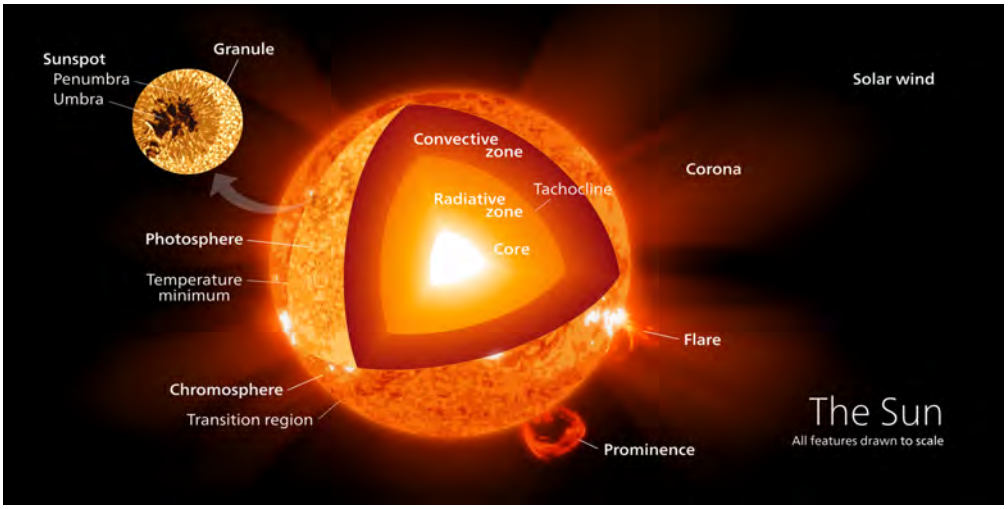

Figure 1.2: Structure of the sun
Source: Wikipedia

On the other hand, the Sun has an atmosphere, in which several regions can be also separated. The *photosphere*, *chromosphere* and *corona* are depicted in Figure 1.2 and remain relatively close to the Sun, but the *heliosphere* —formed by the *termination shock*, the *heliosheath* and the *heliopause*— extends up to more than 130 AU —see Figure 1.4. The photosphere is the visible layer of the Sun. Solar plasma heats up from 4,500 K in photosphere up to 1 million K in the corona. This heating of plasma in the innermost solar atmosphere is still under research, and there are several candidates: Alfven waves, slow and fast magneto-acoustic waves, current dissipation, microflares, etc. Beyond the Sun's corona the plasma extends from the Sun as solar wind, and transports the Sun's magnetic field. The magnetic field lines associated to the Sun's magnetic field tend to form closed curves —i.e. the lines depart from the Sun's surface and return to it—, which prevent plasma from escaping to the interplanetary space. However, there are regions over the solar surface in which magnetic lines are not closed but continue in the interplanetary medium, allowing solar plasma to escape the Sun. This solar plasma is known as solar wind, which can be classified into:

- *Fast solar wind*. The plasma material has velocities of the order of 750 km/s and escapes from large regions of open magnetic field lines —called *coronal*

holes— arising from the Sun. In x-ray images these zones appear as dark areas —see Figure 1.3(a).

- *Slow solar wind*. The velocity is, in this case, about 400 km/s. The main sources of slow solar wind are *helmet streamers*, regions of closed magnetic field lines, mostly. However, some magnetic lines do not form closed loops and solar plasma is able to escape, but in a lesser extent than in coronal holes —see Figure 1.3(b).

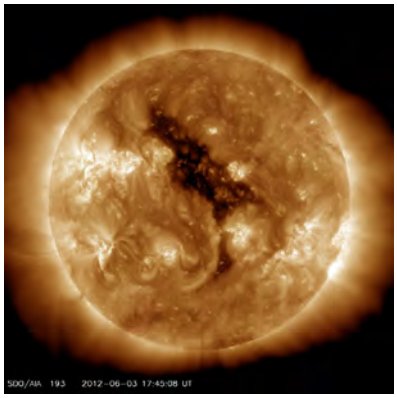

(a) Coronal hole —X-ray image by the NASA's space telescope Solar Dynamics Observatory (SDO). Source: NASA

(b) Helmet streamers during total solar eclipse. Source: NASA

Figure 1.3: Sources of fast (a) and slow (b) solar wind.

Although the simplified explanation of coronal holes and helmet streamers as the main sources of fast and slow solar wind —respectively— is commonly accepted, the real phenomena is more complicated and is still and active subject of research —see reference [6] for a deeper explanation on the sources of solar wind.

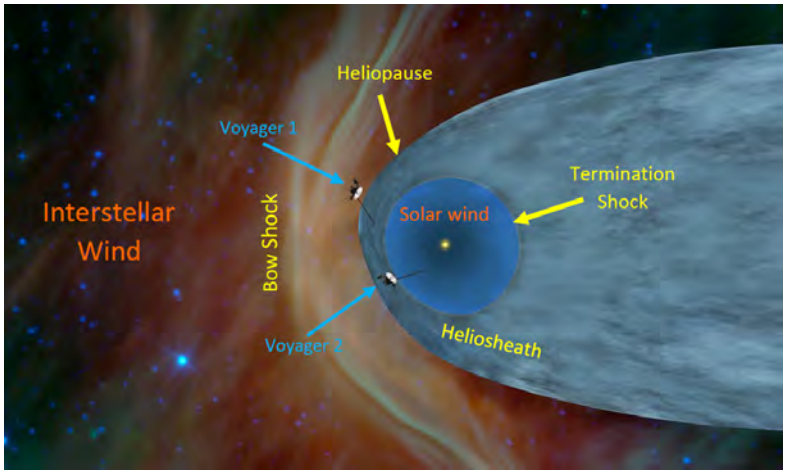

Figure 1.4: The Sun heliosphere and its surroundings
Source: NASA —only background image

The Sun's atmosphere fills the Solar System interplanetary space and at the *termination shock* the solar wind suddenly decelerates due to the influence of the interstellar wind, composed of plasma material and radiation from massive stars, supernovas and other violent space phenomena. The *heliosheath* comprises the space between the termination shock and the *heliopause*, which is the border that separates the solar wind from the interstellar wind. A *bow shock* appears as a result of the movement of the Sun an its atmosphere with respect to the interstellar wind.

Since 25 August 2012, the Voyager 1 is the first spacecraft in exploring the interstellar medium. Nowadays, the Voyager 2 is in the heliosheath and is directed also to cross the heliopause. Both spacecraft completed their corresponding main mission but are still exploring the space and sending interesting scientific data to the Earth in the frame of the Voyager Interstellar Mission (VIM).

1.2 Space missions and magnetic holes

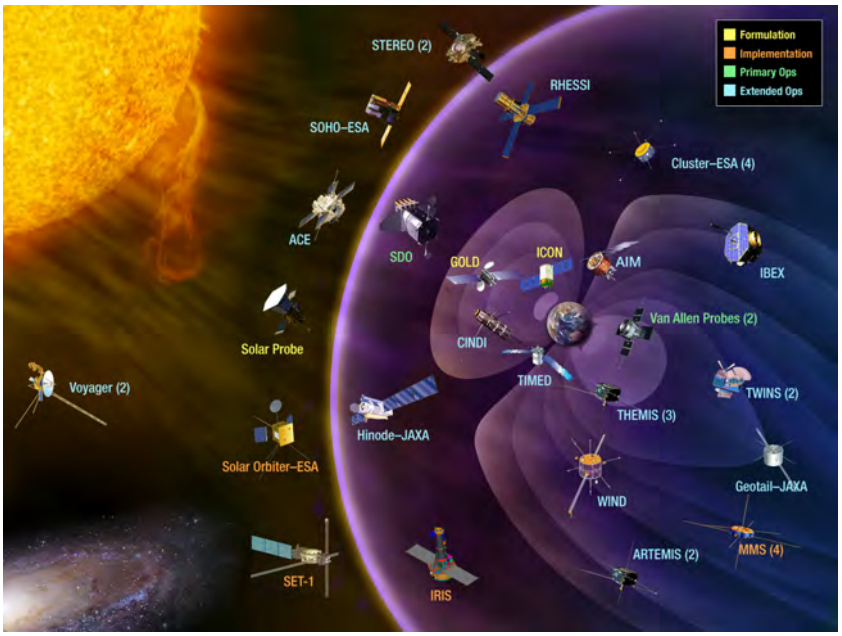

Figure 1.5: Heliophysics System Observatory (HSO).
The fleet of spacecraft involved in NASA heliophysics investigations —some of them in collaboration with other space agencies, such as ESA or JAXA. Not updated.
Source: NASA

The previous section highlights that heliophysics and space plasmas are very interesting fields of investigation, and there is still a lot of work to do. In the process of understanding solar physics, theory must go together with observations made by space probes. A large number of space mission are involved in heliophysics researches. Those working for NASA, currently active and other that are being prepared are shown in Figure 1.5. This picture is not totally updated. For exam-

ple, the space probes IRIS and MMS are already in space.

An interesting location in space regarding solar wind observation is the Lagrangian point 1 (L1), placed in the ecliptic plane and between the Earth and the Sun. Lagrangian points are special locations in a problem of orbital mechanics involving two big-mass bodies —the Sun and the Earth in the concerning case— and one small-mass body. These points are positions in which the small mass could maintain the relative position with respect to the other two bodies —this is constant position in a reference frame centered at the Sun and rotating at the same rate than Earth's rotation around the Sun, for example—, and happen at points in which the combined gravitational force balances the centrifugal force —that must be taken into account because of the rotating reference frame. The point L1 is closer to the Sun than the Earth, so that the orbital period of a small-mass body should be shorter than the Earth's one if only the Sun gravity is considered. However the influence of the Earth alleviates the Sun's gravity, making possible for a spacecraft in L1 to orbit with the same period than Earth. This is interesting since solar wind from the Sun reaches L1 one hour before the Earth, so that any space probe orbiting on L1 can anticipate violent space weather phenomena coming from the Sun. On the other hand, orbits near L1 are unstable under perturbations so that spacecraft in L1 have to correct their orbits from time to time. The space probes SOHO and ACE have orbits close to L1.

1.2.1 The Ulysses mission and magnetic holes

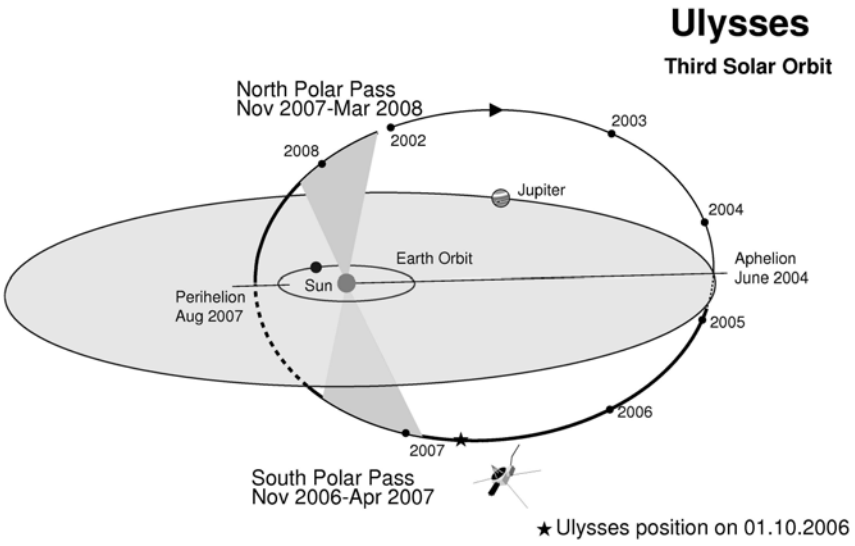

Figure 1.6: Ulysses third solar orbit.
Apohelion: 5.40 AU. Perihelion: 1.35 AU. Inclination: 79.11º. Period: 6.2 years.
Source: ESA

The Ulysses mission, made in collaboration of ESA and NASA , was launched on 6 October 1990 by the Discovery space shuttle and ended on 30 June 2009. The

main target of Ulysses was the study of the Sun on their polar regions. Up to then all measurements on solar activity were made on the plane of the ecliptic —which coincides with the Sun's equator—, so that the scientific interest was on characterizing the Sun behavior out of this plane. To accomplish this task, Ulysses spacecraft was placed on a polar orbit around the Sun by making a gravity assist maneuver on Jupiter. Ulysses completed almost three orbits before the end of the mission.

In the course of the mission, localized magnetic events were measured in the plasma appearing as decreases of the magnetic field amplitude with certain rotation of the magnetic field vector. These events have been identified to be *magnetic holes*. The Ulysses mission is emphasized because its measurements of these events are a great example of magnetic holes observed in the interplanetary space, but magnetic holes or similar behaviors have also been observed by other missions —e.g. Cluster or Helios. It is very common to find references to Ulysses and Cluster missions in the recent literature. In the last case, magnetic holes were observed in the Earth's magnetosheath.

Regarding events detected by Ulysses reference [7] establishes that magnetic holes were measured at the entire range of heliolatitudes and radial distances —no preference for certain latitudes or distances— but only during solar maximum[2] —which occurred during the second orbit. In solar minimum, magnetic holes were only detected in the ecliptic plane —during the ecliptic trajectory phase and the first orbit. Magnetic holes were mostly captured in slow solar wind. However due to many effects affecting the results at the same time is difficult to extract any conclusion in terms of latitude, distance or solar cycle dependency. On the other hand, detected events were close in time. This is, when conditions are adequate for one magnetic hole to take place, it is very likely that it comes together with more events. Moreover all of them were detected with the solar wind in equilibrium —but [7] also mentions this may be due to the difficulty of detecting such events in very active solar wind.

In [8] some of the characteristics of magnetic holes are gathered in the introduction. This type of structures are characterized by sudden decreases in the magnetic field intensity. It is again mentioned that magnetic holes appear as localized structures in quiet plasma —no oscillating behavior— and they may come in groups. Furthermore, the plasma velocity and ambient magnetic field vector change across one magnetic hole is very small. Finally, it is mentioned that the propagation angle of the structure with respect to the ambient magnetic field vector is large. In Figure 1.1 two examples of a detected magnetic hole are shown —the idea of magnetic hole is more ideally represented in subplot (b).

Some characteristic of magnetic holes remind solitary waves, which appear as traveling wave solutions to systems of partial differential equations. Although a more rigorous definition of solitary wave will be later given in Chapter 3, they are localized structures that propagates at constant speed without deforming inside

[2]The Sun's activity seems to be cyclic with a period of 11 years.

a medium that is in equilibrium —e.g. quiet solar wind. It is evident that the features of the observed magnetic holes fit very well with the definition of solitary wave. This is the reason why magnetic holes have been tried to be theoretically explained in terms of solitary wave solutions to plasma fluid models. There is an extensive list of papers dealing with this subject.

1.3 Motivation, goals and outline

The Sun is the most important celestial body for humans. It is because of Sun that life is possible, it is a source of energy and is the driver of many important phenomena on Earth. The Sun is also the main player of many events taking place in the solar system. It protects us against the interstellar medium and its magnetic field and solar material covers the nearby outer space, so that particles and radiation from the Sun are continuously hitting the Earth and spacecraft. It is in this last subject that this thesis is focused.

Strong solar wind and solar storms may have a negative influence on Earth power lines and telecommunication, specially during solar maximums. Large amounts of solar material directed to the Earth can deform the Earth's magnetic field and disrupt signals, affecting, for example, air navigation. Moreover, solar wind also blows against spacecraft on space and may damage electronic components and instruments that cannot be easily replaced or repaired.

It is clear that understanding solar wind, and heliophysics in general, is important. Regarding the development of protection and mitigation techniques against dangerous phenomena from the Sun, having all possible information and understanding the physics behind is fundamental. The project presented in this thesis is made on the context of theoretical approaches to magnetic holes measured in solar wind, so that it is a contribution to the process of comprehending the Sun and its related phenomena.

The main objective of this project is to solve the problem of existence of solitary wave solutions in an specific plasma fluid model, the Magnetohydrodynamic model with Hall and Finite Larmor Radius effects —which seems to be adequate for solar wind modeling. Furthermore, an introduction will be given to the suitable experimental instruments needed to measure a real magnetic hole and certain considerations on a hypothetical space mission will be addressed.

With these purposes in mind, Chapter 2 deals with an introduction to theoretical plasma models and in Chapter 3 the required mathematical knowledge is compiled. Chapter 4 is about how theory applies to the concerning problem, the most important details about the algorithms, as well as the results. Chapter 5 deals with the mentioned hypothetical mission. Topics concerning the regulatory frame and socio-economic environment will be included also in this chapter. The final chapter will be devoted to extracting conclusions and proposing possible future investigations.

Chapter 2

Plasma Models

The work presented in this document is based on models that consider the plasma as a conducting fluid. These models can be seen as extensions of Navier-Stokes equations for neutral fluids —continuity, conservation of momentum and conservation of energy—, including electromagnetic variables and forces, since the fluid is not neutral but formed of charged particles. As it will be remarked later, the time evolution of the electromagnetic fields is described by Maxwell equations, and it is influenced by the fluid motion. In turn, electromagnetic fields have an effect on the motion of the fluid. Therefore, the evolution of the plasma macroscopic properties and the evolution of the magnetic and electric fields are coupled, so that continuity, momentum and energy equations must be solved together with Maxwell's equations.

However, some simplifications can be introduced that reduce the degree of complexity of solving the entire set of equations keeping all terms. Depending on the assumptions supporting these simplifications, there exists several plasma conducting fluid models. The results presented in further sections are based on the Hall Magnetohydrodynamic model with Finite Larmor radius effect —FLR-Hall-MHD model. Along this chapter, several magnetohydrodynamical models will be presented, from the simplest MHD to FLR-Hall-MHD, going through the Hall-MHD.

Definition of plasma macroscopic variables

In magnetohydrodynamics, the plasma state is described by its macroscopic properties, and all species are treated as a whole, rather than individually. Although, macroscopically, each specie may have different density or velocity —this information is lost with this approach—, the plasma macroscopic variables are defined in the following way[1], and account for the contributions of the individual species:

[1]Many theoretical concepts and derivations are based or have been taken from [9] and [10], which use different notation. In order to avoid confusions, the notation used in this part of the thesis does not necessarily follow none of them.

- Mass density

$$\rho = \sum_{\alpha} \rho_{\alpha} = \sum_{\alpha} n_{\alpha} m_{\alpha} \tag{2.1}$$

- Electric charge density:

$$\rho_c = \sum_{\alpha} n_{\alpha} q_{\alpha} \tag{2.2}$$

- Mean velocity, defined in such a way that the linear momentum per unit volume computed with the mass density and the mean velocity is the sum of momentums —per unit volume— of all the species, i.e.

$$\mathbf{v} = \frac{1}{\rho} \sum_{\alpha} \rho_{\alpha} \mathbf{v}_{\alpha} \tag{2.3}$$

- Diffusion velocity, defined for each specie as the relative velocity with respect to a reference frame moving with the mean velocity $\mathbf{v}$, i.e.

$$\mathbf{w}_{\alpha} = \mathbf{v}_{\alpha} - \mathbf{v} \tag{2.4}$$

- Electric current density

$$\mathbf{J} = \sum_{\alpha} n_{\alpha} q_{\alpha} \mathbf{v}_{\alpha} = \rho_c \mathbf{v} + \sum_{\alpha} n_{\alpha} q_{\alpha} \mathbf{w}_{\alpha} \tag{2.5}$$

  It is interesting the fact that, even if the plasma is macroscopically neutral —i.e. $\rho_c = 0$—, there may still exist an electric current density at scales greater than the Debye length[2] due to the diffusion velocity.

In this definitions the subindex α accounts for one particle specie, n is the number density —i.e. the number of particles per unit volume— and m is mass.

Maxwell Equations

Maxwell's equations in differential form can be derived from their integral form —more intuitive and meaningful— evaluated on a differential volume and using Gauss' and Stokes' theorems. The Maxwell's equations expressed in Gaussian units are:

- Faraday's Law establishes that whenever the magnetic field changes with time, an electric field appears whose lines are arranged in closed loops. This equations gives the time evolution of the magnetic field.

$$\nabla \times \mathbf{E} = -\frac{1}{c} \frac{\partial \mathbf{B}}{\partial t} \tag{2.6}$$

[2]The Debye length is the scale above which there is macroscopic neutrality in plasmas.

- Ampere's Law describes how a magnetic field appears —with its lines in closed loops— whenever there exists an electric current density or a time-varying electric field. Ampere's law is an expression for the time evolution of the electric field.

$$\nabla \times \mathbf{B} = \frac{1}{c}\left(4\pi\mathbf{J} + \frac{\partial \mathbf{E}}{\partial t}\right) \tag{2.7}$$

- Gauss' Law relates the electric flux on a closed surface with the electric charge inside it, i.e. positive charges are sources and negative charges are sinks of electric field.

$$\nabla \cdot \mathbf{E} = 4\pi\rho_c \tag{2.8}$$

- Gauss' Law for magnetic field states that the magnetic flux through any closed surface is always zero. That is to say, there are no magnetic sources or sinks, magnetic monopoles do not exist. This means that magnetic field lines either are closed or go to infinity.

$$\nabla \cdot \mathbf{B} = 0 \tag{2.9}$$

From Kinetic Theory to Macroscopic equations

Both conducting and non-conducting fluids are nothing but a large number of particles acting together. Thus, one possibility to describe the state of any fluid is to solve the equations of motion for every single particle, for given initial conditions. This is typically not computationally affordable due to the huge number of particles and data to be managed. The next step is to go to a statistical approach, the *kinetic theory*.

In kinetic theory the single-particle phase space is defined by $(\mathbf{r}, \mathbf{v})$, being $\mathbf{r}$ the position vector and $\mathbf{v}$ the velocity vector. Each particle is connected with one point in the 6D phase space, given by its position and velocity. If one takes a differential 6D cube located at $(\mathbf{r}, \mathbf{v})$ in this state space, there will be a number of points lying inside this cube, meaning that their position and velocity take values between $(\mathbf{r}, \mathbf{v})$ and $(\mathbf{r} + d\mathbf{r}, \mathbf{v} + d\mathbf{v})$. The distribution function $f_\alpha(\mathbf{r}, \mathbf{v}, t)$ gives the phase-space density of α-specie particles in an infinitesimal cube at $(\mathbf{r}, \mathbf{v})$ and at time instant t. The distribution function can be computed by solving the *Boltzmann equation*

$$\frac{\partial f_\alpha}{\partial t} + \mathbf{v} \cdot \nabla f_\alpha + \mathbf{a} \cdot \nabla_v f_\alpha = \left(\frac{\delta f_\alpha}{\delta t}\right)_{\text{coll}} \tag{2.10}$$

whose derivation can be found in Chapter 5 Section 5 of [9]. In Equation (2.10) $\mathbf{a}$ stands for the acceleration vector, ∇_v for the differential operator with respect to velocity components and $(\delta f_\alpha/\delta t)_{\text{coll}}$ for the contribution from particle collisions. This last term is zero in the case of collisionless plasmas, e.g. in the case of solar

wind.

The distribution function condensates all the physical information of the system. Once it is known, all macroscopic properties can be computed from the moments of $f_\alpha(\mathbf{r},\mathbf{v},t)$. The macroscopic or average value of an arbitrary property $\phi(\mathbf{r},\mathbf{v},t)$ at position $\mathbf{r}$ and time t for a particular specie α, is obtained by multiplying[3] $f_\alpha(\mathbf{r},\mathbf{v},t)\ d^3r\, d^3v$ and $\phi(\mathbf{r},\mathbf{v},t)$ —i.e. the total amount of ϕ inside the differential 6D cube located at $(\mathbf{r},\mathbf{v})$ in the state space—, integrating over all velocity components from $-\infty$ to $+\infty$ —since we are interested in all α-specie particles infinitesimally close to $\mathbf{r}$ position, disregarding their velocity— and dividing by the the total number of particles of that specie close to position $\mathbf{r}$, independently of their velocity —this is the integral of $f_\alpha(\mathbf{r},\mathbf{v},t)\, d^3r\, d^3v$ over the complete velocity domain—, i.e.

$$< \phi >_\alpha (\mathbf{r},t) = \frac{d^3r \int_v \phi(\mathbf{r},\mathbf{v},t)\, f_\alpha(\mathbf{r},\mathbf{v},t)\, d^3v}{d^3r \int_v f_\alpha(\mathbf{r},\mathbf{v},t)\, d^3v} = \frac{1}{n_\alpha(\mathbf{r},t)} \int_v \phi(\mathbf{r},\mathbf{v},t)\, f_\alpha(\mathbf{r},\mathbf{v},t)\, d^3v$$

Solving the Boltzmann equation in order to compute the distribution function of a particle specie can be a complex task. However, differential equations can be obtained that lead the temporal and spatial behavior of the macroscopic properties of a particular specie from the Boltzmann equation, without actually solving it; i.e. the *macroscopic transport equations*. This is achieved in a very similar way than previously done for the computation of one macroscopic variable. In this case, the entire Boltzmann equation has to be multiplied by the property of interest and integrate all over the velocity space. The first three moments of the Boltzmann equation are computed multiplying by m_α, $m_\alpha \mathbf{v}_\alpha$ and $m_\alpha v_\alpha^2/2$, which result into the continuity equation, the momentum transport equation and the energy transport equation respectively.

Each new moment of the Boltzmann equation introduces a new unknown[4], that requires of a higher order moment. The differential equation giving the distribution function is equivalent to an infinite system of Partial Differential Equations (PDEs). This fact may give an idea of the large amount of information contained in the distribution function. In order to avoid having such a large system of PDEs, a few moments of the Boltzmann equation are typically derived and a reasonable simplifying assumption is introduced in the higher moment equation that allows to close the system.

The transport equations govern the behavior of macroscopic variables for each individual specie in the plasma, but MHD theory considers the plasma as a whole.

[3] d^3r is the differential volume element in the position space, while d^3v is the differential volume element in the velocity space

[4] For example, the continuity equation gives the space and temporal evolution of density but involves the linear momentum. In turn momentum is given by the solution of the momentum equation, but it requires of knowing the pressure. The pressure can be obtained from the solution of the energy equation, but the heat flux appears as a new unknown.

By adding up all species' continuity equations and using the definitions of the plasma macroscopic variables, the general continuity equation

$$\frac{\partial \rho}{\partial t} + \nabla \cdot (\rho \mathbf{v}) = 0 \tag{2.11}$$

is obtained. Note that the collision terms, present in the individual transport equations, cancel when considering the species all together:

In a similar way the momentum equation for a conducting fluid can be derived, which reads

$$\frac{\partial}{\partial t}(\rho \mathbf{v}) + \nabla \cdot (\rho \mathbf{v}\mathbf{v}) = \rho_c \mathbf{E} + \frac{\mathbf{J} \times \mathbf{B}}{c} - \nabla \cdot \underset{\sim}{\mathbf{P}} \tag{2.12}$$

where $\underset{\sim}{\mathbf{P}}$ stands for the pressure tensor —in the most general case, anisotropic pressure has to be considered. Gravity has been neglected against electromagnetic forces. Therefore, the only important volumetric force acting on the fluid is the Lorentz force $\rho_c \mathbf{E} + \mathbf{J} \times \mathbf{B}/c$.

Typically the system of transport equations is truncated at the third moment —included—, which yields the overall energy equation[5]

$$\frac{1}{\gamma - 1}\frac{Dp}{Dt} + \frac{p}{\gamma - 1}\nabla \cdot \mathbf{v} + \nabla \cdot \mathbf{q} + \left(\underset{\sim}{\mathbf{P}} \cdot \nabla\right) \cdot \mathbf{v} = \mathbf{J}' \cdot \mathbf{E}' \tag{2.13}$$

in which $\mathbf{E}' = \mathbf{E} + (\mathbf{v} \times \mathbf{B})/c$, $\mathbf{J}' = \mathbf{J} - \rho_c \mathbf{v}$, $\mathbf{q}$ stands for the heat flux vector and the scalar p is defined as one third of the trace of $\underset{\sim}{\mathbf{P}}$. The right-hand-side of Equation (2.13) is Joule heating effect.

Generalized Ohm's Law

From the macroscopic transport equations of momentum for each specie one more equation can be derived, the generalized Ohm's Law. It is called *generalized* because typically some terms can be neglected, so that it is common to use a reduced version of this equation. In Chapter 9 Section 5.3 of [9] the generalized Ohm's Law is derived and particularized for the case of two particle species in the plasma: electrons and one kind of ions —which is the case also in [5] and in this thesis. Therefore, in the considered plasma there exist two species of equal charge (e) —with opposite sign— and this assumption, together with macroscopic neutrality ($\rho_c = 0$) implies that —from Equation (2.2)— the number density of electrons (n_e) must coincide with the number density of ions (n_i), i.e $n_i = n_e = n$. Furthermore, it must be taken into account that the mass of ions (m_i) is much larger than the mass of electrons (m_e), i.e. $m_e \ll m_i$, which results into $n \simeq \rho/m_i$

[5]The process of deriving the macroscopic equation is based, mainly on Chapter 9 of J.A. Bittencourt's book [9]. However, the energy equation is posed in this thesis modified, in order to be more general. In [9] the energy equation is particularized for monoatomic gases, whose particles has 3 degrees of freedom and, thus, the adiabatic gas constant $\gamma = 5/3$

from the definition of mass density (2.1).

In order to reach the expression for the Generalized Ohm's Law, the momentum transport equation corresponding to each particle must be multiplied by q_α/m_α and all momentum transport equations added together. An intermediate step is to use the continuity equation. The result is

$$\frac{m_e}{ne^2}\left[\frac{\partial \mathbf{J}}{\partial t} + \nabla\cdot(\mathbf{J}\mathbf{v} + \mathbf{v}\mathbf{J})\right] - \frac{1}{ne}\nabla\cdot\underset{\sim}{\mathbf{P}}_e = \mathbf{E} + \frac{\mathbf{v}\times\mathbf{B}}{c} - \frac{1}{ne}\frac{\mathbf{J}\times\mathbf{B}}{c} - \eta\mathbf{J} \quad (2.14)$$

Ohm's law can be thought as an equation governing the time evolution of the electric current density. The first term in the left-hand side of Equation (2.14) is called the *electron inertia* term and the second one is the contribution of the electron pressure. On the right-hand side of the equation, there are contributions from the Lorentz force and the electric current density itself. The third term —i.e. $1/ne\,\mathbf{J}\times\mathbf{B}/c$— is called the *Hall* term and it will be important in the Hall-MHD model.

2.1 MHD

The introductory part of this chapter has introduced the equations needed to construct the magnetohydrodynamical models, giving also some background on their origin and meaning. The MHD models are simplified versions of this set of equations, based on certain hypotheses. Let us summarize the most important ones in the case of the pure MHD model:

1. Quasi-neutrality ($\rho_c \approx 0$). This assumption is already in the generalized Ohm's Law —Equation (2.14)— and implies that, as long as one single type of ions is considered, the number density of ions is equal to the number density of electrons ($n_i = n_e = n$). This is true at scales grated than the Debye length. Another important consequence is that the electric force effects on the flow can be neglected —i.e. the term $\rho_c\mathbf{E}$ in the momentum equation (2.12). Furthermore $\mathbf{J}' \approx \mathbf{J}$ in the energy equation.

2. The electron mass is much smaller than the ion mass ($m_e \ll m_i$). That is to say, the equations are particularized for the limit $m_e \to 0$. Under this limit the plasma frequency and the electron girofrequency tend to infinity, so that they cannot be taken into account any more. The simplification $m_e \to 0$ implies that these small scale high frequency phenomena cannot be captured by this model.

3. The Ohm's Law is simplified by neglecting the electron inertia and Hall terms, as well as the contribution from the electron pressure. This assumption is based on an order-of-magnitude analysis. In addition, if the magnetic Reynolds number —$R_M = 4\pi V_c L/(\eta c^2)$, being V_c and L the characteristic speed and the characteristic length, respectively— is much

larger than one —i.e. the plasma is highly conductive— the resistivity term can be also dropped from the Ohm's Law. This can be proved by comparing the order of magnitude of $\eta\mathbf{J}$ —which is $\eta Bc/\left(4\pi L\right)$, from Ampere's Law— and $\mathbf{v}\times\mathbf{B}/c$ —$V_c B/c$. If one neglects resistivity effects ideal MHD equations are reached, but one could retain the corresponding term, in which case resistive MHD equations are obtained. Let us restrict to the case of ideal MHD, due to the high solar wind conductivity. Under these assumptions, the Ohm's Law is reduced to

$$\mathbf{E}+\frac{\mathbf{v}\times\mathbf{B}}{c}=0 \tag{2.15}$$

which implies $\mathbf{E}'=0$ and, thus, there are no heating term due to Joule effect in the energy equation.

4. The pressure is isotropic, i.e. pressure is equal independently of the direction and there are no shear terms. This is mathematically translated into a diagonal pressure tensor, whose diagonal terms are all equal. Therefore $\nabla\cdot\underset{\sim}{\mathbf{P}}=\nabla p$, being p the scalar pressure value. This is the case when viscosity is not included and the plasma is considered to be sufficiently collisional. Solar wind is not a very collisional plasma, so that a good solar wind model should modify this assumption.

5. The displacement current can be neglected in Ampere's law —Equation (2.7). By using Equations (2.15) and (2.7), it can be seen that the force due to the magnetic field in the momentum equation is

$$\frac{\mathbf{J}\times\mathbf{B}}{c}=\frac{1}{4\pi}\left[\nabla\times\mathbf{B}-\frac{1}{c}\frac{\partial\mathbf{E}}{\partial t}\right]\times\mathbf{B}=\frac{1}{4\pi}\left[\nabla\times\mathbf{B}+\frac{1}{c^2}\frac{\partial}{\partial t}\left(\mathbf{u}\times\mathbf{B}\right)\right]\times\mathbf{B}$$

An order-of-magnitude analysis suggest that the displacement current effects on the momentum equation can be ignored as long as the ratio of the magnetic energy density to one half the mass energy density is much smaller than 1 —this is achieved by comparison with the order of magnitude of $\rho\,\partial\mathbf{v}/\partial t$—, i.e.

$$\frac{B^2/\left(8\pi\right)}{1/2\ \rho c^2}\ll 1$$

6. Heat flux is neglected, i.e. $\nabla\cdot\mathbf{q}\approx 0$.

7. Finite Larmor Radius (FLR) effects are negligible. That is to say, important variations of the macroscopic properties occur spatially at scales greater than the ion gyroradius —also called Larmor radius— and temporally at scales greater than the ion cyclotron period.

Note that the effect of the magnetic field in Equation (2.12) —once the displacement current has been dropped— can be understood as an extra non-isotropic pressure —called *magnetic pressure*— acting on the fluid, as it can be expressed as the divergence of a magnetic pressure tensor in the following way

$$\frac{1}{4\pi}\left(\nabla\cdot\mathbf{B}\right)\times\mathbf{B}=\frac{1}{4\pi}\left[\left(\mathbf{B}\cdot\nabla\right)\mathbf{B}-\frac{1}{2}\nabla\left(B^2\right)\right]=\frac{1}{4\pi}\nabla\cdot\left(\mathbf{BB}-\frac{1}{2}B^2\underset{\sim}{\mathbf{I}}\right)$$

where $\underset{\sim}{\mathbf{I}}$ is the identity tensor.

The resultant set of equations

$$\frac{\partial\rho}{\partial t}+\nabla\cdot\left(\rho\mathbf{v}\right)=0 \tag{2.16}$$

$$\frac{\partial}{\partial t}\left(\rho\mathbf{v}\right)+\nabla\cdot\left[\rho\mathbf{vv}+p\,\underset{\sim}{\mathbf{I}}+\frac{1}{4\pi}\left(\frac{1}{2}B^2\underset{\sim}{\mathbf{I}}-\mathbf{BB}\right)\right]=0 \tag{2.17}$$

$$\frac{\partial\mathbf{B}}{\partial t}=\nabla\times\left(\mathbf{v}\times\mathbf{B}\right) \tag{2.18}$$

$$\frac{p}{\rho^\gamma}=\text{const.} \tag{2.19}$$

is the MHD model. The simplifications made have allowed to eliminate $\mathbf{E}$, $\mathbf{J}$ and ρ_c from the equations. Therefore, the only remaining electromagnetic variables are the components of $\mathbf{B}$. That is to say, three equations are needed additionally to the fluid equations, coming from the Faraday's induction equation —Equation (2.6)— with $\mathbf{E}$ given by Equation (2.15). The energy equation has been reduced to Equation (2.19), which is the adiabatic relation for isentropic flow evolution. The quantity p/ρ^γ is conserved along streamlines.

An interesting property of the the pure MHD model is *flux freezing*, which consist on the conservation of magnetic flux through any surface moving with the fluid. This result also applies for zero-flux surfaces and, thus, magnetic lines are forced to move together with the fluid. Moreover, there are neither reconnection or breaking of magnetic lines. This is the mechanism by which the Earth's magnetosphere shields the planet against the solar wind or the closed magnetic field lines on the solar surface prevent the plasma from escaping out of the corona.

2.2 Hall-MHD

Rigorously speaking, the Hall MHD model should differ from MHD only in the inclusion of the Hall term in the Ohm's Law. This additional term will be translated into a modified magnetic induction equation, compared to Equation (2.18). However, the goal is to find a good model for solar wind plasma that allow us to get theoretical results and conclusions related to magnetic holes. Bearing this purpose in mind, let us introduce additional changes.

The pressure is decomposed as the contribution from the electrons and the one from the ions, i.e. $\underset{\sim}{\mathbf{P}}=\underset{\sim}{\mathbf{P}}_e+\underset{\sim}{\mathbf{P}}_i$. While the isotropic pressure assumption is

maintained for electrons[6], it will be rejected for the case of ions and substituted by a different pressure model —the *double adiabatic equations* of Chew, Goldberg and Low (CGL).

Hall effect

The Hall effect plays an important role at scales smaller than the ion inertial length c/ω_{pi} —being ω_{pi} the *ion plasma frequency*, i.e. the characteristic frequency of oscillations of the ions in the plasma.

The number density can be expressed as function of density by means of $n = \rho/m_i$ —as a result of $m_e \ll m_i$ and $\rho_c = 0$. The resultant form of the Ohm's law reads

$$\mathbf{E} + \frac{\mathbf{v} \times \mathbf{B}}{c} - \frac{m_i}{4\pi e\rho} (\nabla \times \mathbf{B}) \times \mathbf{B} = .0 \tag{2.20}$$

in which Equation (2.7) without displacement current was used to substitute $\mathbf{J}$. Equation (2.20) can be used to eliminate $\mathbf{E}$ from Equation (2.6), yielding and expression for the evolution of the magnetic field

$$\frac{\partial \mathbf{B}}{\partial t} = \nabla \times \left[\mathbf{v} \times \mathbf{B} - \frac{m_i c}{4\pi e\rho} (\nabla \times \mathbf{B}) \times \mathbf{B} \right] \tag{2.21}$$

An important difference between Equations (2.18) and (2.21) is that, in the last case, there are second spatial derivatives of the magnetic field. This a crucial feature, that allows the existence of stationary solitary wave solutions in this system, as the kind of solutions this thesis aims to find.

Pressure model

As already mentioned, the pressure is expressed as the sum of the contributions of ions and electrons, i.e

$$\underset{\sim}{\mathbf{P}} = \underset{\sim}{\mathbf{P}}_e + \underset{\sim}{\mathbf{P}}_i \tag{2.22}$$

Moreover, isotropic electron pressure is assumed, i.e.

$$\underset{\sim}{\mathbf{P}}_e = p_e \, \underset{\sim}{\mathbf{I}} \tag{2.23}$$

in which p_e is the scalar electron pressure and it is assumed an isothermal equation of state[7], i.e. $p_e = \rho v_{se}^2$. The parameter v_{se} is the electron contribution to the ion

[6]Notice that the electron gyroradius and gyrofrequency are, respectively, much smaller and much larger than the ion's ones. Therefore, the motion of the electron perpendicularly to the local magnetic field may be neglected, so that anisotropy of pressure is only considered for ions.

[7]The gyradiuos of one particle is proportional to its mass, which means that the electron's one is extremely small. Thus, electrons tend to follow magnetic lines and the heat flow transverse to magnetic lines is negligible. This is the reasoning supporting the isothermal electron assumption.

acoustic velocity, and is given by $v_{se}^2 = \kappa T_e/m_e$, being κ the Boltzmann's constant and T_e the electron temperature.

On the other hand, the ion pressure has been said to be anisotropic. If the plasma is approximated to be collisionless —as it is the case of solar wind—, the assumption of isotropic pressure is not justified. In a nearly collisionless plasma, within the time lapse between collisions the ion rotates several times about magnetic lines, so that pressure is not equal in the directions contained in a plane perpendicular to the local magnetic field and in the longitudinal direction. Therefore, it makes sense to defined a perpendicular scalar pressure ($p_\perp$) —associated to directions perpendicular to $\mathbf{B}$— and a parallel pressure ($p_\parallel$) —associated to the direction of $\mathbf{B}$. According to this reasoning, the pressure tensor in a reference frame with the z axis aligned with the local magnetic field $\mathbf{B}$ reads

$$\underset{\sim}{\mathbf{P}}_i = \begin{bmatrix} p_\perp & 0 & 0 \\ 0 & p_\perp & 0 \\ 0 & 0 & p_\parallel \end{bmatrix} = \begin{bmatrix} p_\perp & 0 & 0 \\ 0 & p_\perp & 0 \\ 0 & 0 & p_\perp \end{bmatrix} + \begin{bmatrix} 0 & 0 & 0 \\ 0 & 0 & 0 \\ 0 & 0 & p_\parallel - p_\perp \end{bmatrix} \tag{2.24}$$

which can be understood as an isotropic pressure $p_\perp$ plus a tension $p_\parallel - p_\perp$ in the $\mathbf{B}$ direction. Equation (2.24) can be expressed in matrix notation rather than by components as

$$\underset{\sim}{\mathbf{P}}_i = p_\perp \underset{\sim}{\mathbf{I}} + \left(p_\parallel - p_\perp\right) \mathbf{e}_b \mathbf{e}_b \tag{2.25}$$

Closing the set of equations needs a model for these pressures. There exist several possibilities: models based on experiments and observations, equations of state based on certain assumptions or differential equations for pressure from the energy equation. Because of the symmetry property of the Hall and FLR Hall MHD systems, explained in further chapters, it is very convenient to have algebraic expressions for pressure. Otherwise the complexity of localizing solitary wave solutions notably increases. Following the approach of [5], double adiabatic equations of state will be assumed. This model was initially proposed by Chew, Golderberg and Low [11] from expansion of the distribution function and taking moments of the collisionless Boltzmann equation, but Bittecourt [9] provides in Chapter 12 Section 1.2 a simple derivation of these equations —particularized for monoatomic gases, i.e. $\gamma = 5/3$. The quantities

$$\frac{p_\parallel B^2}{\rho^3} = \text{const.} \tag{2.26}$$

$$\frac{p_\perp}{\rho B} = \text{const.} \tag{2.27}$$

are conserved along streamlines.

It is important to remark that one assumption behind Equations (2.26) and (2.27) is Ohm's Law of the form $\mathbf{E} + \mathbf{v} \times \mathbf{B}/c = 0$, which may seem inconsistent since the Hall term is not included. However this assumption is required in order

to find simple equations of state, as Equations (2.26) and (2.27) are.

Hall MHD equations

Here, all the previous equations are gathered together. The complete Hall MHD model reads

$$\frac{\partial \rho}{\partial t} + \nabla \cdot (\rho \mathbf{v}) = 0 \tag{2.28}$$

$$\frac{\partial}{\partial t}(\rho \mathbf{v}) + \nabla \cdot \left[\rho \mathbf{v}\mathbf{v} + \underset{\sim}{\mathbf{P}}_i + p_e \underset{\sim}{\mathbf{I}} + \frac{1}{4\pi}\left(\frac{1}{2}B^2 \underset{\sim}{\mathbf{I}} - \mathbf{B}\mathbf{B}\right)\right] = 0 \tag{2.29}$$

$$\frac{\partial \mathbf{B}}{\partial t} = \nabla \times \left[\mathbf{v} \times \mathbf{B} - \frac{m_i c}{4\pi e \rho}(\nabla \times \mathbf{B}) \times \mathbf{B}\right] \tag{2.30}$$

with $p_e = \rho v_{se}^2$, $\underset{\sim}{\mathbf{P}}_i = p_\parallel \mathbf{e}_b \mathbf{e}_b + p_\perp \left(\underset{\sim}{\mathbf{I}} - \mathbf{e}_b \mathbf{e}_b\right)$ and $p_\parallel$ and $p_\perp$ fulfilling Equations (2.26) and (2.27), respectively.

2.3 Hall-MHD with Finite Larmor Radius effect

The plasma fluid model proposed in the previous section is improved now by including Finite Larmor Radius[8] (FLR) effects. To be precise, ion FLR, which is much larger than the electron's one. In

$$\Omega_c = \frac{eB}{mc} \tag{2.31}$$

$$r_L = \frac{v_\perp}{\Omega_c} \tag{2.32}$$

it can be noticed that due to the difference in mass between ions and electrons, the gyrofrequency (Ω_c) of electrons is much larger and, as a consequence, its Larmor radius (r_L) is much smaller. In Equations (2.31) and (2.32), $v_\perp$ stands for the velocity of the particle in the plane perpendicular to the magnetic field.

FLR Hall MHD equations introduce additional pressure corrections to CGL equations. The CGL pressure model is only valid for the case of very small gyroradius. By including FLR terms in the pressure, higher frequency and smaller scale phenomena are captured by the model.

[8]The Larmor radius —also called gyroradius or cyclotron radius— is the radius of the circular motion of a charged particle in the presence of an uniform steady magnetic field, in the plane perpendicular to it. The cyclotron frequency or gyrofrequency is the angular frequency of this motion. Both can be mathematically computed in a very simple way, by solving the equations of motion of the particle under the described conditions, with an initial velocity with component in the plane perpendicular to the ambient magnetic field.

The derivation of the ion FLR pressure tensor correction is complex. A complete derivation is provided by Yajima —Appendix of [12]— and MacMhahon [13]. Just to summarize, the FLR pressure tensor comes from the moments of the Vlasov equation[9] and expanding the ion distribution function in terms of $1/\Omega_{ci}$ powers, being Ω_{ci} the ion cyclotron frequency. Zeroth order terms give the CGL pressure tensor $\underset{\sim}{\mathbf{P}}_i^{(0)} = p_\perp \underset{\sim}{\mathbf{I}} + \left(p_\parallel - p_\perp\right) \mathbf{e}_b\mathbf{e}_b$, while first order terms result into the FLR pressure tensor correction $\underset{\sim}{\mathbf{P}}_i^{(1)}$.

The total ion pressure tensor involves the CGL tensor ($\underset{\sim}{\mathbf{P}}_i^{(0)}$) and the FLR correction ($\underset{\sim}{\mathbf{P}}_i^{(1)}$), i.e.

$$\underset{\sim}{\mathbf{P}}_i = \underset{\sim}{\mathbf{P}}_i^{(0)} + \underset{\sim}{\mathbf{P}}_i^{(1)} \tag{2.33}$$

where the CGL contribution is given by

$$\underset{\sim}{\mathbf{P}}_i^{(0)} = \underset{\sim}{\mathbf{P}}_{i,\parallel}^{(0)} + \underset{\sim}{\mathbf{P}}_{i,\perp}^{(0)} \tag{2.34}$$

with $\underset{\sim}{\mathbf{P}}_{i,\parallel}^{(0)} = p_\parallel \mathbf{e}_b\mathbf{e}_b$ and $\underset{\sim}{\mathbf{P}}_{i,\perp}^{(0)} = p_\perp \left(\underset{\sim}{\mathbf{I}} - \mathbf{e}_b\mathbf{e}_b\right)$. The double adiabatic model for pressure does not take into account Finite Larmor Radius effects on energy —apart from neglecting the Hall term. The FLR correction is divided in three different contributions, i.e.

$$\underset{\sim}{\mathbf{P}}_i^{(1)} = \underset{\sim}{\mathbf{P}}_{i,1}^{(1)} + \underset{\sim}{\mathbf{P}}_{i,2}^{(1)} + \underset{\sim}{\mathbf{P}}_{i,3}^{(1)} \tag{2.35}$$

with

$$\underset{\sim}{\mathbf{P}}_{i,1}^{(1)} = \frac{1}{\Omega_{ci}} \left[\frac{1}{4}\mathbf{e}_b \times \left(\nabla\mathbf{v} + \nabla\mathbf{v}^T\right) \cdot \underset{\sim}{\mathbf{P}}_{i,\perp}^{(0)} + \text{transp.}\right] \tag{2.36}$$

$$\underset{\sim}{\mathbf{P}}_{i,2}^{(1)} = -\frac{1}{\Omega_{ci}} \left[\mathbf{e}_b \left(\nabla \times \mathbf{v}\right) \cdot \underset{\sim}{\mathbf{P}}_{\perp}^{(0)} + \text{transp.}\right] \tag{2.37}$$

$$\underset{\sim}{\mathbf{P}}_{i,3}^{(1)} = \frac{2}{\Omega_{ci}} \left[\mathbf{e}_b \left(\underset{\sim}{\mathbf{P}}_{i,\parallel}^{(0)} \cdot \nabla\right) \times \mathbf{v} + \text{transp.}\right] \tag{2.38}$$

where $\Omega_{ci} = eB/\left(m_i c\right)$ and *transp.* stands for the transpose of the other term inside the brackets. It is very important the fact that Ω_{ci} in Equations (2.36)-(2.38) has to be evaluated with the local magnetic field amplitude B.

In the FLR Hall MHD case there are second spatial derivatives in both $\mathbf{B}$ and $\mathbf{v}$. while the Hall MHD equations has second space derivatives in $\mathbf{B}$ but not in $\mathbf{v}$. The fact of having second derivatives of velocity is going to lead to a much more complex mathematical problem when trying to find solitary wave solutions, compared with the Hall case. The second derivatives of velocity with respect to

[9]The Vlasov equation governs the behavior of the distribution function, just as the Boltzmann equation does. According to [9], Vlasov equation differs from Boltzmann's one in assuming absence of collisions and including the effect of forces as the addition of external forces and averaged internal macroscopic fields. However, sometimes the name Vlasov equation is used for the collisionless Boltzmann's equation, without any additional difference.

spatial coordinates may remember to viscous terms. This is the reason why sometimes the concept of *gyroviscosity* is used. However, the physical mechanisms are completely different.

As a summary, the FLR Hall MHD model is described by

$$\frac{\partial \rho}{\partial t} + \nabla \cdot (\rho \mathbf{v}) = 0 \tag{2.39}$$

$$\frac{\partial}{\partial t}(\rho \mathbf{v}) + \nabla \cdot \left[\rho \mathbf{v}\mathbf{v} + \underset{\sim}{\mathbf{P}}_i + p_e \underset{\sim}{\mathbf{I}} + \frac{1}{4\pi}\left(\frac{1}{2}B^2 \underset{\sim}{\mathbf{I}} - \mathbf{B}\mathbf{B}\right)\right] = 0 \tag{2.40}$$

$$\frac{\partial \mathbf{B}}{\partial t} = \nabla \times \left[\mathbf{v} \times \mathbf{B} - \frac{m_i c}{4\pi e \rho}(\nabla \times \mathbf{B}) \times \mathbf{B}\right] \tag{2.41}$$

with $p_e = \rho v_{se}^2$ and $\underset{\sim}{\mathbf{P}}_i$ as defined through this section, with the double adiabatic equations for $p_\parallel$ and $p_\perp$. The next step is to particularize Equation (2.39)-(2.41) for one-dimensional traveling solutions, since the goal is to find solitary wave solutions.

2.3.1 FLR Hall MHD Dynamical System

The procedure explained in this subsection is based on *Finite Larmor radius influence on MHD solitary waves* [5] by Einar Mjølhus. However, when following the derivations in [5] and after a thorough validation of the equations, slightly different expressions have been obtained.

A reference frame is defined whose center moves with the wave velocity C and with the x axis pointing in the direction of propagation, i.e. perpendicular to the wavefront. The z axis is defined pointing in the direction of the magnetic field perpendicular to the propagation direction. Note that the reference frame defined in this way is inertial and, therefore, the momentum equation (2.40) is perfectly valid. Furthermore, due to the definition of solitary wave —it does not deform—, the problem becomes steady in this reference frame, i.e. $\frac{\partial}{\partial t} = 0$. On the other hand the solution is 1D, meaning that all variables change only in the propagation direction. This is $\frac{\partial}{\partial y} = \frac{\partial}{\partial z} = 0$ and, thus, the nabla operator is reduced to $\nabla = \frac{\partial}{\partial x}\mathbf{e}_x$ —being $\mathbf{e}_x$ the unitary vector in the x direction.

Solitary waves are solutions that propagate inside a medium in equilibrium. According to this statement, when $x \to \pm\infty$ the magnetic field value should tend to the ambient magnetic field

$$\mathbf{B}_0 = B_0 \cos\theta \mathbf{e}_x + B_0 \sin\theta \mathbf{e}_z \tag{2.42}$$

and the velocity to the upstream velocity

$$\mathbf{v}_0 = v_{0x}\mathbf{e}_x \tag{2.43}$$

with subindex "0" used to denote upstream conditions. In Equations (2.42) and (2.43), θ accounts for the angle between the propagation direction and the ambient

magnetic field. It has been made use also of the fact that the $\mathbf{B}_0$ component along $\mathbf{e}_y$ is zero due to the way the z axis has been defined. Due to the selected reference frame, the solution will be in terms of velocity relative to the wave velocity. Therefore the upstream value of the velocity is also relative. If the upstream fluid is considered to be in equilibrium at zero absolute velocity[10], the relative upstream velocity is $v_{0x} = -C$.

Note that the x component of Equation (2.41) under the 1D and stationary hypotheses yields the identity $0 = 0$, so that there is no equation for the evolution of B_x. This mathematical result has a physical meaning and can be easily seen from the magnetic divergence equation particularized for 1D problem $\nabla \cdot \mathbf{B} = \frac{\partial}{\partial x} B_x = 0$. The conclusion is that B_x must be constant with x ($B_x = B_0 \cos\theta$). In fact, if the steady assumption is dropped, 1D Equation (2.41) guarantees also $\frac{\partial}{\partial t} B_x = 0$, so that even if the problem is unsteady, B_x is constant in time and space.

The non-dimensional velocity vector $\mathbf{u}$ and perpendicular magnetic field vector $\mathbf{b}$ are defined as

$$\mathbf{u} = \frac{\mathbf{v}}{v_{0x}} = u_x \mathbf{e}_x + u_y \mathbf{e}_y + u_z \mathbf{e}_z \tag{2.44}$$

$$\mathbf{b} = \frac{B_y}{B_0 \sin\theta} \mathbf{e}_y + \frac{B_z}{B_0 \sin\theta} \mathbf{e}_z = b_y \mathbf{e}_y + b_z \mathbf{e}_z \tag{2.45}$$

with upstream values $u_x = b_z = 1$ and $u_y = u_z = b_y = 0$. Applying the one-dimensional and steady hypotheses to the continuity equation —Equation (2.39)— yields

$$\frac{\rho}{\rho_0} = \frac{1}{u_x} \tag{2.46}$$

which relates density and horizontal speed.

Let us introduce two additional auxiliary magnetic field variables

$$b^2 = b_y^2 + b_z^2 \tag{2.47}$$

$$\hat{b}^2 = \left(\frac{B}{B_0} \right)^2 = \cos^2\theta + b^2 \sin^2\theta \tag{2.48}$$

With the variables introduced so far an using Equation (2.46) to eliminate density, non-dimensional double adiabatic equations of state can be reached. Taking into account that constants in Equations (2.26) and (2.27) are equal to the upstream value of the left-hand side, the non dimensional pressures are defined as

$$P_{\parallel}(u, b^2) = \frac{p_{\parallel}}{p_{0\parallel}} = \frac{1}{\hat{b}^2 u^3} \tag{2.49}$$

[10] In case the plasma is at equilibrium with free stream velocity different from zero, an inertial reference frame in which the upstream plasma is seen at rest can always been defined.

$$P_{\perp}(u, b^2) = \frac{p_{\perp}}{p_{0\perp}} = \frac{\hat{b}}{u} \tag{2.50}$$

Dynamical system equations

The factor $m_i c/\left(4\pi e\rho\right)$ in Equation (2.41) can be expressed in terms of the ion upstream cyclotron frequency $\Omega_{ci,0}$, the Alfven speed[11] v_A, the upstream magnetic field magnitude B_0 and the local horizontal velocity as

$$\frac{m_i c}{4\pi e\rho} = \frac{m_i c}{eB_0}\,\frac{B_0^2}{4\pi\rho_0}\,\frac{\rho_0}{\rho}\,\frac{1}{B_0} = \frac{v_A^2}{\Omega_{ci,0}B_0}$$

where $v_A^2 = B_0^2/\left(4\pi\rho_0\right)$.

Working on Equation (2.41) with the explained hypotheses and introducing the nondimensional magnetic field and velocity vectors as defined in Equations (2.45) and (2.44) yields

$$\textbf{y:} \qquad \frac{d}{dx}\left[v_{0x}\left(-\sin\theta\, u_x b_y + \cos\theta\, u_y\right) + \frac{v_A^2}{\Omega_{ci,0}}\cos\theta\sin\theta\, u_x \frac{db_z}{dx}\right] = 0$$

$$\textbf{z:} \qquad \frac{d}{dx}\left[v_{0x}\left(-\sin\theta\, u_x b_z + \cos\theta\, u_z\right) - \frac{v_A^2}{\Omega_{ci,0}}\cos\theta\sin\theta\, u_x \frac{db_y}{dx}\right] = 0$$

where the x partial derivatives have been substituted by the absolute derivative, since it is the only derivative operator different from zero. Therefore, the expressions inside the brackets are constant and equal to their upstream value. Note also that upstream x derivatives are zero because the plasma is at equilibrium upstream. If one integrates above equations once, and divide them by $v_{0x}u_x\sin\theta$ nondimensional dynamical equations for magnetic field are obtained. Moreover the x coordinate distance is scaled with the characteristic length $\ell = v_A^2\cos\theta/\left(\Omega_{ci,0}v_{0x}\right)$. The parameter ℓ differs from the one used by Mjølhus in [5] by a $\cos\theta$ factor. In article [1] by the same author, he defines a characteristic length with the $\cos\theta$ included, and this definition agrees with the results of this work. The system then reads

$$\frac{d\mathbf{b}}{d\hat{x}} + \mathbf{G}(\mathbf{u}, \mathbf{b}) = 0 \tag{2.51}$$

being $\hat{x} = x/\ell$ and $\mathbf{G} = G_y\mathbf{e}_y + G_z\mathbf{e}_z$, with

[11] The Alfven speed is one of the characteristic velocities associated to small-amplitude wave modes in plasmas.

$$G_y = -\frac{u_z}{u_x}\frac{\cos\theta}{\sin\theta} + b_z - \frac{1}{u_x} \tag{2.52}$$

$$G_z = \frac{u_y}{u_x}\frac{\cos\theta}{\sin\theta} - b_y \tag{2.53}$$

Note that the first derivative in Equation (2.51) comes from the second spatial derivatives in (2.41) due to keeping the Hall term.

Following a similar procedure, one can obtain dynamical equations for velocity from Equation (2.40). As in the magnetic field case, a first integral of the equations can be directly computed, leading to three first order ordinary differential equations. In this case, the equations have been scaled with $\rho_0 v_{0x}^2$. The final equations are

$$\frac{\delta}{\hat{b}}\,\underset{\sim}{\mathbf{A}}\cdot\frac{d\mathbf{u}}{d\hat{x}} + \mathbf{F}(\mathbf{u},\mathbf{b}) = 0 \tag{2.54}$$

with $\delta = (v_\perp^2/v_A^2)\,P_\perp(u,b^2)/\cos\theta$, $v_\perp^2 = p_{0\perp}/\rho_0$, $\mathbf{F} = F_x\mathbf{e}_x + F_y\mathbf{e}_y + F_z\mathbf{e}_z$ and

$$F_x = u_x - 1 + P(u_x,b^2) + \frac{1}{2}M_A\sin^2\theta\left(b^2-1\right) \tag{2.55}$$

$$F_y = u_y + \chi(u_x,b^2)\cos\theta\sin\theta\,b_y \tag{2.56}$$

$$F_z = u_z + \left[\chi(u_x,b^2)b_z - \chi(1,1)\right]\cos\theta\sin\theta \tag{2.57}$$

The functions $P(u,b^2)$ and $\chi(u,b^2)$ are

$$\begin{aligned} P(u_x,b^2) = M_e\left(\frac{1}{u_x}-1\right) + M_i\Bigg\{ & P_\perp(u,b^2) - 1 + \\ & + \left[a_p P_\parallel(u,b^2) - P_\perp(u,b^2)\right]\frac{\cos^2\theta}{\hat{b}^2} - (a_p-1)\cos^2\theta\Bigg\} \end{aligned} \tag{2.58}$$

$$\chi(u_x,b^2) = M_i\left[a_p P_\parallel(u,b^2) - P_\perp(u,b^2)\right]\frac{1}{\hat{b}^2} - M_A \tag{2.59}$$

In Equations (2.55)-(2.59) the following parameters have been introduced:

$$M_e = v_{se}^2/v_{0x}^2 \tag{2.60}$$

$$M_i = v_\perp^2/v_{0x}^2 \tag{2.61}$$

$$M_A = v_A^2/v_{0x}^2 \tag{2.62}$$

$$a_p = p_{0\parallel}/p_{0\perp} \tag{2.63}$$

The tensor $\underset{\sim}{\mathbf{A}}$ in Equation (2.54), which comes from the FLR correction tensor (2.35)-(2.38), is

$$
\begin{aligned}
A_{11} &= 0 \\
A_{21} &= \hat{b}_z r_\perp \\
A_{31} &= -\hat{b}_y r_\perp \\
A_{12} &= -\hat{b}_z \left(r_\perp - 2\varepsilon \hat{b}_\parallel^2 \right) \\
A_{22} &= 2\varepsilon \hat{b}_\parallel \hat{b}_y \hat{b}_z \\
A_{32} &= -\hat{b}_\parallel \left(r_\parallel - 2\varepsilon \hat{b}_z^2 \right) \\
A_{13} &= \hat{b}_y \left(r_\perp - 2\varepsilon \hat{b}_\parallel^2 \right) \\
A_{23} &= \hat{b}_\parallel \left(r_\parallel - 2\varepsilon \hat{b}_y^2 \right) \\
A_{33} &= -2\varepsilon \hat{b}_\parallel \hat{b}_y \hat{b}_z
\end{aligned}
$$

but it can be expressed in a more elegant way as $\underset{\sim}{\mathbf{A}} = \underset{\sim}{\mathbf{I}} \times \mathbf{r} - 2\varepsilon \hat{\mathbf{b}} \hat{\mathbf{b}}_\parallel \times \hat{\mathbf{b}}_\perp$, in which new magnetic field auxiliary vector variables have been used[12]

$$\hat{\mathbf{b}}_\parallel = \hat{b}_x \mathbf{e}_x \tag{2.64}$$

$$\hat{\mathbf{b}}_\perp = \hat{b}_y \mathbf{e}_y + \hat{b}_z \mathbf{e}_z \tag{2.65}$$

$$\hat{\mathbf{b}} = \hat{\mathbf{b}}_\parallel + \hat{\mathbf{b}}_\perp \tag{2.66}$$

$$\hat{b}_x = \hat{b}_\parallel = B_x/B = \cos\theta/\hat{b} \tag{2.67}$$

$$\hat{b}_y = B_y/B = b_y \sin\theta/\hat{b} \tag{2.68}$$

$$\hat{b}_y = B_z/B = b_y \sin\theta/\hat{b} \tag{2.69}$$

and the vector $\mathbf{r}$ reads

$$\mathbf{r} = -r_\parallel \hat{\mathbf{b}}_\parallel + r_\perp \hat{\mathbf{b}}_\perp \tag{2.70}$$

$$r_\parallel = \frac{1}{2}\left(1 - 3\hat{b}_\parallel^2\right) + 2\varepsilon \hat{b}_\parallel^2 \tag{2.71}$$

$$r_\perp = \frac{1}{2}\left(1 + 3\hat{b}_\parallel^2\right) - 2\varepsilon \tag{2.72}$$

$$\varepsilon = \left(p_\perp - p_\parallel\right)/p_\perp = 1 - a_p P_\parallel / P_\perp \tag{2.73}$$

The inclusion of the FLR term in the pressure introduces second x derivatives of velocity in the system and as a result the velocity components are state variables of the dynamical system. In the Hall MHD case the magnetic field dynamical

[12] The same notation as he used in [5] has been used. The use of a lot of magnetic field variables, in order to reach compact expressions, may lead to some confusions. Realize that $\hat{\mathbf{b}} = \mathbf{e}_b$ and $\hat{b} \neq \left|\hat{\mathbf{b}}\right|$, because $\left|\hat{\mathbf{b}}\right| = |\hat{\mathbf{e}}_b| = 1$

equations are identical but the momentum equation leads to $\mathbf{F}(\mathbf{u}, \mathbf{b}) = 0$. These are three algebraic equations that relates the magnetic field with the velocity components. The Hall MHD dynamical system is bi-dimensional and much easier to deal with than the FLR Hall MHD one. The interested reader may find additional information on solitary waves in the Hall MHD model in reference [1] by E. Mjølhus and on shock waves in [14] by G. Sánchez-Arriaga.

It may be initially thought that one could isolate $d\mathbf{u}/dx$ in (2.54) by multiplying by $\hat{b}/\delta$ and the inverse of $\underset{\sim}{\mathbf{A}}$. However, it can be demonstrated that the determinant of $\underset{\sim}{\mathbf{A}}$ is equal to zero, so that $\underset{\sim}{\mathbf{A}}$ is singular. Equations (2.51) and (2.54) form a five-dimensional system. However the singularity of $\underset{\sim}{\mathbf{A}}$ restricts the set of possible solutions to the system. This property of $\underset{\sim}{\mathbf{A}}$ can be used to prove the existence of an invariant, i.e. an algebraic equation that defines a 4D hypersurface and restricts the 5D phase space. The invariant can be also understood as a reduction of the dimension of the state space from 5 to 4, since there exists an extra algebraic equation relating the state variables. The next step is to define the invariant and to use it to isolate $d\mathbf{u}/dt$ in Equation (2.54), following the procedure of [5].

Invariant in the FLR Hall MHD dynamical system

The tensor $\underset{\sim}{\mathbf{A}}$ is singular. As a consequence one its eigenvalues is zero, with associated right and left eigenvectors $\mathbf{R}$ and $\mathbf{L}$, respectively. By definition $\mathbf{R}$ and $\mathbf{L}$ satisfy

$$\mathbf{L} \cdot \underset{\sim}{\mathbf{A}} = 0 \tag{2.74}$$

$$\underset{\sim}{\mathbf{A}} \cdot \mathbf{R} = 0 \tag{2.75}$$

Solving this indeterminate system yields

$$\mathbf{L} = \frac{1}{\mu}\left(\mathbf{r} + 2\varepsilon\hat{b}_{\perp}^2\hat{\mathbf{b}}_{\parallel} - 2\varepsilon\hat{b}_{\parallel}^2\hat{\mathbf{b}}_{\perp}\right) \tag{2.76}$$

$$\mathbf{R} = \frac{1}{\mu}\mathbf{r} \tag{2.77}$$

where μ is an arbitrary constant. The additional condition $\mathbf{L} \cdot \mathbf{R} = 1$ can be imposed, in which case

$$\mu^2 = r_{\perp}^2\hat{b}_{\perp}^2 + r_{\parallel}^2\hat{b}_{\parallel}^2 - \gamma \tag{2.78}$$

with $\gamma = 2\varepsilon\hat{b}_{\perp}^2\hat{b}_{\parallel}^2$.

If one left multiplies Equation (2.54) by $\mathbf{L}$, the first addend in the left-hand side becomes zero ($\mathbf{L} \cdot \underset{\sim}{\mathbf{A}} = 0$), so that $\mathbf{L} \cdot \mathbf{F} = 0$ remains. Due to the singularity of the 1D FLR tensor, the solutions to the dynamical system must satisfy the algebraic relation $\mathbf{L} \cdot \mathbf{F} = 0$, which is the already anticipated invariant. Let us introduce the function $H(\mathbf{u}, \mathbf{b}) = \mathbf{L} \cdot \mathbf{F}$, being $H(\mathbf{u}, \mathbf{b}) = 0$ the invariant.

The next step is to use this invariant to reach an equation equivalent to (2.54) with $d\mathbf{u}/dx$ isolated in the left-hand side. To do so, it is required to define new vectors related to the eigenvalues of $\underset{\sim}{\mathbf{A}}$. Besides to zero, the 1D FLR tensor $\underset{\sim}{\mathbf{A}}$ can be proved to have imaginary eigenvalues $\pm i\mu$. The vectors $\mathbf{S}$ and $\mathbf{T}$ are determined in such a way that they satisfy

$$\underset{\sim}{\mathbf{A}} \cdot \mathbf{S} = -\mu \mathbf{T} \tag{2.79}$$

$$\underset{\sim}{\mathbf{A}} \cdot \mathbf{T} = \mu \mathbf{S} \tag{2.80}$$

which yields

$$\mathbf{S} = \frac{1}{\mu \hat{b}_\perp \hat{b}_\parallel} \left[\left(\hat{b}_\perp^2 r_\perp - \gamma \right) \hat{\mathbf{b}}_\parallel + \left(\hat{b}_\parallel^2 r_\parallel - \gamma \right) \hat{\mathbf{b}}_\perp \right] \tag{2.81}$$

$$\mathbf{T} = \frac{1}{\hat{b}_\perp \hat{b}_\parallel} \left(\hat{\mathbf{b}}_\parallel \times \hat{\mathbf{b}}_\perp \right) \tag{2.82}$$

Similarly, vectors $\mathbf{M}$ and $\mathbf{N}$ fulfill

$$\mathbf{M} \cdot \underset{\sim}{\mathbf{A}} = \mu \mathbf{N} \tag{2.83}$$

$$\mathbf{N} \cdot \underset{\sim}{\mathbf{A}} = -\mu \mathbf{M} \tag{2.84}$$

and have expressions

$$\mathbf{M} = \frac{1}{\mu \hat{b}_\perp \hat{b}_\parallel} \left(\hat{b}_\perp^2 r_\perp \hat{\mathbf{b}}_\parallel + \hat{b}_\parallel^2 r_\parallel \hat{\mathbf{b}}_\perp \right) \tag{2.85}$$

$$\mathbf{N} = \mathbf{T} \tag{2.86}$$

Vectors $\mathbf{L}$, $\mathbf{R}$, $\mathbf{S}$, $\mathbf{T}$, $\mathbf{M}$ and $\mathbf{N}$ defined by Equations (2.76)-(2.86) can be verified to satisfy the normalization and orthogonality conditions

$$\mathbf{L} \cdot \mathbf{R} = \mathbf{M} \cdot \mathbf{S} = \mathbf{T} \cdot \mathbf{N} = 1$$

$$\mathbf{M} \cdot \mathbf{R} = \mathbf{N} \cdot \mathbf{R} = \mathbf{L} \cdot \mathbf{S} = \mathbf{L} \cdot \mathbf{T} = \mathbf{N} \cdot \mathbf{S} = \mathbf{M} \cdot \mathbf{T} = 0$$

On the other hand, the change of variable

$$\frac{\delta}{\hat{b}} \frac{d\mathbf{u}}{d\hat{x}} = \mathbf{w} \tag{2.87}$$

can be made on Equation (2.54). Equation (2.87) is an explicit expression for $d\mathbf{u}/dx$ —once multiplied by $\hat{b}/\delta$. The rest of the section will be devoted to obtaining the components of $\mathbf{w}$. Note that this change of variable applied in Equation (2.54) implies

$$\underset{\sim}{\mathbf{A}} \cdot \mathbf{w} = -\mathbf{F} \tag{2.88}$$

that is an algebraic set of equations from which it will be tried to obtain expressions for the components of $\mathbf{w}$ —it is known beforehand that we are not going to be

able to completely determine $\mathbf{w}$ from Equation (2.88), since it is an indeterminate system. In order to solve the problem of defining $\mathbf{w}$, a basis formed by $\mathbf{R}$, $\mathbf{S}$ and $\mathbf{T}$ is very convenient —since they right multiply $\underset{\sim}{\mathbf{A}}$ in (2.88). Note that this basis is neither normal nor orthogonal. Let us write $\mathbf{F}$ and $\mathbf{w}$ as

$$\mathbf{F} = F_R\,\mathbf{R} + F_S\,\mathbf{S} + F_T\,\mathbf{T} \tag{2.89}$$

$$\mathbf{w} = w_R\,\mathbf{R} + w_S\,\mathbf{S} + w_T\,\mathbf{T} \tag{2.90}$$

The vector function $\mathbf{F}$ is known —in terms of the state variables— so that the components in the new basis can be obtained from Equation (2.89). Dot-multiplying this expression by $\mathbf{L}$, $\mathbf{M}$ and $\mathbf{N}$ —respectively— and using the orthogonality and normalization conditions, the components of $\mathbf{F}$ in the new basis read

$$F_R = \mathbf{L}\cdot\mathbf{F} = 0 \tag{2.91}$$

$$F_S = \mathbf{M}\cdot\mathbf{F} \tag{2.92}$$

$$F_T = \mathbf{N}\cdot\mathbf{F} \tag{2.93}$$

Introducing Equations (2.89)-(2.93) in (2.88) and using the relations (2.75), (2.79) and (2.80) yields

$$\underset{\sim}{\mathbf{A}}\cdot(w_R\,\mathbf{R} + w_S\,\mathbf{S} + w_T\,\mathbf{T}) = -\left[(\mathbf{M}\cdot\mathbf{F})\;\mathbf{S} + (\mathbf{N}\cdot\mathbf{F})\;\mathbf{T}\right]$$

$$\mu w_T\mathbf{S} - \mu w_S\mathbf{T} = -\left[(\mathbf{M}\cdot\mathbf{F})\;\mathbf{S} + (\mathbf{N}\cdot\mathbf{F})\;\mathbf{T}\right] \tag{2.94}$$

By in identifying terms in the right and the left hand sides of the previous expression, one finds

$$w_S = (\mathbf{N}\cdot\mathbf{F})/\mu \tag{2.95}$$

$$w_T = -(\mathbf{M}\cdot\mathbf{F})/\mu \tag{2.96}$$

From Equation (2.94), it follows, again, $\mathbf{L}\cdot\mathbf{F} = 0$. Otherwise $F_R \neq 0$ and Equation (2.94) would lead to the conclusion that the system is incompatible.

As predicted, $\mathbf{w}$ cannot be completely determined using only Equation (2.88). An extra condition is required and this is $dH/d\hat{x} = 0$. That is to say, the integration of the dynamical system must be started with an initial condition fulfilling $H(\mathbf{u},\mathbf{b}) = 0$, but this must be also satisfied for all subsequent $\hat{x}$ points. If in addition to the proper initial condition, $dH/d\hat{x} = 0$ is imposed, the agreement of the solution with the invariant is guaranteed. The $\hat{x}$ derivative of the invariant reads

$$\frac{dH}{d\hat{x}} = \frac{\partial H}{\partial \mathbf{u}}\cdot\frac{d\mathbf{u}}{d\hat{x}} + \frac{\partial H}{\partial \mathbf{b}}\cdot\frac{d\mathbf{b}}{d\hat{x}} = \frac{\hat{b}}{\delta}\frac{\partial H}{\partial \mathbf{u}}\cdot\mathbf{w} - \frac{\partial H}{\partial \mathbf{b}}\cdot\mathbf{G} = 0 \tag{2.97}$$

where Equations (2.51) and (2.87) have been used to substitute the $\hat{x}$ derivatives of velocity and magnetic field vectors. Operating with this equation one can reach an expression for w_R

$$w_R = -\frac{w_S \Gamma_S - \Gamma_b/\hat{b}}{\Gamma_R} \tag{2.98}$$

with

$$\Gamma_R = \frac{\partial H}{\partial \mathbf{u}} \cdot \mathbf{R}$$
$$\Gamma_S = \frac{\partial H}{\partial \mathbf{u}} \cdot \mathbf{S}$$
$$\Gamma_b = \delta \frac{\partial H}{\partial \mathbf{b}} \cdot \mathbf{G}$$

defined according to [5]. Moreover the gradient of $H(\mathbf{u}, \mathbf{b})$ with respect to $\mathbf{u}$ and $\mathbf{b}$ can be obtained in terms of $\mathbf{F}$ and $\mathbf{L}$ and their corresponding derivative tensors

$$\frac{\partial H}{\partial \mathbf{u}} = \frac{\partial L}{\partial \mathbf{u}} \cdot \mathbf{F} + \frac{\partial F}{\partial \mathbf{u}} \cdot \mathbf{L}$$
$$\frac{\partial H}{\partial \mathbf{b}} = \frac{\partial L}{\partial \mathbf{b}} \cdot \mathbf{F} + \frac{\partial F}{\partial \mathbf{b}} \cdot \mathbf{L}$$

Note that $\frac{\partial H}{\partial \mathbf{u}} \cdot \mathbf{T} = 0$, since $\mathbf{L} \cdot \mathbf{T} = 0$ and $\frac{\partial L}{\partial \mathbf{u}} \cdot \mathbf{F}$ is along $\mathbf{e}_x$ —because the derivatives of $\mathbf{L}$ with respect to u_y and u_z are all zero— while $\mathbf{T}$ is perpendicular to $\mathbf{e}_x$ —see Equation (2.82)—, so that $\left(\frac{\partial L}{\partial \mathbf{u}} \cdot \mathbf{F}\right) \cdot \mathbf{T} = 0$ also.

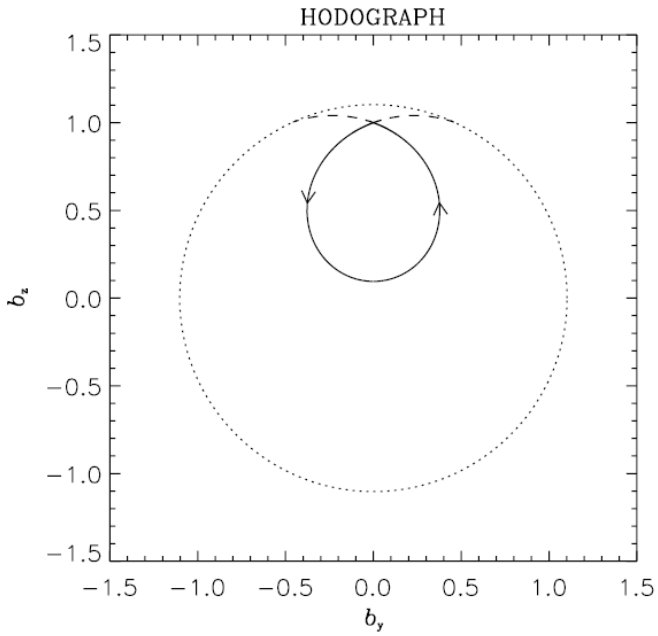

Figure 2.1: Magnetic hodograph from [1].
Dotted line: sonic circle. Broken line: solution departing from the upstream value of $\mathbf{b}$ and hitting the sonic circle.

Finally, we note that whenever $\Gamma_R \to 0$ the variable $w_R \to \infty$ and so does $d\mathbf{u}/dx$. There is a singularity at $\Gamma_R = 0$ which must be taken into account in the

development of the algorithm in charge of finding solitary wave solutions. The existence of this singularity reminds to singularities also present in the Hall MHD case: the so-called *sonic circle* —since it is a circle in the state space formed by b_z and b_y, see Figure 2.1—, which limits the values of b^2 within certain interval —more details in reference [1]. There is at least one sonic circle existing no matter the combination of the problem parameters. However, the FLR Hall MHD system is more complex due to the greater number of dimensions of the state space and the solution to $\Gamma_R(\mathbf{u}, \mathbf{b}) = 0$ would lead to a 4D hypersurface in the 5D state space in which the singularity takes place, so that it is not expected that investigating $\Gamma_R(\mathbf{u}, \mathbf{b}) = 0$ lead to such an elegant and simple solution as the sonic circle is.

Discrepancies on the final equations with respect to *Finite Larmor radius influence on MHD solitary waves* [5] by E. Mjølhus

The last part of this chapter is a summary of the main differences found in the Equations of [5] with respect to the dynamical system equations showed in this subsection. All the equations have been derived and compared to those in [5]. Moreover, whenever possible, analytical and numerical outputs of some expressions have been compared and in some cases a cross-check have been made by comparison with other references.

1. There is a $\cos\theta$ factor included inside the characteristic length ℓ used to scale x that does not appear in the definition of ℓ in [5]. However, the characteristic length defined in [1] by the same author coincides with the definition used in this work. This difference does not affect the final results, since parameter ℓ is included inside $d\hat{x}$ and the solution is given in terms of $\hat{x}$.

2. The expression given in [5] for the 1D FLR tensor is $\underset{\sim}{\mathbf{A}} = \underset{\sim}{\mathbf{I}} \times \mathbf{r} + 2\varepsilon \hat{\mathbf{b}}\,\hat{\mathbf{b}}_{\parallel} \times \hat{\mathbf{b}}_{\perp}$. However, following the process in [5], equation $\underset{\sim}{\mathbf{A}} = \underset{\sim}{\mathbf{I}} \times \mathbf{r} - 2\varepsilon \hat{\mathbf{b}}\,\hat{\mathbf{b}}_{\parallel} \times \hat{\mathbf{b}}_{\perp}$ has been reached. The equations for the eigenvectors and eigenvalues of $\underset{\sim}{\mathbf{A}}$, as well as the orthogonality and normalization conditions, in the paper coincide with those derived in this thesis.

3. There is a $\hat{b}$ dividing δ in Equations (2.54) and (2.87) coming from the cyclotron frequency appearing in the FLR pressure tensor. This $1/\hat{b}$ factor does not appear in the corresponding equations of [5].

4. The difference on the $1/\hat{b}$ factor, affects also the equation giving the component of $\mathbf{w}$ along the direction defined by $\mathbf{R}$, i.e. w_R. The expression for w_R used in this work is given by Equation (2.98).

5. Note that, in Equation (2.98), the "–" sign in the numerator differs from equation (46) of [5].

6. In Equation (2.52) giving G_y the last term in the right-hand is $1/u_x$, while in [5] it is 1.

2.3.2 FLR Hall MHD Dispersion Relations

Let us consider a plasma —satisfying the assumptions behind the FLR Hall MHD model— at equilibrium. One may study the existence of small amplitude waves at these conditions. These are solutions to the system oscillating spatially and temporally around the equilibrium magnitudes ρ_0, $\mathbf{v}_0$ and $\mathbf{B}_0$. The type of solutions described can be expressed mathematically as

$$\hat{\rho}(\hat{x},\tau) = 1 + \hat{\rho}_1\, e^{i(k\hat{x}-\omega\tau)}$$

$$\mathbf{u}(\hat{x},\tau) = \mathbf{u}_0 + \mathbf{u}_1\, e^{i(k\hat{x}-\omega\tau)}$$

$$\mathbf{b}(\hat{x},\tau) = \mathbf{b}_0 + \mathbf{b}_1\, e^{i(k\hat{x}-\omega\tau)}$$

being $\mathbf{u}_0 = 1\,\mathbf{e}_x$, $\mathbf{b}_0 = 1\,\mathbf{e}_z$, $\mathbf{u}_1 = u_{1x}\mathbf{e}_x + u_{1y}\mathbf{e}_y + u_{1z}\mathbf{e}_z$ and $\mathbf{b}_1 = b_{1y}\mathbf{e}_y + b_{1z}\mathbf{e}_z$, with terms of first order much lower than zeroth-order ones. The variable $\hat{\rho}$ is non-dimensional density, being ρ_0 the characteristic density. The non-dimensional coordinate $\hat{x}$ is again with respect to a moving reference frame with velocity C along x, and τ is time normalized with ℓ/v_{0x}. Since the analysis is made with non-dimensional equations, the variables k and ω are normalized wavenumber and frequency —with $1/\ell$ and v_{0x}/ℓ—, respectively.

Perturbing the longitudinal magnetic field is not needed, since it has been reasoned and mathematically proved that B_x must be constant in both space and time. If the x component of the magnetic field is perturbed, the equations will lead us again to the same conclusion.

Equations (2.39)-(2.41) can be converted into non-dimensional form using the non-dimensional variables defined in this section and those used for the FLR Hall MHD dynamical system. Note that in this case, the steadiness assumption is not kept, but equations are particularized for 1D waves —i.e. only spatial derivatives with respect to x are maintained, so that $\nabla = \partial/\partial x\,\mathbf{e}_x$. The nondimensional FLR Hall MHD system of equations reads

$$\frac{\partial\hat{\rho}}{\partial\tau} + \frac{\partial}{\partial\hat{x}}\left(\hat{\rho}u_x\right) = 0 \tag{2.99}$$

$$\begin{aligned}\frac{\partial}{\partial\tau}\left(\hat{\rho}\mathbf{u}\right) + \nabla\cdot\Big[\hat{\rho}\mathbf{u}\mathbf{u} + M_e\hat{\rho}\underset{\sim}{\mathbf{I}} + M_i\hat{\underset{\sim}{\mathbf{P}}}_i^{(0)} + \\ + M_A\sin^2\theta\left(\frac{1}{2}\hat{B}^2\underset{\sim}{\mathbf{I}} - \hat{\mathbf{B}}\hat{\mathbf{B}}\right) + \frac{M_i}{M_A\cos\theta}\underset{\sim}{\mathbf{\Pi}}\Big] = 0\end{aligned} \tag{2.100}$$

$$\frac{\partial\hat{\mathbf{B}}}{\partial\tau} = \nabla\times\left(\mathbf{u}\times\hat{\mathbf{B}}\right) - \mathbf{e}_x\times\frac{\partial}{\partial\hat{x}}\left(\frac{1}{\hat{\rho}}\frac{\partial\mathbf{b}}{\partial\hat{x}}\right) \tag{2.101}$$

with [13]

$$\hat{\underset{\sim}{\mathbf{P}}}_i^{(0)} = a_p\hat{\rho}^3/\hat{b}^2\,\mathbf{e}_b\mathbf{e}_b + \hat{\rho}\hat{b}\left(\underset{\sim}{\mathbf{I}} - \mathbf{e}_b\mathbf{e}_b\right) = a_pP_{\parallel}\,\mathbf{e}_b\mathbf{e}_b + P_{\perp}\left(\underset{\sim}{\mathbf{I}} - \mathbf{e}_b\mathbf{e}_b\right) \tag{2.102}$$

[13] In this case, Equation (2.46) cannot be used, so that pressures must be expressed in terms of $\hat{\rho}$, but not u_x. Equations (2.49) and (2.50) do not hold here.

$$\hat{\mathbf{B}} = \frac{1}{\tan\theta}\mathbf{e}_x + \mathbf{b} \tag{2.103}$$

and $\underset{\sim}{\mathbf{\Pi}}$ accounts for the FLR tensor, of which only the first row

$$\mathbf{e}_x \cdot \underset{\sim}{\mathbf{\Pi}} = \Pi_{xx}\mathbf{e_x} + \Pi_{xy}\mathbf{e_y} + \Pi_{xz}\mathbf{e_z} = \frac{P_\perp}{\hat{b}}\underset{\sim}{\mathbf{A}} \cdot \frac{\partial \mathbf{u}}{\partial \hat{x}} \tag{2.104}$$

is needed because of the one-dimensional simplification. The tensor $\underset{\sim}{\mathbf{A}}$ is given by the expressions in the previous section —but with pressures expressed in terms of density as in Equation (2.102).

If Equations (2.99)-(2.104) are particularized for small amplitude wave-like solutions, an algebraic linear system of equations is obtained —the exponential terms will eventually vanish from the equations.

Linear continuity equation :

$$k u_{1x} + (k - \omega)\,\hat{\rho}_1 = 0 \tag{2.105}$$

Linear momentum equations :

$$(k-\omega)\,u_{1x} + M_e k\,\hat{\rho}_1 + M_i k\,P_{1x} + M_A k \sin^2\theta\, b_{1z} + \\ + \frac{M_i}{M_A\cos\theta} k\,\Pi_{1xx} = 0 \tag{2.106}$$

$$(k-\omega)\,u_{1y} + M_i k\,P_{1y} - M_A k\cos\theta\sin\theta\, b_{1y} + \frac{M_i}{M_A\cos\theta} k\,\Pi_{1xy} = 0 \tag{2.107}$$

$$(k-\omega)\,u_{1z} + M_i k\,P_{1z} - M_A k\cos\theta\sin\theta\, b_{1z} + \frac{M_i}{M_A\cos\theta} k\,\Pi_{1xz} = 0 \tag{2.108}$$

Linear magnetic induction equations :

$$(k-\omega)\,b_{1y} - \frac{1}{\tan\theta} k\,u_{1y} - ik^2\,b_{1z} = 0 \tag{2.109}$$

$$(k-\omega)\,b_{1z} + k\,u_{1x} - \frac{1}{\tan\theta} k\,u_{1z} + ik^2\,b_{1y} = 0 \tag{2.110}$$

The double adiabatic first-order pressure terms

$$P_{1x} = \left[1 + (3a_p - 1)\cos^2\theta\right]\hat{\rho}_1 + \sin^2\theta\left(1 - 4a_p\cos^2\theta\right) b_{1z} \tag{2.111}$$

$$P_{1y} = (a_p - 1)\cos\theta \sin\theta \, b_{1y} \tag{2.112}$$

$$P_{1z} = \cos\theta \sin\theta \left[(3a_p - 1)\,\hat{\rho}_1 + \left(4a_p \cos^2\theta - 3a_p - \cos^2\theta\right) b_{1z}\right] \tag{2.113}$$

appeared in these equations, together with the first-order FLR pressure terms

$$\Pi_{1xx} = -\frac{1}{2} i \, \sin\theta \left(1 - 5\cos^2\theta + 8a_p \cos^2\theta\right) k \, u_{1x} \tag{2.114}$$

$$\begin{aligned}\Pi_{1xy} = &\frac{1}{2} i \, \sin\theta \left(1 - \cos^2\theta + 4a_p \cos^2\theta\right) k \, u_{1x} + \\ &+ \frac{1}{4} i \, \cos\theta \left(4 - 2\sin^2\theta - 8a_p \cos^2\theta\right) k \, u_{1z}\end{aligned} \tag{2.115}$$

$$\Pi_{1xz} = \frac{1}{4} i \, \cos\theta \left[-3 - \cos^2\theta + 9\sin^2\theta + 8a_p \left(\cos^2\theta - \sin^2\theta\right)\right] k \, u_{1y} \tag{2.116}$$

Equations (2.105)-(2.110) can be arranged and expressed in matrix form as $\underset{\sim}{\mathbf{D}}(k,\omega) \cdot \mathbf{z}_1 = 0$, with $\mathbf{z}_1 = (\hat{\rho}_1, u_{1x}, u_{1y}, u_{1z}, b_{1y}, b_{1z})^T$. In order for this matrix equation to have solutions different than the trivial one, the determinant of $\underset{\sim}{\mathbf{D}}$ has to be zero. This provides an algebraic equation relating the value of the wavenumber k with the frequency ω. Therefore, this equation can be solved for several real values of k and obtain solutions $\omega = \omega(k)$. In fact, for each k there are six values of ω satisfying $\det(\underset{\sim}{\mathbf{D}}) = 0$, associated to different wave modes. Of course, one may have different modes depending also on the parameters of the problem, i.e. M_A, M_i, M_e, a_p and θ.

The solutions $\omega = \omega(k)$ are called *dispersion relations*. The concept of dispersion refers to the physical phenomena of a wave which separates into its elementary wave components. A small-amplitude wave mode is composed by a linear combination of the waves satisfying the dispersion relation $\omega = \omega(k)$ of that particular mode —these are the cited elementary components. If the phase velocity ω/k of the elementary waves is a function of the wavenumber k, the result is that wave components will propagate in space at different velocities depending on their wavelengths and, as a result, the different components separate.

There is no dispersion in the case of the pure MHD model. To see this fact just drop the Hall and FLR terms in the linearized equations, which are easy to identify —the double adiabatic model can be maintained, there is no need of returning to the scalar pressure case. In this case the matrix equation $\underset{\sim}{\mathbf{D}}(k,\omega) \cdot \mathbf{z}_1 = 0$ can be expressed as $\underset{\sim}{\mathbf{D}}(\omega/k) \cdot \mathbf{z}_1 = 0$, i.e. in terms of the phase velocity. Solving $\det(\underset{\sim}{\mathbf{D}}) = 0$ will deliver results $\omega/k = \text{const.}$, meaning that the phase velocity of one particular mode is independent on the wavelength of the wave components. When Hall and FLR effects are introduced in the model, dispersion is being also introduced.

The study of the dispersion relations of one plasma model provides relevant information about the plasma. They are also important in terms of stability. If for certain range of k there are ω solutions with positive imaginary part, that range of wave numbers leads to unstable small-amplitude solutions that will grow

exponentially in time. It must be remarked that this analysis refers to the stability of the equilibrium, without taking int account the presence of a solitary wave.

For the project exposed in this thesis, dispersion relations will be relevant and should be taking into account for stability purposes at small amplitudes in numerical simulations of the time evolution of a particular solitary wave. To be precise, once a theoretical solitary wave solution has been found and computed in the FLR Hall MHD dynamical system, it can be used as initial condition to solve the system of unsteady 1D partial differential equations. If the solitary wave is stable, the solution should not deform and remain static with respect to the moving reference frame —i.e. the solution is steady, although the equations take into account any possible unsteadyness. It must be strongly highlighted that the stability analysis based on dispersion relations is only valid at small amplitudes close to the equilibrium state, because stability is assessed on the upstream state without taking into account the presence of a solitary wave. Therefore, dispersion relations can only predict instability at the tails of the solitary wave, where the value of the state variables is very close to the equilibrium state and, thus, the linear analysis is valid. If the Fourier transform of the state variables characterizing the initial state of the solitary wave reveals that it has large energy associated to unstable wavenumbers —according to the dispersions relations—, one may observe instabilities at the small amplitudes in the tails when computing the time evolution. If this is the case, the wave will not persist in the simulation since any perturbation on small amplitudes will grow in time. However, the nonexistence of linear instabilities does not guarantee that the solitary wave is stable.

In later chapters a brief insight on this type of simulation will be given, together with dispersion relations results. The results from this type of simulations are important when assessing the stability of the solitary waves. However, this project is more focused on the subject of existence of solutions. The non-dimensional FLR Hall MHD equations and the dispersion relations have been provided by Dr. Thierry Passot from Observatoire de la Côte d'Azur, whose research group is actively collaborating with Dr. Gonzalo Sánchez Arriaga and the author on the subject of solitary waves on space plasmas. These equations have been also useful as a double check in the validation process of the dynamical system equations.

Chapter 3

Basic Theory of Dynamical Systems

This chapter discusses some basic principles of dynamical systems that are relevant for the analysis of solitary waves. The theoretical aspects described here have been needed for understanding the problem, from a mathematical point of view, and the development of the algorithms. Some of this theory is general and applies to other dynamical system than the concerning one for this thesis.

Equations (2.51) and (2.87) form a nonlinear dynamical system. It can be written as

$$\frac{d\mathbf{z}}{dx} = \mathbf{f}(\mathbf{z}, x; \boldsymbol{\mu}) \tag{3.1}$$

where $\mathbf{z}$ is the state vector, x is the independent variable and $\boldsymbol{\mu}$ stands for the vector of parameters. In the FLR Hall MHD dynamical system

$$\mathbf{z} = \begin{bmatrix} u_x & u_y & u_z & b_y & b_z \end{bmatrix} \tag{3.2}$$

and

$$\boldsymbol{\mu} = \begin{bmatrix} C/v_A & v_\perp/v_A & v_{se}/v_\perp & a_p & \theta \end{bmatrix} \tag{3.3}$$

The vector function $\mathbf{f}$ defines a vector field in the phase space, and depends on the position in the phase space, on the parameters of the system and on the independent variable, in the most general case. The solution $\mathbf{z}(x)$ to the dynamical system (3.1) depends on the parameters and on the initial condition $\mathbf{z}(0) = \mathbf{z}_0$.

The dynamical system built from the Hall-MHD FLR model proposed in the previous chapter is autonomous —i.e. it does not depend explicitly on the independent variable. So that, in coming sections, the system (3.1) will be assumed to be also autonomous. Moreover, the dependency on $\boldsymbol{\mu}$ will be omitted in order to use a more compact notation

$$\frac{d\mathbf{z}}{dx} = \mathbf{f}(\mathbf{z}) \tag{3.4}$$

3.1 Equilibrium solutions, stability and reversibility

Mathematically an equilibrium point is defined as $\frac{d\mathbf{z}}{dt}\Big|_{\mathbf{z}=\mathbf{z}_e} = 0$. Therefore, equilibrium points $\mathbf{z}_e$ are solutions to the algebraic system of equations $\mathbf{f}(\mathbf{z}_e) = 0$. This solutions may be found analytically, in some cases. However, in general, numerical methods are needed to solve this type of equations, especially as the degree of complexity of the system increases. One of the most popular choices is Newton method. The convergence to the solution depends on the point at which we decide to start the numerical algorithm. Making a good initial guess to begin the numerics becomes more and more difficult as the number of dimensions of the system increases.

Note that, according to the definition of equilibrium points, if the system (3.4) is integrated with initial conditions $\mathbf{z}(0) = \mathbf{z}_e$, the solution is $\mathbf{z}(x) = \mathbf{z}_e$ for every x. However, this only would occur at the exact equilibrium points. It is interesting to study the response to a small perturbation from the equilibrium position.

3.1.1 Stability of equilibrium positions

The dynamic stability analysis studies the evolution of the solution when the equilibrium is perturbed. A small disturbance $\mathbf{y}(t)$ is added to the equilibrium point $\mathbf{z}_e$

$$\mathbf{z}(x) = \mathbf{z}_e + \mathbf{y}(x) \tag{3.5}$$

If Equation (3.5) is substituted in (3.4), and linearized using Taylor series, one finds

$$\frac{d\mathbf{y}}{dt} = \mathbf{f}(\mathbf{z}_e + \mathbf{y}) \simeq \mathbf{f}(\mathbf{x}_e) + \underset{\sim}{\mathbf{J}} \cdot \mathbf{y} = \underset{\sim}{\mathbf{J}} \cdot \mathbf{y} \tag{3.6}$$

where the fact that $\mathbf{f}(\mathbf{x}_e) = 0$ has been used.

The matrix $\underset{\sim}{\mathbf{J}}$ in Equation (3.6) is the Jacobian matrix of $\mathbf{f}(\mathbf{x})$ evaluated at $\mathbf{x} = \mathbf{x}_e$. The Jacobian matrix is defined as[1]:

[1]Realize that the definition of Jacobian matrix used in mathematics differs from the one used in fluid dynamics. The mathematic definition keeps derivatives with respect to the same variable in columns, while the second one places these derivatives in rows. The Jacobian matrix used in fluid mechanics is the transpose of the Jacobian as defined by (3.7).

$$\underset{\sim}{\mathbf{J}} = \left[\begin{array}{cccc} \frac{\partial f_1}{\partial z_1} & \frac{\partial f_1}{\partial z_2} & \cdots & \frac{\partial f_1}{\partial z_n} \\ \frac{\partial f_2}{\partial z_1} & \frac{\partial f_2}{\partial z_2} & \cdots & \frac{\partial f_2}{\partial z_n} \\ \vdots & \vdots & \ddots & \vdots \\ \frac{\partial f_n}{\partial z_1} & \frac{\partial f_n}{\partial z_2} & \cdots & \frac{\partial f_n}{\partial z_n} \end{array}\right]\Bigg|_{\mathbf{z}=\mathbf{z}_e} \tag{3.7}$$

The evolution of the perturbation can be computed by solving Equation (3.6), giving an initial condition for $\mathbf{y}$. The linearization performed in (3.6) implies that the solution is valid as long as it remains very close to the equilibrium point. If one tries solutions for $\mathbf{y}$ with form $\mathbf{u}e^{\lambda t}$ and develops Equation (3.6), the result is the eigenvalue problem

$$\left(\underset{\sim}{\mathbf{J}} - \lambda \underset{\sim}{\mathbf{I}}\right) \cdot \mathbf{u} = 0 \tag{3.8}$$

Equation (3.8) gives n different eigenvalues and eigenvectors, and thus n solutions of $\mathbf{y}$ —being n the dimension of the system. Note that if the elements of $\underset{\sim}{\mathbf{J}}$ are real and if one eigenvalue is complex, then its complex conjugate is also an eigenvalue. Since the problem is linear, the complete solution

$$\mathbf{y}(x) = \sum_{i=1}^{n} c_i \mathbf{u}_i e^{\lambda_i x} \tag{3.9}$$

is obtained by applying superposition[2].

From Equation (3.9), one may realize that, in order for the equilibrium point to be stable —i.e. the perturbation decays— the real part of all the eigenvalues values must be negative. Otherwise the perturbation would grow exponentially, and at some point, the linear solution of $\mathbf{y}(x)$ is not valid anymore, since nonlinear effects would come into play. The imaginary part of the eigenvalues introduce oscillations in the solution. This can be proved by developing the exponential of an imaginary number according to Euler formula. In case all eigenvalues have negative real part, but some of them have null real part, the system is said to be critically stable.

For later use, the concepts of stable and unstable manifold of the equilibrium solution are now introduced. The stable manifold of a particular equilibrium can be defined as the set of orbits in the state space that approach the equilibrium as $x \to \infty$. Similarly, the unstable manifold comprise the orbits that tend to the equilibrium point as $x \to -\infty$. The local approximations of the stable and unstable manifolds close to the equilibrium are given by the eigenvectors of $\underset{\sim}{\mathbf{J}}$ linked to

[2]Only the case in which matrix $\underset{\sim}{\mathbf{J}}$ has n different eigenvalues is being considered, since the goal of this section is not to provide a complete theory of dynamical systems, but expose the tools that have been needed for the accomplishment of this work

negative and positive real-part eigenvalues, respectively. Far from the equilibrium, the stable and unstable manifolds may be strongly driven by the nonlinearities of the system.

All the previous concepts allow the location of the equilibrium positions in the state space and the assessment of their stability properties for certain value of the system parameters $\boldsymbol{\mu}$, i.e. for certain location in the parameter space. However, if $\boldsymbol{\mu}$ is modified the dynamics of the system will change, in general. There exist a wide variety of possible phenomena that may occur under changes of the parameters, e.g. destruction and creation of equilibrium positions, changes in the stability properties of one particular solution, etc.

The present project is highly related to the analysis of the change in the dynamical behavior, manifolds and stability of the system in the parameter space. In the case of the Hall-MHD model with FLR effect, there exist an equilibrium solution that keeps its position in the state space for any value of $\boldsymbol{\mu}$, i.e. the upstream state $[u_x, u_y, u_z, b_y, b_z] = [1, 0, 0, 0, 1]$. However the dynamics of the system do change with $\boldsymbol{\mu}$, as well as the stability properties of the fixed point. In fact the type of solutions one may find around the equilibrium is very rich, since the state space is four-dimensional.

3.1.2 Reversibility and Stability in 4D reversible dynamical systems

This subsection defines the concept of reversibility, as well as it gives an introduction to the stability of equilibrium states in 4D dynamical systems.

Reversibility

The concept of reversibility as defined in this section is going to be of paramount importance in the existence of solitary wave solutions and in the design of an algorithm capable of finding symmetric solitary wave solutions to the FLR Hall MHD dynamical system.

Reversibility is defined here, following article [2] by A.R. Champneys, for systems with an even number of dimensions —remind that the FLR system state space has five dimensions which are reduced to four once an invariant has been demonstrated to exist. A dynamical system is said to be reversible if the equations governing the dynamics remain the same under a reversal of x and half the state variables. That is to say, the system of equations —in the FLR case Equations (2.51) and (2.87)— are just kept equal under the following changes —let us take a 4D dynamical system as an example

$$x \longrightarrow (-x)$$
$$[z_1(x),\ z_2(x),\ z_3(x),\ z_4(x)] \longrightarrow [z_1(-x),\ -z_2(-x),\ z_3(-x),\ -z_4(-x)]$$

As a consequence, the x derivatives undergo the transformation

$$\left[\frac{dz_1}{dx}(x),\ \frac{dz_2}{dx}(x),\ \frac{dz_3}{dx}(x),\ \frac{dz_4}{dx}(x)\right] \longrightarrow \left[-\frac{dz_1}{dx}(-x),\ \frac{dz_2}{dx}(-x),\ -\frac{dz_3}{dx}(-x),\ \frac{dz_4}{dx}(-x)\right]$$

In the particular case of the FLR Hall MHD dynamical system, it can be proved that Equations (2.51) and (2.87) are reversible in the sense presented by [2] under the transformation

$$\hat{x} \longrightarrow (-\hat{x})$$
$$[u_x(\hat{x}),\ u_y(\hat{x}),\ u_z(\hat{x}),\ b_y(\hat{x}),\ b_z(\hat{x})] \longrightarrow [u_x(-\hat{x}),\ -u_y(-\hat{x}),\ u_z(-\hat{x}),\ -b_y(-\hat{x}),\ b_z(-\hat{x})]$$

which it is going to be expressed in a more compact way with the operator J_1 and being $U(x)$ one solution of the system, following the notation in [5]

$$U(x) \longrightarrow J_1 U(x)$$

Five state variables have been included since a dynamical system with five dimensions have been built. But bear in mind that the invariant $H(\mathbf{u}, \mathbf{b}) = 0$ is implicit in (2.87), so that we can think of the FLR Hall MHD dynamical system as being 4D; there are no five degrees of freedom because one of the states is constrained by the invariant.

This reversibility property may be seen from other point of view. If U is a solution and the system is reversible when J_1 is applied, then $J_1 U$ is also a solution. Moreover if the solution U reaches $b_y = 0$ and $u_y = 0$ simultaneously, $J_1 U$ will also reach $b_y = 0$ and $u_y = 0$, so that both solution can be joined together forming a single trajectory in the state space. It is important to understand that this connection can only take place through the 2D surface in the 4D state space defined by $b_y = 0$ and $u_y = 0$ —which is called the *symmetric section*—, because these are the only points that may belong at the same time at U and $J_1 U$. Note that the upstream equilibrium is, in phase space, a point placed on the symmetric section.

To summarize, the FLR Hall MHD system is 4D and reversible. These two features are important and have a consequence on stability of the upstream equilibrium state and on the existence of symmetric solitary wave solutions. Solitary waves are orbits that connect with one equilibrium point for $x \to \pm\infty$. This type of solutions are called homoclinic orbits. Article [2] by A.R. Champneys compiles many interesting information and conclusions related to homoclinic orbits in reversible dynamical systems with an even number of dimensions. So that all the knowledge from [2] applies to the concerning case.

Stability of equilibrium points 4D dynamical systems

The study of the stability of equilibrium solutions in 4D is made in the same way than with any other system and has been already explained in Section 3.1.1. The

type of equilibrium in terms of stability is established looking at the layout of eigenvalues in the complex plane of the Jacobian matrix of the system.

In 2D systems equilibrium points are classified according to the eigenvalues of the Jacobian of the system in *centers*, *stable/unstable focus*, *saddles* and *stable/unstable nodes* depending on whether the two eigenvalues are imaginary conjugates, complex conjugates with negative/positive real part, negative and positive real or all of them negative/positive real, respectively.

In the case of the Hall MHD dynamical system —described in [1] or [14]— the possibilities get reduced due to the system being Hamiltonian. That is to say, the system has a Hamiltonian function[3] associated to it. Hamiltonian systems are conservative, which implies $\nabla \cdot \mathbf{f} = 0$. Therefore, trajectories cannot emerge or disappear at one point, they must be closed or go to infinity, which prevent any equilibrium point from being a node or a focus in 2D.

In 4D systems, the fact of having four eigenvalues results into many more possibilities. However, for the particular case of interest, a symmetric equilibrium, the eigenvalues are forced to be symmetric with respect to the imaginary axis in the complex plane —apart from the symmetry with respect to the real axis, which is obliged as long as the Jacobian is real. This can be intuitively reasoned once reversibility has been understood. As an example[4], if there exists one unstable eigendirection associated to a real eigenvalue λ at one side of the symmetric section, due to symmetry an stable eigendirection must exists symmetrically to the first one and associated to a real eigenvalue $-\lambda$.

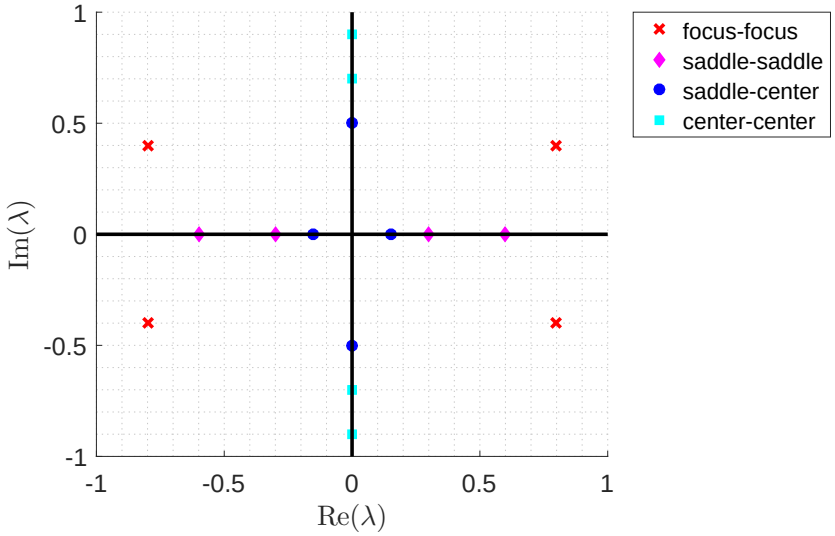

Figure 3.1: Casuistry of eigenvalues in the complex plane for 4D symmetric equilibrium

[3] A Hamiltonian function has not been found or proved to exists in the FLR Hall MHD case.

[4] For the example real eigenvalues have been chosen for simplicity, but the symmetry of eigenvalues applies also for complex ones.

Figure 3.1 reflects the possible position of the eigenvalues in the complex plane and the name assigned to each case. The convention used to name the type of equilibrium depending on the eigenvalues follows the names used in the 2D case. A pair of complex conjugates is referred to as *focus*, a pair of imaginary eigenvalues is referred to as *center* and a pair of negative-positive eigenvalues is a *saddle*. Due to symmetry it is not possible to have nodes —in this case this conclusion is not related to the Hamiltonian character of the systems.

3.2 Homoclinic orbits

Homoclinic orbits are solutions of a dynamical system that approaches to an equilibrium point as $x \to \pm\infty$. That is to say, the homoclinic orbit is a trajectory that departs from equilibrium point and returns to that same equilibrium. When the independent variable of the system is spatial, homoclinic orbits are usually called solitary waves. In addition, if the system is integrable, the term *soliton* is used. Solitary waves typically arise as solutions of nonlinear systems in partial differential equations —as it has been shown in Section 2.3.1.

In section 3.1.1 the concepts of stable and unstable manifolds were introduced. Attending to its definition, the reader may have realized that it an homoclinic orbit belongs to the stable manifold of the equilibrium point but also to the unstable one. Therefore this type of trajectories happen whenever the stable and unstable manifolds of the equilibrium point intersect. This is not the only conclusion one may extract from the definition of homoclinic orbit. The existence of both, stable and unstable manifold of the equilibrium is a necessary condition for the existence of this kind of orbits linked to that particular equilibrium. But this condition being satisfied does not guarantee the existence of homoclinic orbits. However, it is possible to know beforehand in which conditions it has no sense to look for solitary wave solutions

At this point the relation between homoclinic orbits and reversibility is to be introduced. The reversibility property of the concerning system is a great advantage when trying to find solitary wave solutions. In order to prove the existence of solitary waves in reversible system is not longer needed to find a solution coming from equilibrium at $x \to -\infty$ and returning to the same equilibrium at $x \to \infty$. The only requirement is to prove that a solution departing from the equilibrium intersects the symmetric section, because in this case it can be guaranteed that the solution will come back to the equilibrium symmetrically. That is to say, for an homoclinic orbit to exists it suffices to have an intersection between the stable or unstable manifold with the symmetric section, because in this case it is known that the orbit will return to the equilibrium following the other manifold.

One of the main tasks to be accomplished is to study the existence of solitary wave solutions in the parameters space —that is to say, for which values of $\boldsymbol{\mu}$ homoclinic orbits exist. As mentioned, the value of $\boldsymbol{\mu}$ may affect the dynamics of the system and, of course this may imply creation or destruction of homoclinic orbits. How this kind of solutions are organized in the parameter

space highly depends on the type of equilibrium —in terms of stability. Reference [2] condensates many information extracted from an extensive bibliography and analyzes this question for dynamical systems with similar properties as the FLR Hall MHD one. It studies the equilibrium of a general 4D system with parameters a and b —i.e. $\boldsymbol{\mu} = (a,\ b)$— and with characteristic equation

$$\lambda^4 - b\lambda^2 + a = 0 \tag{3.10}$$

with results into the following stability map[5] in parameter space:

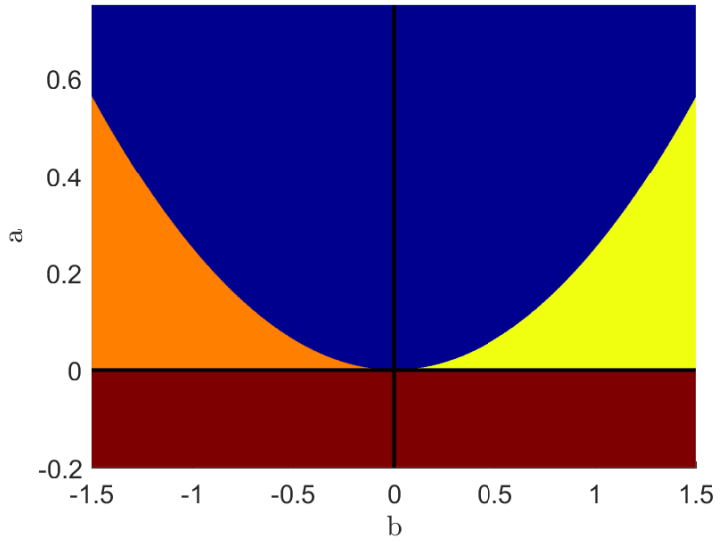

Figure 3.2: Stability map based on Fig.1 of [2]
Blue: focus-focus. Orange: center-center.
Yellow: saddle-saddle. Brown: saddle-center.

Let us summarize the main conclusions gathered in [2] regarding the existence and organization of solitary wave solutions in the parameter space presented in Figure 3.2 for each of the cases[6]:

1. *Center-center*: the eigenvalues are two pairs of pure imaginary conjugates. The equilibrium solution is critically stable. Therefore there do not exist neither stable nor unstable manifolds and as a consequence homoclinic orbits cannot happen.

2. *Saddle-saddle*: two eigenvalues are positive real while the other two are negative real. In this case, the two eigenvectors associated to the positive eigenvalues define the unstable manifold, while the other two define the stable one. Both manifolds are bi-dimensional.

   Homoclinic orbits exist in saddle-saddle conditions whenever the 2D manifolds intersect —or equivalently, when one of the manifolds intersect

[5]By stability map it is understood a plot like the one in Figure 3.2, classifying the stability type of the studied equilibrium as function of the parameters.

[6]Note that the different cases are named following [5] rather than [2] because it has been considered to be clearer.

the symmetric section, which is also bi-dimensional. The intersection of 2D entities in a 4D space may occur relatively easily, since it is equivalent to impose 4 constrains on a space with 4 degrees of freedom. The intersection will, in general, take place at localized points, although it is not guaranteed. One would expect to find homoclinic solutions for every point in the parameter space in saddle-saddle equilibrium.

The previous reasoning is not a rigorous proof, but a qualitative way of understanding the results that are mathematically demonstrated in [2]. According to [2], it can be mathematically proved that homoclinic orbits organize in a continuum of solutions in the parametric plane when the equilibrium is saddle-saddle. Solitary waves exist, in principle, for every combination of parameters in saddle saddle conditions. An equivalent way of expressing this idea is to say that homoclinic orbits have codimension zero in the parametric domain. The codimension can be defined as the number of parameters that have to be changed in order to move from one point in the parametric domain to an homoclinic solution, within areas corresponding to certain type of the equilibirum point. In the saddle-saddle case, since solitary waves arrange in a continuum of solutions, solutions are said to have codimension zero.

3. *Focus-focus*: In this case the four eigenvalues are complex conjugates —by pairs—, but two of them have positive real part while the other two have negative real part. Similarly to the saddle-saddle case, the stable and unstable manifolds exist and are bi-dimensional, so that a continuum of homoclinic orbit solutions is expected in the parameter domain. Additional considerations are proposed in [2] regarding the multiplicity of the solutions due to reversibility and the oscillations introduced by the imaginary part of the eigenvalues.

4. *Saddle-center*: two eigenvalues are imaginary while the other two are positive and negative real. In this case the stable and unstable manifolds are each of them 1D.

   The existence of solitary waves in saddle-center conditions requires, in general, the intersection of the 1D unstable and stable manifolds. The intersection of 1D objects in a 4D space is not easy to occur, since it requires that 6 constrains are satisfied in a space with 4 degrees of freedom. However, in reversible systems the existence of solitary waves is guaranteed as long as the stable or unstable manifold intersects the symmetric section, which is 2D in the case of 4D systems. The intersection of the 1D manifold with a 2D hypersurface in 4D is more easy to happen, since 5 constrains have to be satisfied. This non-rigorous explanation highlights that the reversibility property of the system facilitates the existence of solitary wave solutions, and, consequently, it has an effect on the organization of solutions in the parametric plane.

   Reference [2] mathematically proves that in saddle-center symmetric equilibrium, homoclinic orbits are organized in branches. That is to say,

in curves $a = a(b)$ in the case of Figure 3.2. Therefore, homoclinic solutions have codimension 1 in the parametric domain.

The discussion on existence of homoclinic orbits in the parameter domain depending on the stability of the equilibrium point is summarized in Table 3.1.

In the case of the FLR Hall MHD a characteristic polynomial with the shape of Equation (3.10) can be found for the upstream equilibrium. With a and b being function of C/v_A, $v_\perp/v_A$, $v_{se}/v_\perp$, a_p and θ. We want to analyze stability and solitary wave existence in the parametric space defined by Equation (3.3), rather than in terms of a and b —which lack of physical meaning. To do so stability maps will be built in the $C/v_A - \theta$, plane fixing the values of $v_\perp/v_A$ and v_{se}/v_A and a_p, while varying θ and C/v_A. This way of studying the stability of the upstream will results in maps with more complicated geometries than in Figure 3.2.

Case	Manifold dimension	Solutions arrangement	Codimension
Center-center	0	Non-existence	-
Saddle-saddle	2	Continuum	0
Focus-focus	2	Continuum	0
Saddle-center	1	Branches	1

Table 3.1: Existence of homoclinic orbits in symmetric equilibrium solutions to 4D dynamical systems.

Chapter 4

Solitons in the FLR Hall MHD model for solar wind

The previous chapters introduced concepts of plasma physics and dynamical systems that are going to be needed. This chapter is more practical and explains how all the previous theory has been used to solve the problem of the existence of solitary waves in the FLR Hall MHD for solar wind.

Before entering into the details of the algorithms, let us summarize the main conclusions or key points from previous chapters. In Chapter 2 conducting-fluid models for plasma were introduced. To be precise, collisionless plasmas can be modeled using doble adiabatic equations of state and the MHD equations are corrected by including the Hall term in the magnetic induction equation and Finite Larmor Radius corrections for pressure. After particularizing the FLR Hall MHD system of equations (2.39)-(2.41) for stationary one-dimensional traveling solutions and dealing with the singularity of the 1D FLR tensor $\underset{\sim}{\mathbf{A}}$, the system of Partial Differential Equations is reduced into the system of Ordinary Differential Equations

$$\frac{d\mathbf{u}}{d\hat{x}} = \frac{\hat{b}}{\delta}\mathbf{w} \tag{4.1}$$

$$\frac{d\mathbf{b}}{d\hat{x}} = -\mathbf{G} \tag{4.2}$$

whose vector of parameters is defined as $\boldsymbol{\mu} = (C/v_A,\ v_\perp/v_A,\ v_{se}/v_\perp,\ a_p,\ \theta)$. This dynamical system has an equilibrium point at the upstream state, i.e. $u_x = b_z = 1$ and $u_y = u_z = b_y = 0$. Due to the existence of an invariant in the system, it can be thought of as a 4D system. The most interesting property is reversibility —which was defined in 3.1. By analyzing the dimensions of the stable and unstable manifolds and using the existence of a symmetric section it was possible to anticipate the expected arrangements of homoclinic orbit solutions in the parametric space.

Although E. Mjølhus presents in [5] numerical solutions to the system and give some tips on the used numerical algorithms, it is not clear how this solutions have been found or how are solutions arranged in the parametric domain. Moreover,

although the results presented in [14] look like solitary waves, no rigorous proof of existence is given —the author himself states that his results do not have to be considered as a proof of existence of solitary waves in the FLR Hall MHD model. It seems that some solutions may be similar to solitary waves but a mathematical evidence must be found. In this project these kind of proofs are shown in saddle-center equilibrium conditions following the procedure of reference [15].

4.1 Methodology

This section contains the methodology and the basis of the main algorithms developed for solving the problem of existence of solitary waves in the parametric domain. The codes implementing the algorithms have been written and run using MATLAB.

4.1.1 Stability Map of the equilibrium solution

As highlighted in Section 3.2 the organization of solitary waves in the parameter space is highly influenced by the stability of the upstream state. The goal is to obtain plots similar to Figure 3.2 but substituting the axis by parameters with physical meaning. This is done for fixed values of $v_\perp/v_A$, $v_{se}/v_\perp$ and a_p, studying how the eigenvalues change varying θ and C/v_A —thus, our map is represented with axis C/v_A and θ and for every combination of $v_\perp/v_A$, $v_{se}/v_\perp$ and a_p a different plot is going to be obtained.

The Jacobian matrix associated to the dynamical system given by Equations (4.1) and (4.2) has to be evaluated at the equilibrium. The next step is to compute the eigenvalues to classify the equilibrium type. The calculation of the Jacobian matrix can be faced in two different ways:

1. Numerically. At some point in the overall process Equations (4.1) and (4.2) are going to be integrated to obtain numerical solutions, so that a MATLAB function has to be coded which receives as input the parameters and state variables values and delivers the right-hand side of Equations (4.1) and (4.2).

   On the other hand a very simple routine can be written that computes partial derivatives with centered finite differences and constructs the Jacobian matrix for given vector function and state. This routine can be used to obtain numerically the Jacobian of the right-hand-side function.

   Once the Jacobian has been computed, the routine *eig()* already incorporated in MATLAB libraries can be used to calculate the eigenvalues —and also the eigenvectors, which will be later needed.

2. Analytically. This is the approach followed in [5], which obtain the eigenvalues using Equation (2.54) rather than (4.1). Trying solutions

$$\begin{bmatrix}\mathbf{u}(x)\\ \mathbf{b}(x)\end{bmatrix} = \begin{bmatrix}\mathbf{u}_0\\ \mathbf{b}_0\end{bmatrix} + \begin{bmatrix}\mathbf{u}_1(x)\\ \mathbf{b}_1(x)\end{bmatrix} = \begin{bmatrix}\mathbf{u}_0\\ \mathbf{b}_0\end{bmatrix} + \mathbf{V}e^{\lambda\hat{x}}$$

around the equilibrium, with order 1 terms being small perturbations, the system is linearized. The resultant equation is

$$\left(\underset{\sim}{\mathbf{M}}^T + \lambda \underset{\sim}{\mathbf{N}}\right) \cdot \mathbf{V} = 0 \tag{4.3}$$

with

$$\underset{\sim}{\mathbf{M}} = \begin{bmatrix} (\partial \mathbf{F}/\partial \mathbf{u})_0 & (\partial \mathbf{G}/\partial \mathbf{u})_0 \\ (\partial \mathbf{F}/\partial \mathbf{b})_0 & (\partial \mathbf{G}/\partial \mathbf{b})_0 \end{bmatrix}$$

$$\underset{\sim}{\mathbf{N}} = \begin{bmatrix} \delta_0 \underset{\sim}{\mathbf{A}}_0 & 0 \\ 0 & \underset{\sim}{\mathbf{I}} \end{bmatrix}$$

in which $\underset{\sim}{\mathbf{A}}_0$ is the 1D FLR tensor evaluated at the equilibrium and $\underset{\sim}{\mathbf{I}}$ the identity matrix. The matrices of partial derivatives of $\mathbf{F}$ and $\mathbf{G}$ in $\underset{\sim}{\mathbf{M}}$ follow the definition of Jacobian typically used in fluid mechanics[1] —i.e. the transpose of (3.7). The linearization of a general function $\mathbf{f}(\mathbf{z})$ around $\mathbf{z}_0$ using this definition is $\mathbf{f}(\mathbf{z}_0 + \mathbf{z}_1) \approx \mathbf{f}(\mathbf{z}_0) + \mathbf{z}_1 \cdot (\partial \mathbf{f}/\partial \mathbf{z})_0 = \mathbf{f}(\mathbf{z}_0) + (\partial \mathbf{f}/\partial \mathbf{z})_0^T \cdot \mathbf{z}_1$. Looking at this linearization expression, the reason for $\underset{\sim}{\mathbf{M}}$ being transposed is clear —bear in mind that the matrix $\underset{\sim}{\mathbf{A}}$ multiplies $d\mathbf{u}/d\hat{x}$ on the left side. A difference with respect to [5] has been found, where the matrix $\underset{\sim}{\mathbf{M}}$ is not transposed in its equation (49).

The problem to be solved —i.e. Equation (4.3)— differs from the typical eigenvalue problem (3.8). MATLAB libraries include the routine *polyeig()* for this type of modified eigenvalue problems, so that values for λ and $\mathbf{V}$ —which play the role of eigenvalue and eigenvector— are obtained.

Both options are equally easy to implement into a code —having in mind that the derivatives of $\mathbf{F}$ have already been analytically derived for the computation of w_R in Equation (2.98) and the derivatives of $\mathbf{G}$ are easy to derive— and it has been checked that the same eigenvalues and eigenvectors are obtained from the two methods, as it should. More accurate solutions are expected from the analytical approach but this choice seems not to have a big influence on final results.

A 2D grid can be defined on the θ-C/v_A plane and for each point in this grid —with the other parameters fixes— eigenvalues can be computed and the equilibrium type classified according to them. Each type can be assigned to a number —e.g. number 1 for saddle-saddle equilibrium— and results stored in a matrix with the size of the grid. Plotting this matrix in the grid formed by θ and C/v_A results into maps similar to Figure 3.2. Of course, as the grid is made finer the

[1] The reason behind this choice is to follow the process in [5]

resolution of the map improves.

In [5] an example of this type of maps is shown, for certain value of the cited parameters. This will be referred to as the nominal case from now on, computed with $v_\perp/v_A = 0.4$, $v_{se}/v_\perp = 1$, $a_p = 1$. The following figure shows examples of equilibrium classification, indicating in each case the differences in the parameter values with respect the nominal one. The stability map in Figure 4.1(a) coincides with the one in [5].

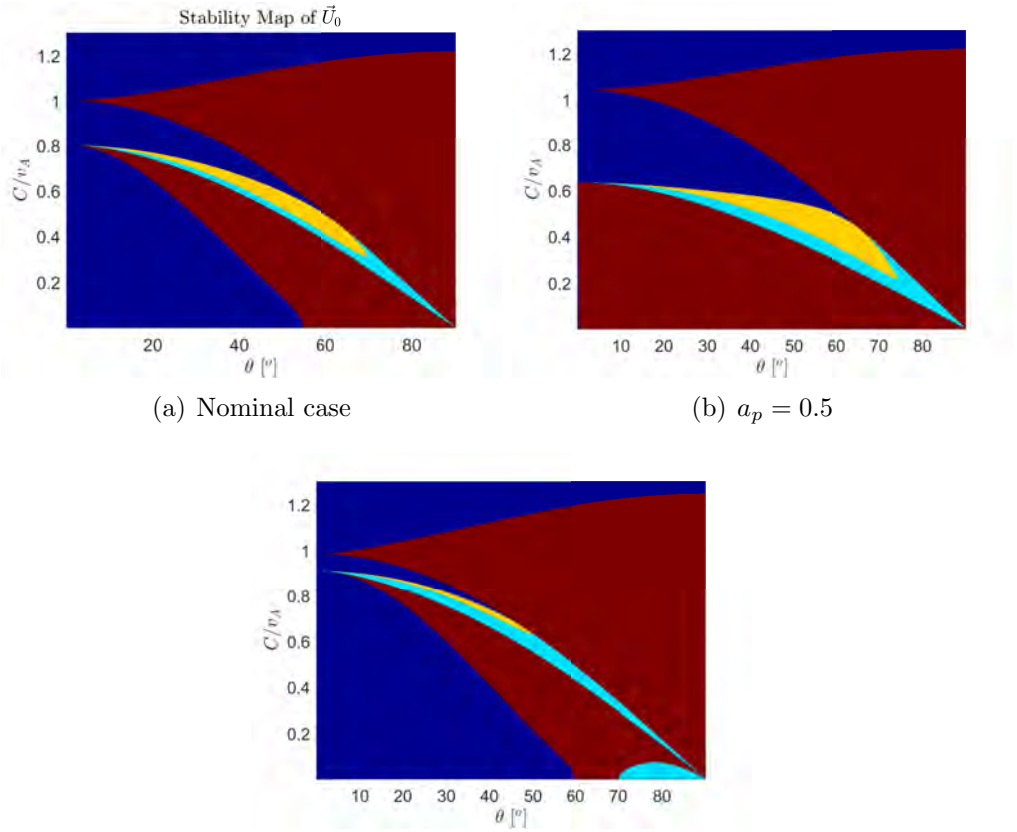

(a) Nominal case

(b) $a_p = 0.5$

(c) $a_p = 1.24$ and $v_{se}/v_\perp = 1.19$

Figure 4.1: Stability maps of the upstream state.
Brown: saddle-center. Yellow: focus-focus.
Cyan: saddle-saddle. Blue: center-center.

The stability of the equilibrium point is highly driven by the values of five critical velocities —normalized with v_A— as a function of θ. Three of them are phase velocities of the fast, Alfvén and slow wave modes associated to the MHD model without Hall or FLR dispersion. The other two are the sonic and the FLR velocities. Both of them are defined by E. Mjølhus in [5]. The FLR velocity is given by the values of $C/v_A(\theta)$ satisfying the equation $\Gamma_R(\mathbf{u}_0, \mathbf{b}_0) = 0$, provided that the other parameters have fixed values. The effects of these speeds on stability are already discussed in [5].

4.1.2 Solitary wave existence criteria

As already mentioned no rigorous criteria that allow to state that a solitary wave exists for certain value of the problem parameters is established in [5]. It is important to set the criteria for solitary wave existence, especially for solutions in the saddle-center parametric regions —but not only— where solutions are expected to be arranged in branches and not in a continuous way. In fact, the criteria for solitary wave existence has been already explained in Section 3.2 but is highlighted here from a more practical perspective.

Homoclinic orbits tend to equilibrium as $\hat{x} \to -\infty$ through the unstable manifold. In practice, this means that the integration of Equations (4.1) and (4.2) must be started at some point in the state space extremely close to the equilibrium following an unstable eigendirection. In saddle-center regions this means in the direction of the eigenvector associated to a positive real eigenvalue, while in saddle-saddle areas unstable eigendirections are all those lying on a 2D hyperplane defined by the two eigenvector associated to positive eigenvalues. In focus-focus equilibrium, the unstable manifold is also 2D, but in this case the two eigenvectors are complex conjugates and the unstable manifold is defined by rotating one of the complex eigenvectors in the complex plane and taking the real part. Essentially:

$$\text{Saddle-center:} \qquad (\mathbf{u}, \mathbf{b})_{\text{init}} = (\mathbf{u}_0, \mathbf{b}_0) + \varepsilon \mathbf{V}_u \tag{4.4}$$

$$\text{Saddle-saddle:} \qquad (\mathbf{u}, \mathbf{b})_{\text{init}} = (\mathbf{u}_0, \mathbf{b}_0) + \varepsilon \left(\cos\varphi \mathbf{V}_{u,1} + \sin\varphi \mathbf{V}_{u,2}\right) \tag{4.5}$$

$$\text{Focus-focus:} \qquad (\mathbf{u}, \mathbf{b})_{\text{init}} = (\mathbf{u}_0, \mathbf{b}_0) + \varepsilon \,\text{Re}\left(e^{i\varphi} \mathbf{V}_u\right) \tag{4.6}$$

where all eigenvectors are normalized, ε is how much the initial state separates from the upstream point and φ is a coefficient —ranging from 0 to 2π— that determines the direction in the unstable 2D hyperplane along which the initial point separates from equilibrium.

Beware that in the saddle-center case there are two possible directions $\mathbf{V}_u$ or $-\mathbf{V}_u$, and both have to be explored when searching for solitary waves —in the code the sign of ε is modified, not $\mathbf{V}_u$ itself. This two possibilities are related to the existence of bright and dark solitary waves —according to [5]—, classified according to $b^2 > 1$ and $b^2 < 1$ respectively. The existence intervals of these two types of solutions in the Hall-MHD model are studied by E. Mjølhus in [1].

By starting the integration at the suitable initial point the solution satisfy one of the conditions in the definition of homoclinic orbit. The other condition is that the solution should return to the equilibrium point as $\hat{x} \to \infty$, which has been proved to be guaranteed as long as the solution intersects the symmetric section —defined by $u_y = 0$ and $b_y = 0$. That is to say, if during integration the values of u_y and b_y are detected to be zero simultaneously, it can be stated that a solitary wave solution exist.

The numerical algorithm trying to find solitary wave solutions consists in starting the integration at some point close to equilibrium and in the unstable manifold, and stop the integration whenever there is a change of sign of b_y. At the $\hat{x}$ in which the simulation was stopped the value of b_y is expected to be very close to zero —as long as the integrator has been properly configured— and u_y has certain value which is not necessarily close to zero. This method may be in principle used in saddle-center, saddle-saddle and focus-focus regions, but with differences:

- Saddle-center. This procedure applied on saddle-center regions delivers a final value of u_y for each combination of θ and C/v_A. To be precise, in the most general case two values of u_y are possible, one for orbits started along $\mathbf{V}_u$ and other for $-\mathbf{V}_u$. But when going to real computations it has been noticed that the most common case is that only one trajectory crosses $b_y = 0$, while the other one intersects the singularity hypersurface defined by $\Gamma_R(\mathbf{u}, \mathbf{b}) = 0$ —the practical issues regarding this singularity will be discussed later in this chapter.

  Although the designed algorithms did not initially take into account the possibility of two u_y values for a single C/v_A, in order to be rigorous it should be considered. To do so, for fixed θ, two curves $u_y = u_y(C/v_A)$ should be computed. One for $b(\hat{x})^2 > 1$ —bright— and other for $b(\hat{x})^2 < 1$ —dark. A linearization of $b^2 = b_y^2 + b_z^2$ around the equilibrium results into $b_1 = b_{1z}$ —terms of order one are perturbations of the equilibrium. Therefore, eigendirections with positive component in b_z are presumably linked to the existence of bright solitary waves, while negative b_z indicates the possibility of a dark solitary wave —according to [5], but an implicit assumption is that if $b_1(\hat{x}_0) > 0$ ($b_1(\hat{x}_0) < 0$) initially, $b(\hat{x}) > 1$ ($b(\hat{x}) < 1$) for every $\hat{x}$, and this has not been proved. In the most general case, there should exist two curves $u_y = u_y(C/v_A)$: one associated to $b_{1z}(\hat{x}_0) > 0$ and other to $b_{1z}(\hat{x}_0) > 0$.

  One could calculate the final value of u_y for certain C/v_A range at fixed θ. If a change of sign in u_y happens between two consecutive values of C/v_A, it is known that $u_y = 0$ within that interval of C/v_A. That is to say, an angle θ and an interval of C/v_A can be determined[2] in which at some point in the solution b_y is extremely close to zero and u_y crosses $u_y = 0$. Therefore for that angle and within that velocity range one solution intersects the symmetric section and it can be stated that a solitary wave solution exists.

  The interval of C/v_A containing the solitary wave solution can be made narrower using a bisection method that tries to find the zeros of the $u_y(C/v_A)$ function. To do so, the bisection code must be provided with a routine that delivers the value of u_y —when integration is stopped at b_y sign changes— as function of C/v_A and two initial points inside which a change of sign in $u_y(C/v_A)$ takes place.

- Saddle-saddle. According to reference [2] and the conclusions in the previous chapter, it may be expected to have solitary wave solutions at every pair of

[2]Of course, one could fix C/v_A and vary θ.

θ and C/v_A. This does not imply that a solution exists for every unstable direction along which the equilibrium is perturbed —i.e. not for every value of φ in Equation (4.5).

Therefore, the method of stopping the integration when b_y changes its sign will result in a value of u_y for every φ —in this case θ and C/v_A are both fixed. One could try to find intervals of φ inside which a change of sign in $u_y(\varphi)$ happens. The procedure would be exactly equal to what explained for C/v_A in the saddle-center case.

This numerical algorithm for finding solutions in saddle-saddle regions is already suggested in [5], but leading to non-promising results according to the author. The main efforts have been put on solving the saddle-center problem. However, it may be interesting to continue the work of this thesis exploring the saddle-saddle region and trying to implement this presumably failed method. Since the problem of finding intervals of φ is mathematically equivalent to the problem of C/v_A for the saddle-center case, we could take advantage of the knowledge and expertise acquired from the work in the saddle-center region. Maybe we could understand why this algorithm is failing or adapt it to work properly. The focus-focus algorithm would be very similar to what explained for the saddle-saddle case. However, some concerns on multiplicity of the solitary wave solutions should be taken into account.

Finally, just make mention that the *ode45()* integrator —included in MATLAB— has been used for solving Equations (4.1) and (4.2) given an initial point to start the integration. The integrator options include the possibility of defining events. Whenever an event happens the integration can be stopped. For the algorithm finding intersections with the symmetric section the event $b_y = 0$ is established, although not the only one —see next section. Next sections are particularized for the saddle-center case.

4.1.3 The singularity hypersurface

Apart from the symmetric section there is another important hypersurface, the one defined by the equation $\Gamma_R(\mathbf{u}, \mathbf{b}) = 0$. At these points the variable w_R becomes infinite and this affects the derivatives. Of course, this is translated in extremely high values of the derivatives when integrating numerically and leads to numerical problems. For example, the computations may get stuck because it cannot move forward in x due to the singularity. The intersection of the orbit with this hypersurface has been found to be a very common event according to experience on the saddle-center regions. Moreover, it is mentioned in [5] as one of the reasons of the failure of the saddle-saddle solitary wave finding algorithm.

An analysis on dimensions of manifolds and surfaces, similar to the one in Section 3.2 for intersections of manifolds, may shed some light on this matter —let us thought of the state space as 4D, in order to follow previous reasonings. The singularity hypersurface in the 4D state space is defined by the intersection of $\Gamma_R(\mathbf{u}, \mathbf{b}) = 0$ with the invariant $H(\mathbf{u}, \mathbf{b}) = 0$ —this is a 3D object. Since the

unstable manifold is 1D —3 constrains to a 4D state space— the intersection with the singularity surface implies 4 constrains to a 4D space. Moreover, the integration is stopped at $b_y = 0$. In geometrical terms, when an intersection with the 3D surface defined by $b_y = 0$ takes place. Therefore, trajectories started along the 1D unstable manifold crossing $b_y = 0$ and those encountering the singularity are expected to be found in the same amount.

The encounter with the singularity surface must be taken into account in the algorithms that involve integration of Equations (4.1) and (4.2). This can be faced by defining a new event that is passed to the integrator. This event should monitor the values of the state variable derivatives or Γ_R and stop the integration in case of derivatives being very large or Γ_R approaching zero.

It has been found very useful to plot a new kind of map —also with axes θ and C/v_A— in which points in the parameter space —all parameters fixed except θ and C/v_A— are classified according to:

1. The trajectories in state space, started along any of the two possible unstable directions, intersect the singularity hypersurface. It has no sense trying to find solitary wave solutions in these locations of the parameter space. Let us call them *singular points*. Due to the way the curves $u_y = u_y(C/v_A)$ have been defined, the values of C/v_A for given θ belonging to this category form non-existence intervals of these curves.

2. One of the trajectories intersects the singularity hypersurface but the other crosses $b_y = 0$. Solitary wave solutions are possible at these points, starting along one of the directions. This type of points are associated to a single value of u_y for $b_y = 0$. Since only one of the two possible unstable directions hits the $b_y = 0$ hypersurface. But two subtypes of points can be defined according to the sign of the perturbation along b_z:

   (a) $b_{1z}(\hat{x}_0) > 0$. This possibility is linked, in principle, to bright solitary waves.

   (b) $b_{1z}(\hat{x}_0) < 0$. Related, presumably. to the existence of dark solitary waves.

3. The two trajectories intersect the hypersurface defined by $b_y = 0$. Solitary wave solutions are possible starting the integration in any of the two possible directions. In this case each value of C/v_A is associated to two possible values of u_y for $b_y = 0$.

Le us call this type of plots *singularity maps*. Computing these plots with very good resolution is very demanding in terms of numerics. One should defined a grid on C/v_A and θ, and carry out two integrations at each of the points in this grid —one for each unstable direction. Moreover, as a trajectory approaches the singularity, the derivatives start growing and growing. If this is the case the numerical integration gets slower. Hopefully, the integration will not get stuck, since the values of the derivatives are being monitored and integration stopped if they

become too large.

During this project all points in saddle-center parametric regions have been found to belong to one of these three categories. In fact, points of type 3 are very scarce. Results on these maps show that the vast majority of the points in saddle-center regions belong to types 1 and 2 —at least for the combinations of parameters considered. In fact, algorithms computing $u_y = u_y(C/v_A)$ curves and branches of solutions have been constructed and executed by trying to compute trajectories in both unstable directions —that may may involve two numerical integrations— and taking the result reaching $b_y = 0$ —if any—, which is only one of the trajectories in most of the cases —the algorithms try with one direction, and in the case of reaching the singularity the second direction is tested.

In Section 4.1.2 it has been explained that these algorithms should be applied for two cases: $b_{1z}(\hat{x}_0) > 0$ and $b_{1z}(\hat{x}_0) < 0$. A map classifying the points in the parametric domain according to the recently introduced criteria can be used to know in which regions each of them take place —or maybe the two at the same time if the point is type 3. Since the maps reveal large regions of type 2(a) and 2(b) —separately—, the branch computation algorithms could have been limited to trajectories starting along directions with negative or positive perturbation on b_z —depending on the considered case— on the corresponding parametric regions, and then repeat computations for the opposite case. This would have significantly reduced the execution time. Unfortunately, this is a recent find and results were computed without implementing this useful feature —to be strongly highlighted that this is an improvement concerning only computational cost, and results shown in this thesis are correct. However, the algorithms have been modified for its posterior use in future works.

When integrating the dynamical system, there are some numerical settings that must be configured: the tolerances of the integrator, the distance from the equilibrium at which computations are started (ε) and the threshold value of the derivatives —above which the trajectory is assumed to have intersected the singularity hypersurface. Have in mind that speeding-up the computations is prioritized against accuracy in the case of singularity maps. The objective here is not to obtain accurate numbers but to obtain some maps that will help in subsequent tasks. The following numerical settings have been configured in order to carry out the computations in this section:

- $\varepsilon = 10^{-3}$.
- Maximum threshold value of derivatives: 1000.
- Absolute tolerance of the *ode45()* method: 10^{-6}.
- Relative tolerance of the *ode45()* method: 10^{-6}.

Of course, the value of ε must be, in any case, greater than the absolute tolerance of the integrator. Remember that one of the events leading to stopping the integration is $b_y = 0$, that is identified by a change of sign in $b_y(\hat{x})$. On the other

hand, variation of the state variables with respect the equilibrium —in absolute value— below the absolute tolerance cannot be trusted, because the numerical error is of the same order as the variations. If ε is smaller than the absolute integration tolerance, the evolution of b_y at the very first beginning of the integration may present erratic sing changes due to the numerical error, that will raise the event and stop the integration.

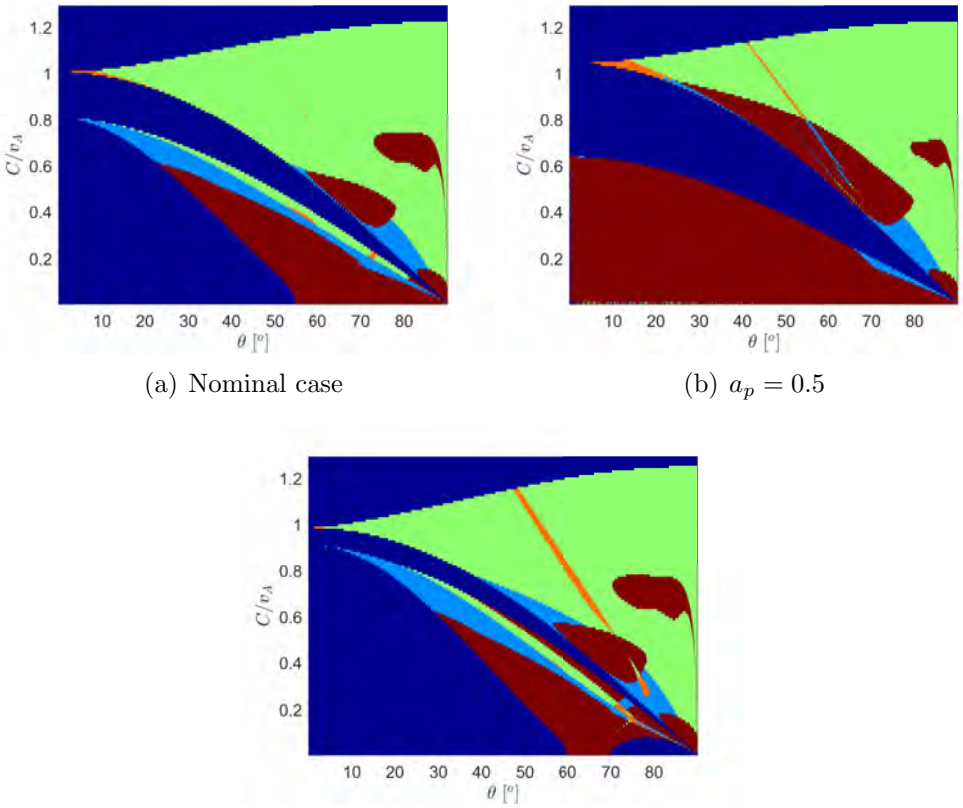

(a) Nominal case

(b) $a_p = 0.5$

(c) $a_p = 1.24$ and $v_{se}/v_\perp = 1.19$

Figure 4.2: Singularity maps
Dark blue: No saddle-center. Brown: Type 1. Blue: Type 2(a). Green: Type 2(b). Orange: Type 3.

Figure 4.2 show examples of singularity maps, for the same combinations of parameters than in Figure 4.1. Points in the parameter domain, whose both possible trajectories intersect $b_y = 0$ —i.e. type 3— are extremely scarce. Most of the points, in every example, have one trajectory crashing with the singularity surface and the other one with $b_y = 0$ —i.e. type 2. Furthermore, from this set of points, the majority starts with negative initial perturbation on b_z —i.e. type 2(b). It is known that no solitary wave solutions are going to be found in type-1 areas

4.1.4 Branches of solutions in saddle-center regions

In the Section 4.1.2 a rigorous criteria for determining existence of solitary waves has been proposed and one possible method has been described for searching solitary wave solutions with all parameters fixed —except for C/v_A— within certain interval of wave velocities C/v_A.

It could be thought that in order to calculate complete branches one could compute the curve $u_y(C/v_A)$ —for values of C/v_A comprised between the borders of the saddle-center region at one particular θ— at many values of θ —ranging from 0^o to 90^o—, and then looking for changes of sign. If points in the parameter space at which solitary waves have been found are represented in the θ-C/v_A plane, one would expect to see branches.

Branches have not, in general, simple geometries. Therefore, in order to properly capture and visualize branches in the parametric domain in this way, the spacing of θ values should be very small. As a consequence, the curve $u_y(C/v_A)$ has to be computed for a lot of values of θ. Beware that each point in $u_y(C/v_A)$ involves at least one integration of Equations (4.1) and (4.2). Moreover, when a sign of change in $u_y(C/v_A)$ is detected, the interval of C/v_A is to be reduced with the bisection method —which involves several integrations depending on the tolerance setting. This paragraph is indented to transmit the idea that a branch computation algorithm designed in this way is simple but involves a considerable amount of computational time to deliver good results. However, this approach can be used to make a first rough scan of the saddle-center regions —without bisection method— to visualize the areas in which it has sense to search solitary wave solutions.

An alternative algorithm is proposed. It may be advisable to take a look at Figure 4.3 at the same time the explanation is read. Starting from one localized solution in the parametric domain at θ_0 and within a tiny range[3] of C/v_A —the width of the interval comes determined by the bisection method tolerance—, the algorithm tries to find another solution, close to the previous one, located at $\theta_0+\Delta\theta$ —in this way, a new solution belonging to the same branch is expected to be found. To do so, the interval of C/v_A of the first solution is kept in the new value of θ and the sign of u_y is checked at the ends, having two possibilities:

1. The signs of u_y at the ends of the C/v_A interval are still opposite. Meaning that a solution exist —belonging, most probably, to the same branch— at $\theta_0 + \Delta\theta$ and within the same C/v_A interval than the first solution, and also with the required tolerance. This scenario is not probable, specially for small tolerance of the bisection. Typically, computations are being made for this project with a tolerance of 10^{-9}.

2. The signs of u_y at the ends of the C/v_A interval are equal. Meaning there is no solitary wave at $\theta_0 + \Delta\theta$ and within the same C/v_A interval

[3]Beware that this range is defined by the values at the ends. One of the ends corresponds to a positive u_y and the other to a negative u_y.

than the solution at θ_0. In this case the branch has not been caught at $\theta_0 + \Delta\theta$, so far. But making the explored interval progressively wider —if originally the interval is $\left[(C/v_A)_-, (C/v_A)_+\right]$, it can be extended to $\left[(C/v_A)_- - n\Delta(C/v_A), (C/v_A)_+ + n\Delta(C/v_A)\right]$ with $n \in \mathbb{N}$— and checking the signs of u_y at the ends, at some moment the signs of u_y are expected to be opposite. In this case a new solution has been found inside the broadened C/v_A interval, which is expected to belong to the same branch of solutions. The interval is narrowed again with the bisection method.

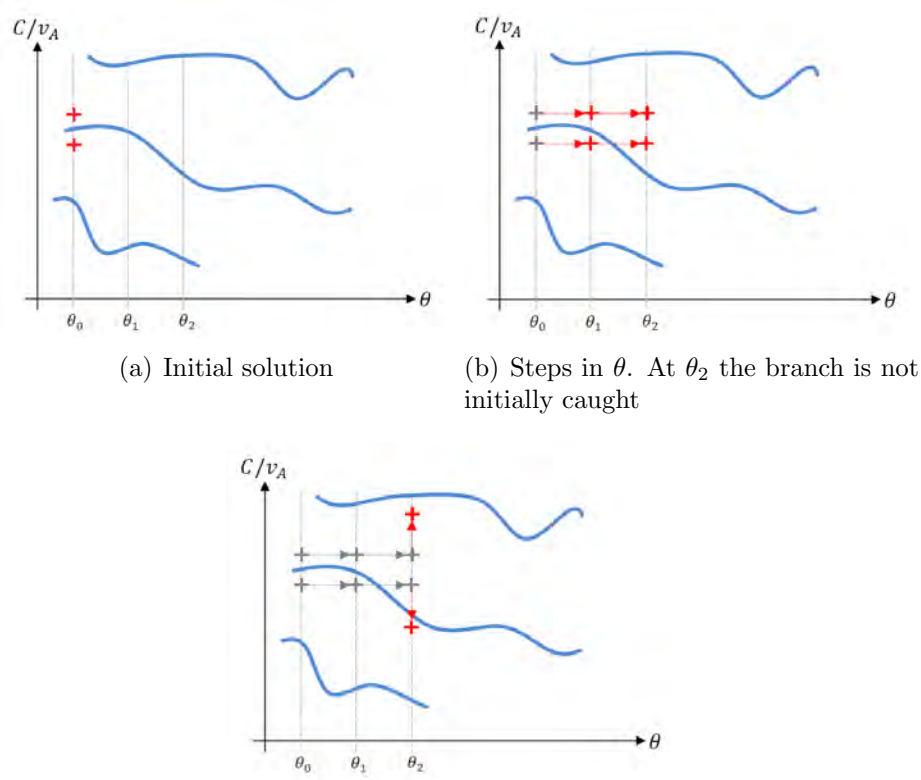

(a) Initial solution

(b) Steps in θ. At θ_2 the branch is not initially caught

(c) Broaden the C/v_A interval

Figure 4.3: Original branch computation algorithm.
Branches —in blue— are painted for clarifying purposes. They are not seen but have to be computed.

This process is to be repeated in subsequent values of θ in order to compute the solutions of one branch. In each new step in θ_j the interval of C/v_A containing one solution for θ_{j-1} —with $j \in \mathbb{N}$ and standing for an index that counts the points in the branch, starting from $j = 0$ for the initial point— is taken as the starting interval in which solutions are checked.

The success of this method highly depends on the selection of $\Delta\theta$ and $\Delta(C/v_A)$ as well as on the geometry of the branches. If $C/v_A(\theta)$ is the curve representing the branch in the θ-C/v_A parametric plane, the method is very likely to fail —being *failure* understood as converging to other branch— at points with large $d(C/v_A)/d\theta$ —despite a good choice for $\Delta\theta$ and $\Delta(C/v_A)$. This is because when

advancing in θ, it is done along lines $C/v_A(\theta) = \text{const.}$, so that the initial interval explored will significantly separate from the concerning branch if $d\left(C/v_A\right)/d\theta$ is big. In order to mitigate the effect of the slope of the branch curve, a modification has been made on the previous algorithm. When the code goes forward to θ_j, instead of taking $[(C/v_A)_-^{j-1}, (C/v_A)_+^{j-1}]$ as the initial interval in which solutions are searched, the starting interval at j is defined according to

$$(C/v_A)_{+,-}^{j} = (C/v_A)_{+,-}^{j-1} + m_{+,-}^{j-1}\Delta\theta_j \tag{4.7}$$

in which subindex j has been also added to $\Delta\theta$ because, in some circumstances, it may be convenient to use a variable step —note that $\Delta\theta_j$ is considered the step between $j-1$ and j. On the other hand, m_j is an estimation of the slope of the curve at point j, using points j and $j-1$ —this is *backwards finite differences* formula, i.e.

$$m_{+,-}^{j-1} = \frac{(C/v_A)_{+,-}^{j-1} - (C/v_A)_{+,-}^{j-2}}{\Delta\theta_{j-1}} \tag{4.8}$$

In this way whenever going forward in θ the curve is being somehow followed by making an estimation of its local slope and defining the initial interval at this new θ value accordingly. Of course Equation (4.8) requires of $j > 1$. The initial velocity interval at $j = 1$ is taken directly from the interval containing the solitary wave solution at $j = 0$. The effect of modifying the branch computation algorithm in this way can be schematically seen on Figure 4.4.

This algorithm is still not perfect and the delivered result may, of course, jump from one branch to another. However, experience has revealed that with the proper selection of $\Delta\theta$ and $\Delta\left(C/v_A\right)$ results are incredibly better than with the original method. In fact, once this numerical method has been configured, jumps to other branches are not common at all.

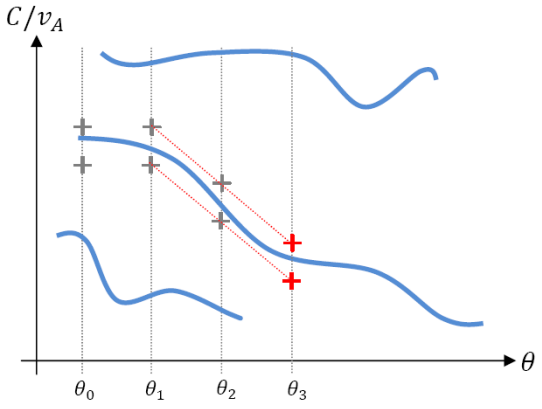

Figure 4.4: Update on the original algorithm.
Intended to mitigate the effect of branch geometry.

The most typical failure case happens whenever the branch turns around. That is to say, the code advances to θ_j but the branch under concern has no points at

this θ_j because it has turned around at some θ value between θ_{j-1} and θ_j. In this case the method is not able to converge to the right branch because there are no solutions of that branch on the considered θ —see Figure 4.5. It will, for sure, jump to another branch. The code could keep improving implementing an an arc-length continuation algorithm. This type of methods parametrize the branch curve using the arc-length coordinate in such a way that the solver moves in the parametric plane following the branch. The use of an arc-length continuation algorithm can be used to compute branches with any shape..

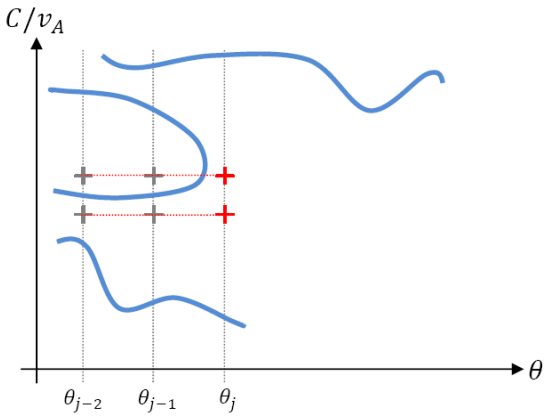

Figure 4.5: Branch turning around.

However this is a major change in the algorithm, and can be avoided by introducing minor modifications. Moreover there are other concerns, such as the intersection with the singularity hypersurface —to be precise, points of type 1 in Section 4.1.3— and leaving the saddle-center region. All this considerations have been taken into account in the following manner:

- Turn-around. This problem is faced by monitoring the values of the slope estimation given by Equation (4.8). A sudden change in the value of m —either the one with subindex '+' or '−'— is assumed to be an indication of a jump between branches. The threshold value of $\Delta m_j = m_j - m_{j-1}$ over which a *sudden change* is considered has been configured based on experience. If Δm_j is greater than a set value, the method is stopped and branch points previously computed are given as output.

  Note that, by doing so, the algorithm is only able to compute branches up to the θ value in which the turn-around takes place. However, this kind of branches can be understood as two individual branches connecting at the turn-around point. And both of them can be calculated with the current algorithm.

- Intersection with the singularity surface. It is possible that, when computing solutions along one branch, a region is entered in which there are points of type 1. In this case, any of the unstable directions lead to derivatives tending to infinite and the hypersurface $b_y = 0$ is not intersected. Remind that the curves $u_y(C/v_A)$ include only points whose trajectories have intersected

$b_y = 0$. So that singular points define non-existence intervals in curves $u_y(C/v_A)$, which may lead to complications if not considered.

If at least one of the ends of the C/v_A intervals —initial or when the interval is made wider— at certain θ corresponds to a singular point, the method is stopped. The branch computation is finished an the output is delivered.

- Leaving the saddle-center region. It is very convenient to have the borders of the regions to be explored computed and stored in a file. The program is able to load the border data and stop the process whenever an end of the considered C/v_A intervals is detected to lie out the region. Of course, another way of facing this problem is by means of checking the eigenvalues of the Jacobian.

To summarize, the final algorithm receives as inputs an array of θ values with the selected $\Delta\theta$. Also an array of C/v_A values, in which solitary wave solutions are searched taking also the initial θ. Changes of sign in $u_y = u_y(C/v_A)$ are detected and the C/v_A intervals containing them are saved. For every detected solution —i.e. a change of sign in u_y— the interval of C/v_A containing the solution is narrowed by means of a bisection method. Then, the code starts looking for solitary wave solutions at the next value of θ and within the final C/v_A interval of $j = 0$. If no solution is found within that initial interval —remember that there is a solution whenever the signs of u_y are opposite at the end of the interval— then it is made wider and wider until a solution is detected. The interval of velocities is narrowed again and the process is repeated for subsequent values of θ but using now Equation (4.7) and (4.8) to select the initial interval.

In order to speed up the computations, MATLAB parallel processing capabilities are used. With the *parfor* loop four iterations can be performed on parallel, as long as loop iterations do not depend on each other. Parallel computing has been implemented in such a way that as many branches as processor cores can be computed at the same time —four, in the case of the computer used to make the calculations.

Just a final comment on the types 2 and 3 introduced in Section 4.1.3. In this section it is also written that in order to compute the results in this thesis the fact of having the two subtypes 2(a) and 2(b) was not taken into account. Although it will be later remarked when explaining the results, the algorithm seems to work perfectly in the case of transitions from zones 2(a) to 2(b), and viceversa. Performing separate computations for regions 2(a) and 2(b) is, however, a good improvement, since the performance of the code is expected to increase significantly and numerical problems in type-3 regions are avoided —note that type 3 is the superposition of regions 2(a) and 2(b).

4.1.5 Time evolution of solitary wave solutions

As mentioned in Section 2.3.2, once a solitary wave has been proved to exist and the evolution of the state variables computed, it can be used as initial condition to solve the one-dimensional unsteady system of partial differential equations. If

the solitary wave is stable, the structure should persist in time without deforming.

The strategy is to discretize the spatial derivatives, so that the system of partial differential equations is converted into a system of ordinary differential equations —with derivatives in time. The dimension of the resultant system will be equal to the number of points in the x-grid in which the solution is being computed times the number of state variables.

There are several methods that can be used for the discretization, e.g. finite differences, finite element or spectral methods. Spectral methods are global, in the sense that they approximate the values of the derivatives of certain function by taking into account every single value of the function in the grid. The result is an incredibly good accuracy, as long as the function is smooth.

Notice that the value of the function —of which the derivatives are to be computed— is only known at the grid points. To approximate the derivatives, an interpolating continuous function that adjusts to the discrete values is found. There are two cases:

1. Periodic problem. In this case the interpolating function is a Fourier series. The grid should be uniform and the number of points must be a power of 2.

2. Non-periodic problem. In this case the interpolating function may be a polynomial. The grid now is not uniform. Non-periodic functions with polynomial interpolation provide better results on grids following especial spacing. One possibility is to use *Chebyshev points*.

The initial shape of the solution is given by the solitary wave solution. This solution should depart from and return to the equilibrium at the extreme values of $\hat{x}$. That is to say, the value of the functions whose derivatives are to be approximated —i.e. the state variables as a function of $\hat{x}$— should be approximately equal at the initial and final points. Although the problem is not periodic, just for numerical purposes it can be treated as periodic. Therefore, Fourier spectral methods are used to compute the spatial derivatives. By making this decision, periodic boundary conditions are being implicitly imposed on the solution.

The numerical algorithm is described now. The evolution of the state variables along $\hat{x}$ is known at the initial time instant. With these data, the initial $\hat{x}$ partial derivatives of the state variables can be computed at the grid points. To do so the Fast Fourier Transform (FFT) of the states is computed —MATLAB function *fft()*—, the transforms are multiplied by ik —this is the derivative operator in the Fourier space, being k the wavenumber— and the inverse Fast Fourier Transform provides the values of the derivatives at the grid points. Then, the time derivatives at each grid point can be computed using Equations (2.99)-(2.101). Other numerical method can use the time derivatives to approximate the value of the state variables in the next time instant. The process is to be repeated up to the end of the defined time span.

Here, the important information coming from the dispersion relations is to be highlighted. The numerical algorithm to calculate the time evolution of the solitary wave uses Fourier transforms. Basically, the state variable space evolution is being decomposed in oscillatory functions associated to certain wave number. The analysis of small amplitude solutions leads to mathematical relations between the wavenumber and the wave frequency —i.e. dispersion relations. It has already been explained that there may be wavenumbers linked to unstable solutions that will grow in time. An initial solitary wave solution with large energy at unstable wavenumbers —what can be known by visualizing the Fast Fourier Transform of the states— may show unstable behavior. Beware that the instability was predicted using linear theory, so that it is only valid at the tails of the solitary wave, where the value of the state variables is very close to the upstream value. The absence of linear instability does not guarantee that the solitary wave is stable.

This brief introduction about spectral methods is given so that the reader can understand the applicability of dispersion relations in this project. Gonzalo Sánchez-Arriaga and the author are currently collaborating with Drs. Thierry Passot and Dimitri Laveder from Observatoire de la Côte d'Azur on stability of solitary waves in the FLR Hall MHD model, but it is not the main subject of this thesis.

4.2 Results

In this section of the chapter, the results obtained by following the algorithms and reasonings exposed in Section 4.1 are going to be displayed and commented. Results will be restricted to the nominal case. The concerning stability map is shown in Figure 4.1(a) and the singularity map in Figure 4.2(a). There are two saddle-center separated areas, which will be referenced as the upper and the lower saddle-center regions.

4.2.1 Solitary wave existence on u_y vs. C/v_A curves

The existence criteria was already exposed in Section 4.1.2. Remind that the u_y vs. C/v_A curves display the value of u_y at the intersection with the subset $b_y = 0$. In the case that the two possible trajectories intersect the singularity surface, a non-existence interval in $u_y = u_y(C/v_A)$ happens. On the other hand, if both trajectories intersect $b_y = 0$, two values or u_y are possible for that value of C/v_A. This is not common at all, from the results on Figure 4.2.

A parametric analysis on ε is going to be made. The lower ε, the closer is the starting point to the unstable manifold of the equilibrium —being ε always greater than the absolute tolerance of the integrator. The eigenvector associated to unstable eigenvalues is only a linear approximation of the global unstable manifold in the vicinity of the equilibrium point. For that reason, a small ε is expected to provide more accurate solitary wave results —in the case such solution exists. E. Mjølhus uses $\varepsilon = 10^{-3}$ to compute the results in [5]. The analysis proposed here will show $u_y = u_y(C/v_A)$ curves, starting with $\varepsilon = 10^{-3}$ and reducing it progressively up to

$\varepsilon = 10^{-10}$. This is coherent with the absolute tolerance for the integration, set to 10^{-11} in this case —the same for the relative tolerance. For sufficiently small ε, this curves should be independent of ε as it is further decreased. Otherwise the solution cannot be considered to be valid. The maximum derivative threshold value is again 1000. In order to show the effect of varying ε to the reader, the curve $u_y = u_y(C/v_A)$ has been computed at $\theta = 50^o$, for the complete range of C/v_A of the upper saddle-center region. Points are spaced 0.0001 in C/v_A axis.

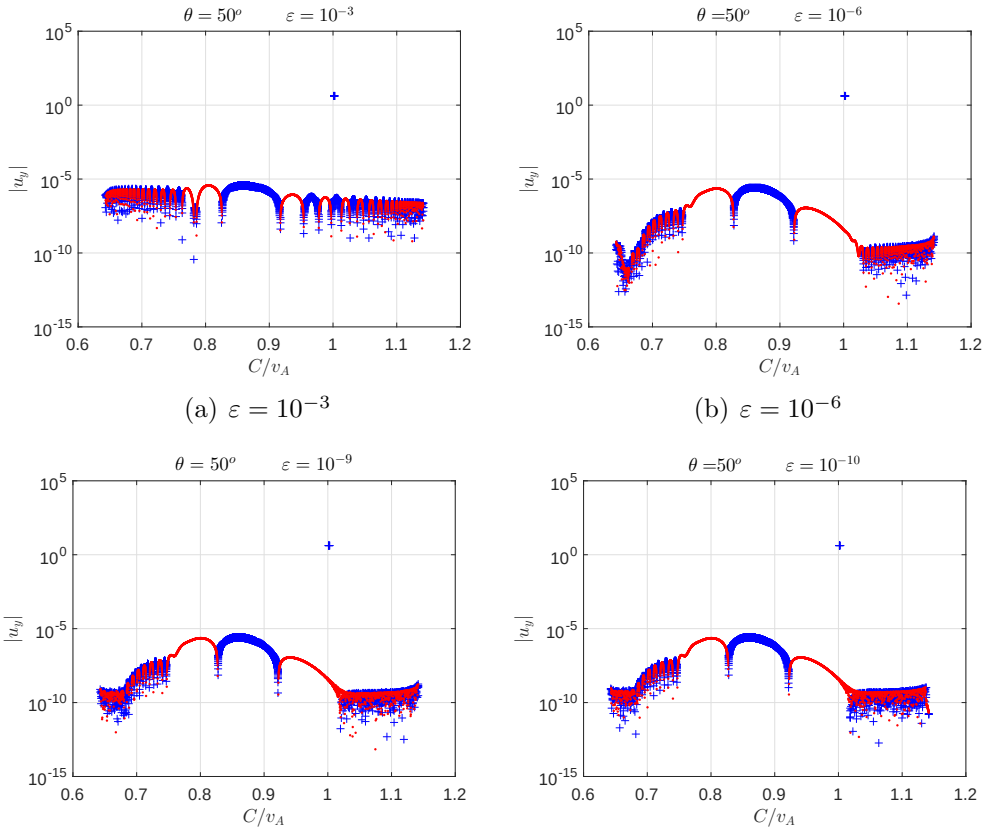

(a) $\varepsilon = 10^{-3}$ (b) $\varepsilon = 10^{-6}$

(c) $\varepsilon = 10^{-9}$ (d) $\varepsilon = 10^{-10}$

Figure 4.6: $u_y = u_y(C/v_A)$ for the upper saddle-center region at $\theta = 50^o$. Blue crosses: $u_y > 0$. Red dots: $u_y < 0$.

Figure 4.6 shows the results of u_y as a function of C/v_A, for integration stopped at $b_y = 0$, for several values of ε. For the vertical axis, logarithmic scale is being used. Anytime the sign of u_y changes, the solitary wave existence criteria defined in this thesis is satisfied. Solitary wave solutions exist at $\theta = 50^o$ and within the ranges of C/v_A containing changes of sign in $u_y = u_y(C/v_A)$. However, as ε is decreased the results, at the extremes of the considered C/v_A interval, become a non ordered sequence of points. The curve is no longer smooth and continuous and points have a random character —see Figure 4.7 in order to see a detail of a velocity interval dominated by numerical errors. This result is due to lack of numerical accuracy in certain C/v_A intervals, due to the values of u_y lying below the accuracy of our computations. Consequently, there are erratic changes of sign in u_y

within velocity intervals dominated by the error, that, of course, cannot be considered an evidence of solitary wave existence. If the branch computation code tries to compute solutions in parametric regions dominated by noise, it may wrongly identify solitary wave solutions, due to these erratic changes of sign. Therefore, regions dominated by the numerical error must avoided when computing branches.

With the current accuracy of the calculations it is not possible to find solitary wave solutions in error-dominated areas. If one wants to explore these areas, the way to proceed would be to detect which numerical method is limiting the accuracy of the computations and try to increased it. When the limit of double precision is reached, the next step wold be to go for quadruple precision —using Mathematica or similar software, as done in article [15]. Then, the numerical noise should decay to lower values and the valid results on $u_y = u_y(C/v_A)$ should cover a wider C/v_A range. However, these are minor details and the present work will focus on solitary wave localization avaoiding parametric regions in which the numerical error dominates on the results for $u_y = u_y(C/v_A)$.

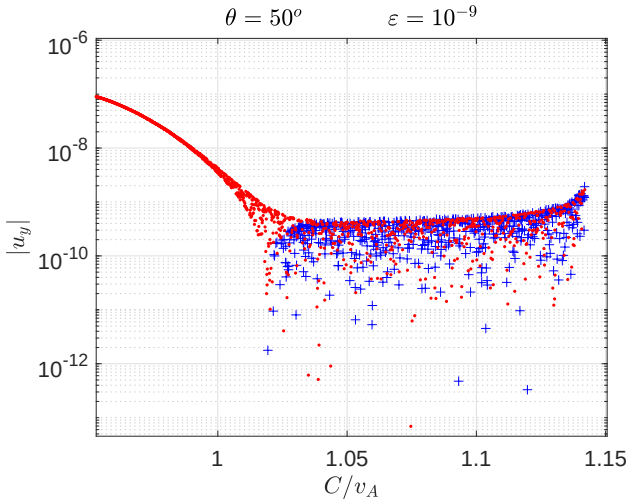

Figure 4.7: $u_y = u_y(C/v_A)$ dominated by the numerical error.
Blue crosses: $u_y > 0$. Red dots: $u_y < 0$.

Regarding the dependence of the results on ε, it seems that $\varepsilon = 10^{-3}$ is not a good choice when looking for solitary waves. Using this value, false positives of solitary existence are being obtained, that disappear as ε is further decreased. In this case, the erratic changes of sign do not have the shape of numerical error so that one could confuse the erratic changes of sign as true evidences of solitary wave existence. However, they cannot be taken as a proof of existence, as long as they disappear when reducing ε. Although, for $\varepsilon = 10^{-6}$, the curve is much more similar to the one for $\varepsilon = 10^{-10}$ —which are the most reliable results—, there are still some changes of sign that disappear at lower ε. At $\varepsilon = 10^{-9}$ there are no false positives, and changes of sign become independent of ε, as it is further decreased. For that reason, $\varepsilon = 10^{-9}$ will be used in future computations. Of course $\varepsilon = 10^{-10}$ is also a good choice. But then, the integration of the equations would take more time, because the initial rate at which the trajectory departs from the equilibrium

is reduced. Therefore, $\varepsilon = 10^{-9}$ is preferred, as a good tradeoff between accuracy and computational speed.

The reader may have noticed that there are some points in Figure 4.6 close to $C/v_A = 1$ that do not fit the curve. This is because, at $\theta = 50^o$ a tiny double existence interval exist close to $C/v_A = 1$, which was not taken into account when making these calculations.

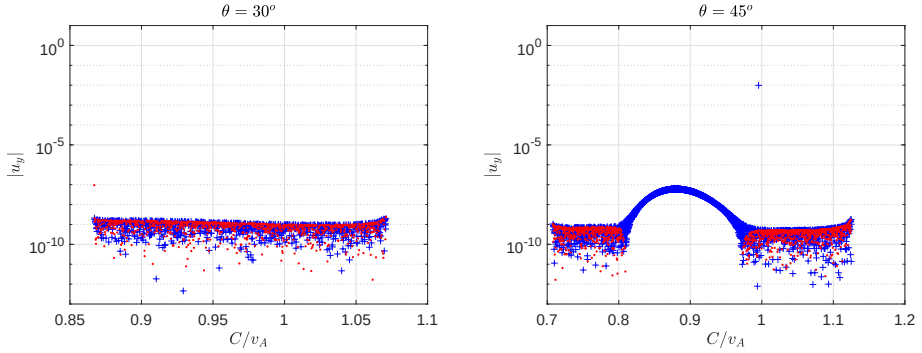

(a) Upper saddle-center region. $\theta = 30^o$ (b) Upper saddle-center region. $\theta = 45^o$

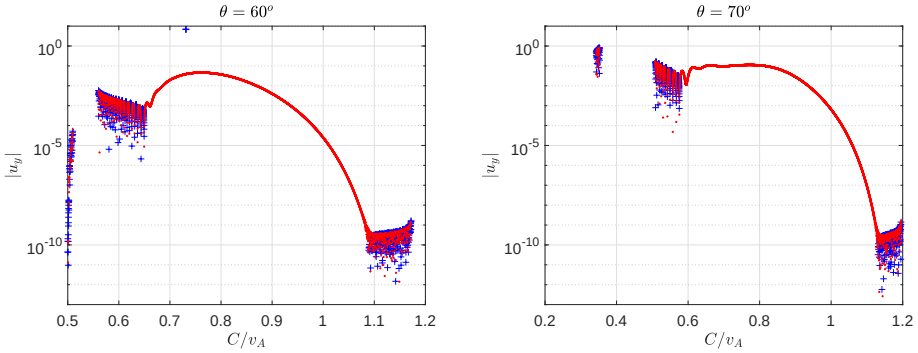

(c) Upper saddle-center region. $\theta = 60^o$ (d) Upper saddle-center region. $\theta = 70^o$

Figure 4.8: $u_y = u_y(C/v_A)$ for several values of θ.
Blue crosses: $u_y > 0$. Red dots: $u_y < 0$.

Results like the ones plotted in Figure 4.6 provide approximate values of C/v_A at which solitary wave solutions exist at certain θ. As mentioned in Section 4.1.2, a branch computation method based on obtaining such results is very time consuming. But they can be used to have a first look on which regions in the parameter space one could expect to find solitary waves and also which regions must be avoided due to lack of numerical accuracy —see Figure 4.9. To do so, $u_y = u_y(C/v_A)$ curves have been computed for θ ranging from 15^o to 85^o, with a spacing of 5^o. Some examples are posted in Figure 4.8 for the upper saddle-center region taking $\varepsilon = 10^{-9}$. The results for $\theta = 30^o$ and $\theta = 60^o$ in the upper saddle-center region are specially interesting because of the solitary wave examples given in [5] at these angles of propagation. However at $\theta = 30^o$ the complete range of C/v_A is dominated by the numerical error, so that it has not been demonstrated that those examples are real solitary waves. Moreover, one example is given in [5]

at $\theta = 60^o$ and $C/v_A = 1.1$, in a parametric region also dominated by numerical noise. It is not strange that the author of [5] gives examples at parameter combinations with u_y dominated by numerical error, since the error takes very small values of u_y. Remember also that the equations used by E. Mjølhus are not completely equal to the ones being used in this project, mainly due to the $1/\hat{b}$ factor explained in previous chapters —but even with this difference in the equations, error dominates more or less in the same parametric regions.

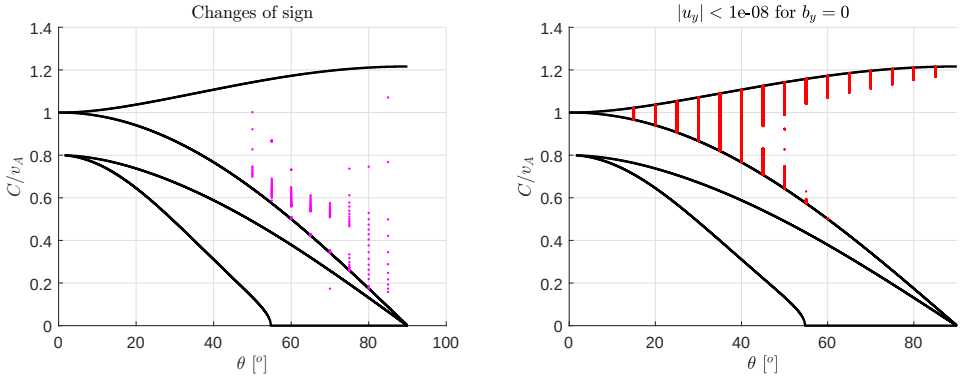

(a) True changes of sing in $u_y = u_y(C/v_A)$.

(b) Points corresponding to $|u_y| < 10^{-8}$. Approximation of the parametric region in which $u_y = u_y(C/v_A)$ results are dominated by numerical error.

Figure 4.9: First scan of saddle-center regions, looking for solitary wave existence.

Figure 4.9(b) can be used to visualize which regions in the parameter space are not going to be explored. The existence of solitary waves in this areas cannot be demonstrated with the current accuracy. For this reason, computations are limited to $\theta \leq 50^o$ in the upper saddle-center region. On the other hand, Figure 4.9(a) is useful to have an idea of the regions occupied by branches of solutions. It also give points that are good candidates for starting the branch computation code. It has been found easier to star the branch computation algorithm at values of θ close to 90º and, then propagate the branches towards lower θ values. The lower saddle-center region does not seem to have velocity intervals dominated by numerical error, but solitary waves have only been found within a small range of θ close to $\theta = 72$º.

4.2.2 Branches of solitary waves solutions

In this section the output from the branch computation code is shown. Results are plotted in Figures 4.10 and 4.11. The numerical settings have been configured in the same way than in the previous section, with $\varepsilon = 10^{-9}$. Every red dot corresponds to an approximate point in the parameter space for which a solitary wave solution can be found. The results are not exact values of C/v_A but intervals with width smaller than 10^{-9}. In the lower saddle-center region, solitary waves have been only found within a small interval of θ and very close to a brown zone.

In Figure 4.11, branches have been plotted on top of the singularity map. It is interesting to see how brown zones —those associated to trajectories hitting the singularity surface— seem to have an influence on the geometry of the branches. In some cases branches start or end in brown zones.

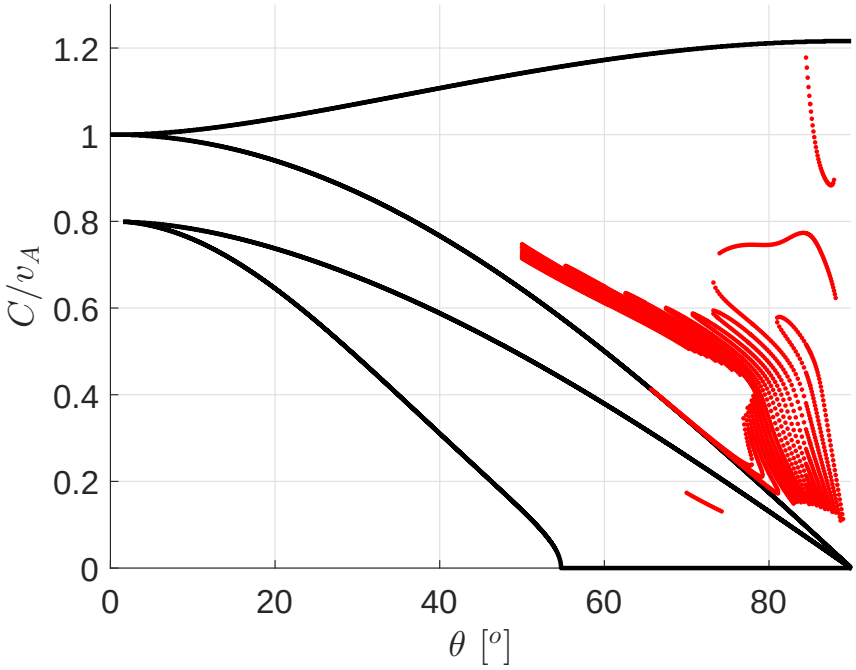

Figure 4.10: Branches of solutions

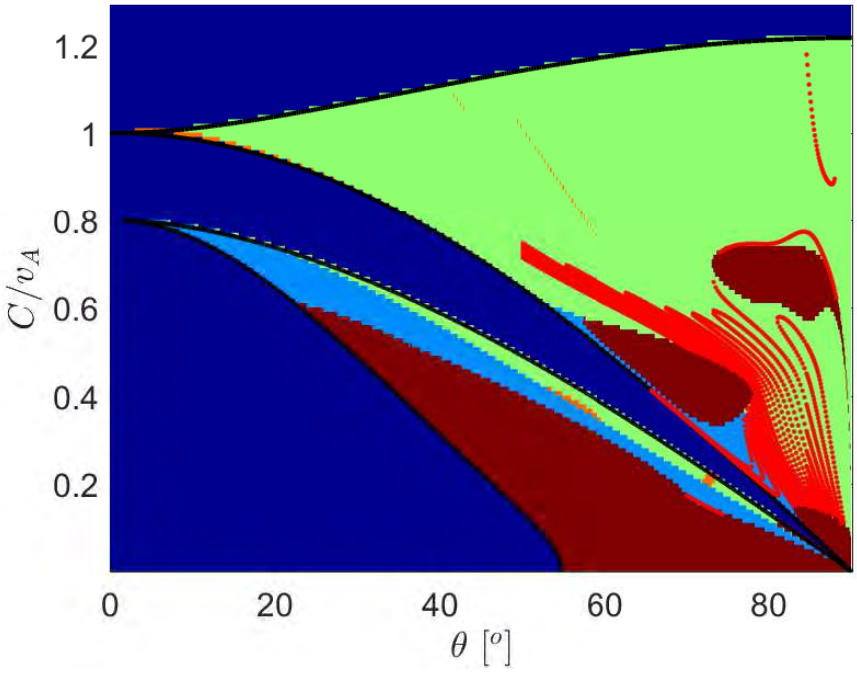

Figure 4.11: Branches of solutions. Plotted over the singularity map.

As a check that the branch computation algorithm is properly designed, results must be coherent with the singularity map and the points in Figure 4.9(a). It has been verified that this is the case.

4.2.3 Solitary wave examples

Figure 4.10 gives plenty of parameter combinations at which the existence of solitary wave solutions has been proved. This part of the thesis shows numerical solutions and discuss some aspects. Firstly, the impossibility of computing exact solitary wave solutions is going to be commented. There is always a small numerical error in the value of the parameters and in the integration. For that reason, the numerical integration of the equations to obtain a solitary wave usually provides results as shown in Figure 4.12. The solution look like a periodically repeated solitary wave. This is because the solution approaches the equilibrium point, but due to the error in the calculations the trajectory separates again from it. The result is an orbit that is very close to the homoclinic orbit but not exact, so that the numerical solution orbits close to the solitary wave in phase space. This is not the only possibility. Cases have been found in which the solution tends to the equilibrium point but the error make the solution to depart from it again and intersect the singularity hypersurface.

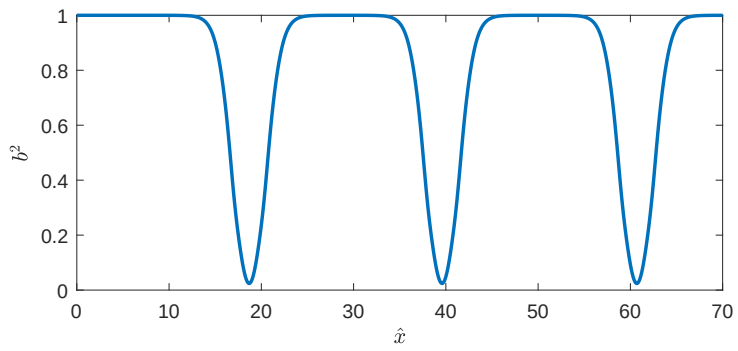

Figure 4.12: Non-exact numerical results of solitary wave solutions.

In previous sections it was introduced the possibility of having positive or negative perturbation on b_z. According to [5], this two cases may be linked to the existence of bright and dark solitary waves. This hypothesis can be checked by looking at the value of b^2 at $\hat{x} = 0$ for every solitary wave in Figure 4.10, being $\hat{x} = 0$ the value of $\hat{x}$ at which the intersection with the symmetric section takes place. In Figure 4.13, branches are plotted again in the parametric plane but the color of the points is related to the value of $(b^2 - 1)$ at $\hat{x} = 0$, i.e. the magnetic amplitude difference with respect the upstream value. Bright solitary waves are defined as having $b^2_{\hat{x}=0} - 1 > 0$, while dark solitary waves are defined with $b^2_{\hat{x}=0} - 1 < 0$. Just looking at the extreme values of $b^2_{\hat{x}=0} - 1$ in the color bar, the existence of both types of solitary waves is evident, among those that have been computed. In every case, bright solutions happen at blue regions in Figure 4.2(a) —those associated with positive perturbation on b_z. But not all solutions lying on this areas are bright. Therefore, the sign of the initial perturbation on b_z

cannot be considered a definitive clue of the type of solitary waves that are going to be found.

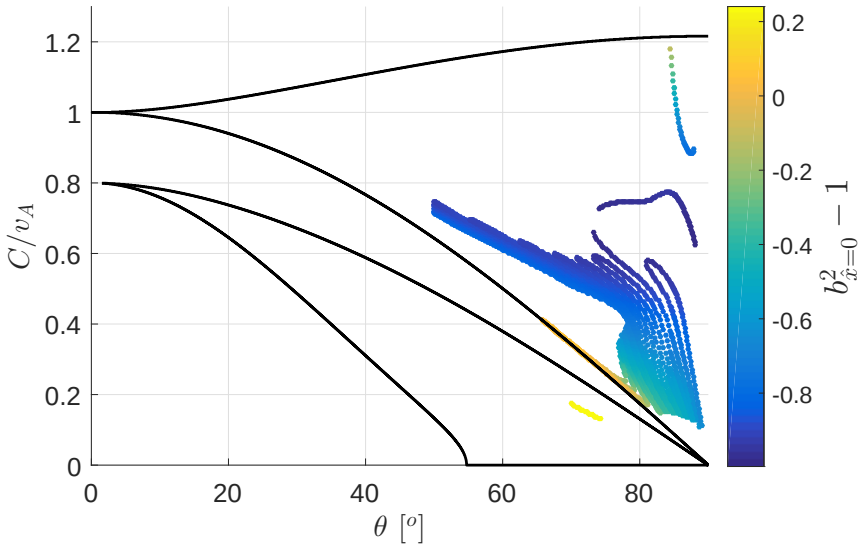

Figure 4.13: Branches of solutions with points colored according to the value of $b^2_{\hat{x}=0} - 1$ at $\hat{x} = 0$.

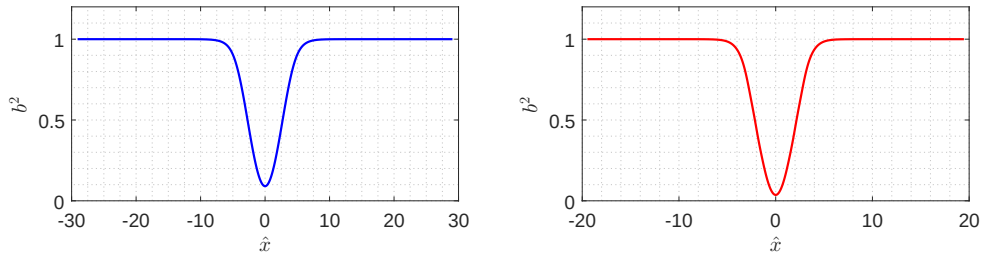

(a) $\theta = 60^o$ and $C/v_A = 0.649526756$ —Upper saddle-center region

(b) $\theta = 74^o$ and $C/v_A = 0.588826627$ —Upper saddle-center region

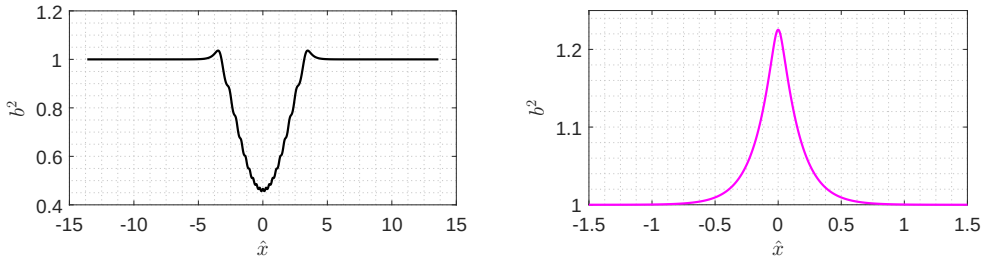

(c) $\theta = 77^o$ and $C/v_A = 0.331351658$ —Upper saddle-center region

(d) $\theta = 70^o$ and $C/v_A = 0.173579614$ —Lower saddle-center region

Figure 4.14: Examples of solitary solutions. Magnetic field amplitude.

In Figures 4.14 and 4.15, several solitary waves are plotted. In general, it can be noted that lower values of θ give smoother curves in the case of the upper saddle-center region. In the lower region, the example in Figure 4.14(d) and 4.15(d) shows

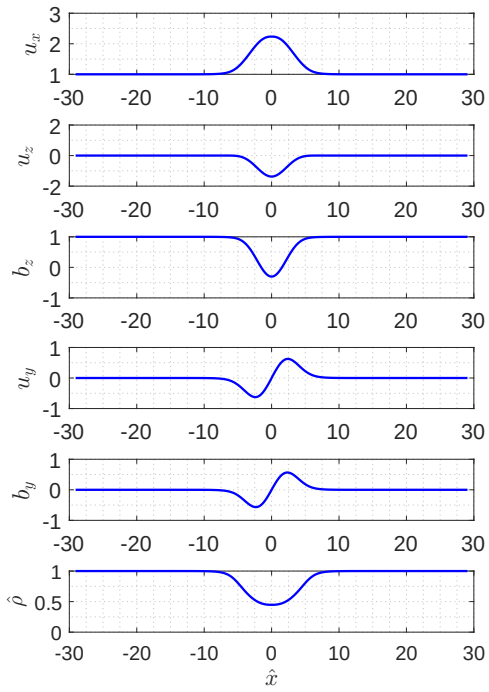

(a) $\theta = 60^{\circ}$ and $C/v_A = 0.649526756$

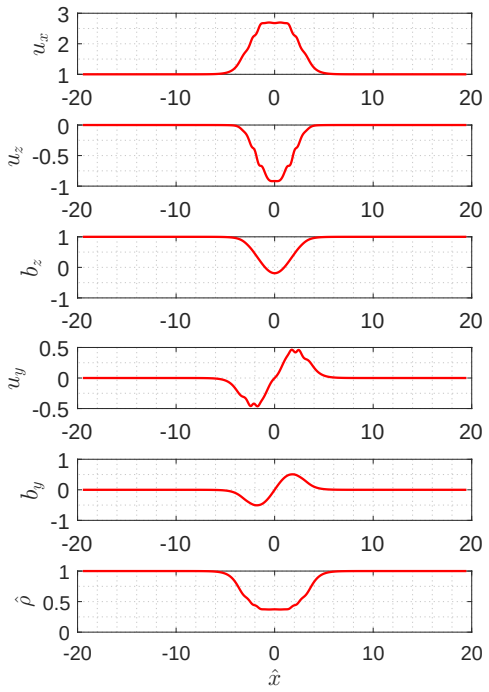

(b) $\theta = 74^{\circ}$ and $C/v_A = 0.588826627$

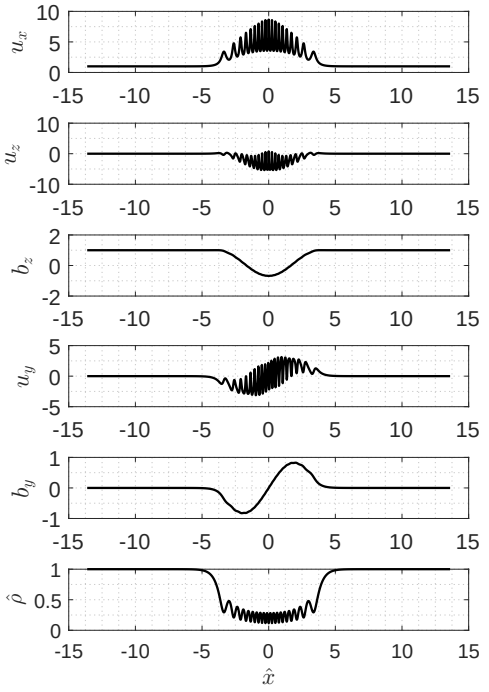

(c) $\theta = 77^{\circ}$ and $C/v_A = 0.331351658$

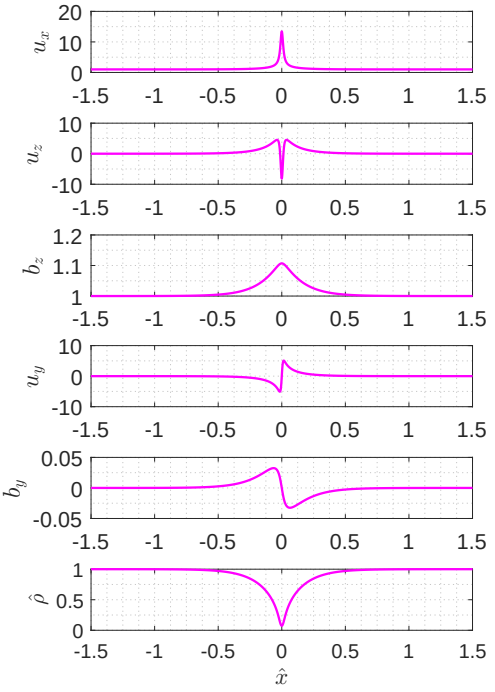

(d) $\theta = 70^{\circ}$ and $C/v_A = 0.173579614$

Figure 4.15: Examples of solitary wave solutions. State variables.

that the solitary wave takes place in a very narrow $\hat{x}$ interval. The non-dimensional length of this solitary wave is much smaller than in the other cases. Figure 4.14(a) and 4.14(b) correspond to trajectories with negative initial perturbation on b_z, while 4.14(c) and 4.14(d) start the integration with positive perturbation in b_z. These last cases were supposed to deliver a bright solitary waves according to the b_z-perturbation criterion, but this is not what we are obtaining, as discussed for Figure 4.13 in the previous paragraph. The example in Figure 4.14(c) is a dark solitary wave according to the value of $b^2(\hat{x}) = 0$. However, the magnetic field amplitude initially increases with respect to the upstream value like a bright solution, due to the positive perturbation on b_z. Although a positive perturbation on b_z leads initially to $b^2 > 1$, it is not guaranteed that $b^2 > 1$ for every $\hat{x}$.

4.2.4 Dispersion results and Fast Fourier Transform

In this section, a suitable solution to carry out time evolution calculations will be found. This type of simulation will give information on the stability of the solutions in time. The objective is to find stable solitary wave solutions. The initial approach is to search smooth solitary waves with no linear instabilities within its wavenumber range. The reason is to guarantee that the equilibrium state is stable. However, it cannot be known in advance if the solitary wave solution itself is stable or not. An analytical approach to study the stability of solitary wave solutions would involve the linearization of FLR Hall MHD partial differential equations around a solitary wave solution. Then, the evolution of the perturbations on the solution could be studied. However, this analysis is complex, so that, for the moment, the stability of the solutions will be studied by means of computing its time evolution. The part of the project dedicated to stability of solitary waves is out of the scope of this thesis, which is focused on existence of solutions.

The same examples than in the previous section will be used to show dispersion relations and FFT results. The example of Figure 4.15(c) is not smooth and varies very rapidly with $\hat{x}$, so that it is expected that small scale —i.e. large k— components of the FFT are important, i.e. the FFT will cover a wide range of wavenumbers with significant energy associated to it. This is also the case of the solitary wave in Figure 4.15(d). In this case the solutions seems more smooth than in the case (c), but the solitary wave length is very small.

Dispersion relations for the same examples are shown in Figure 4.16. To be precise, Figure 4.16 plots the maximum imaginary part of all ω solutions. When any ω has positive imaginary part, any perturbation on the equilibrium state will grow with time. The FFT are plotted in Figure 4.17. As explained, solutions with fast variations in the $\hat{x}$ space result in a wider FFT in the k space. In every case, the dispersion relations show linear instability starting at wavenumbers with large value of the FFT. Therefore, none of this examples is expected to be stable, because the equilibrium itself is not. The FFT of the state variables reveal that unstable modes are excited with high probability. In fact, making a parametric survey on dispersion relations, the nominal values of the parameters do not seem to be a good choice in order to look for stable equilibrium conditions. Therefore,

the values of a_p, $v_\perp/v_A$ and $v_{se}/v_\perp$ have to be modified. Solitary wave solutions with the required characteristic have been found for $a_p = 1.24$, $v_\perp/v_A = 0.4$ and $v_{se}/v_\perp = 1.19$. The corresponding stability and singularity maps have been already displayed in Figures 4.1 and 4.2. One example is shown in Figure 4.18. According to dispersion relations there are no noticeable linear instabilities. The results in Figure 4.19 are different from the exact zero due to numerical error. In this case, no instabilities are expected on the equilibrium state but the stability of the solitary is still to be proved.

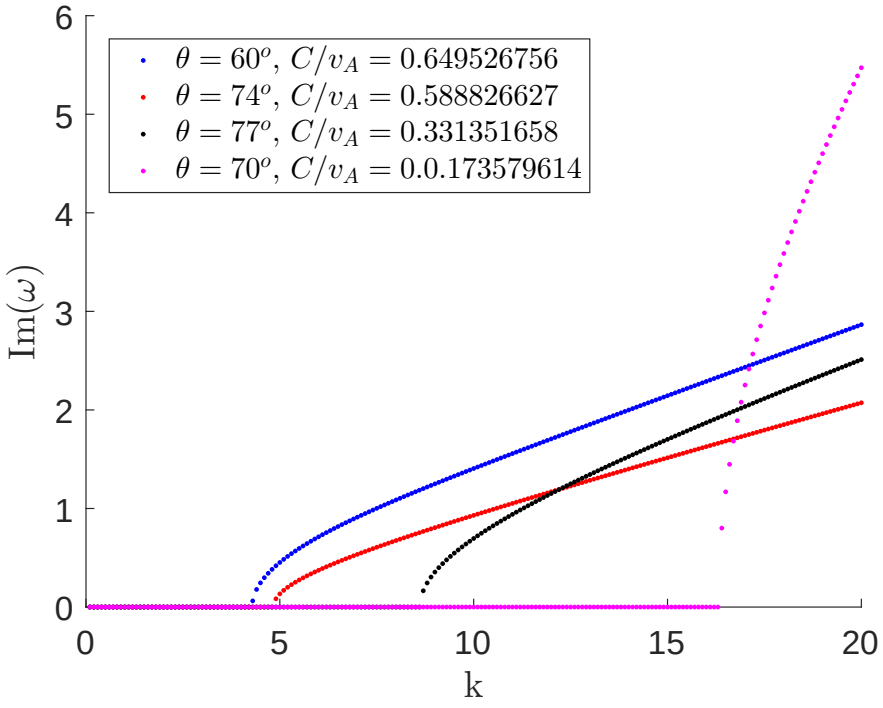

Figure 4.16: Maximum imaginary value of all $\omega = \omega(k)$ relations.

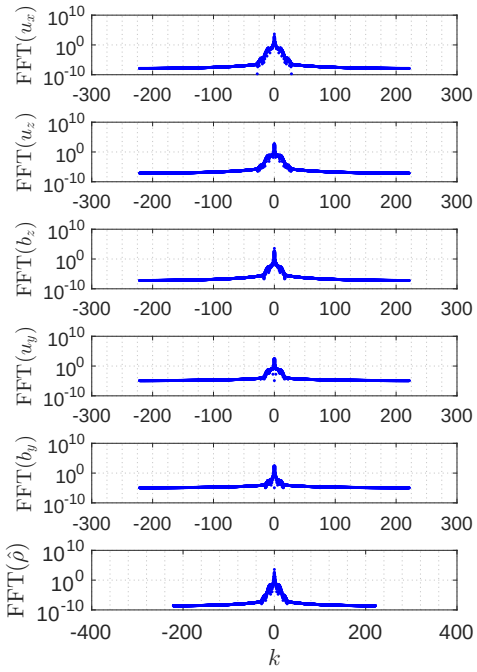

(a) $\theta = 60^{\circ}$ and $C/v_A = 0.649526756$

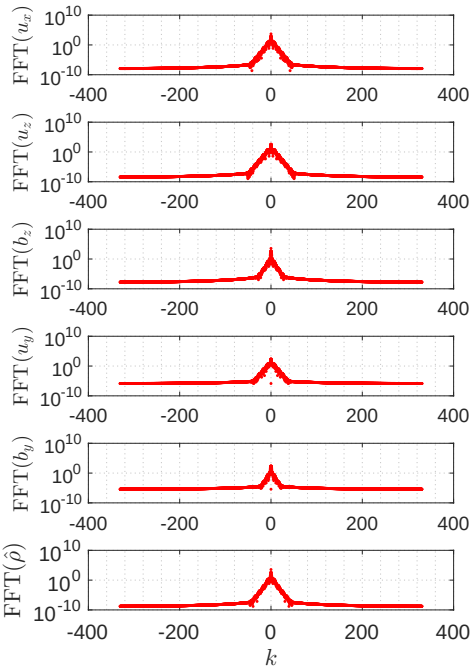

(b) $\theta = 74^{\circ}$ and $C/v_A = 0.588826627$

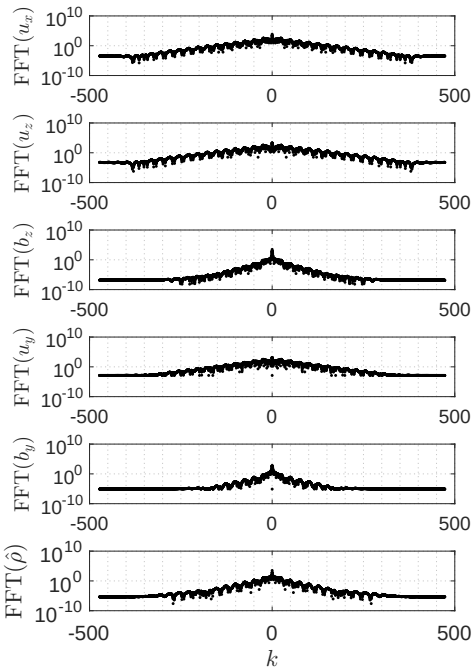

(c) $\theta = 77^{\circ}$ and $C/v_A = 0.331351658$

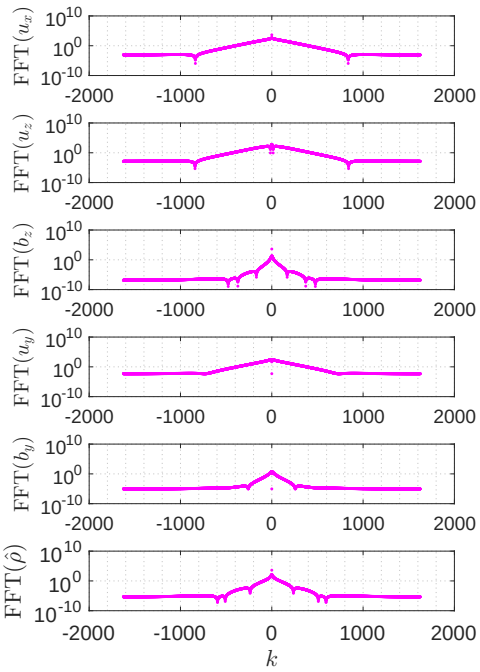

(d) $\theta = 70^{\circ}$ and $C/v_A = 0.173579614$

Figure 4.17: Examples of solitary wave solutions. Fast Fourier Transform.

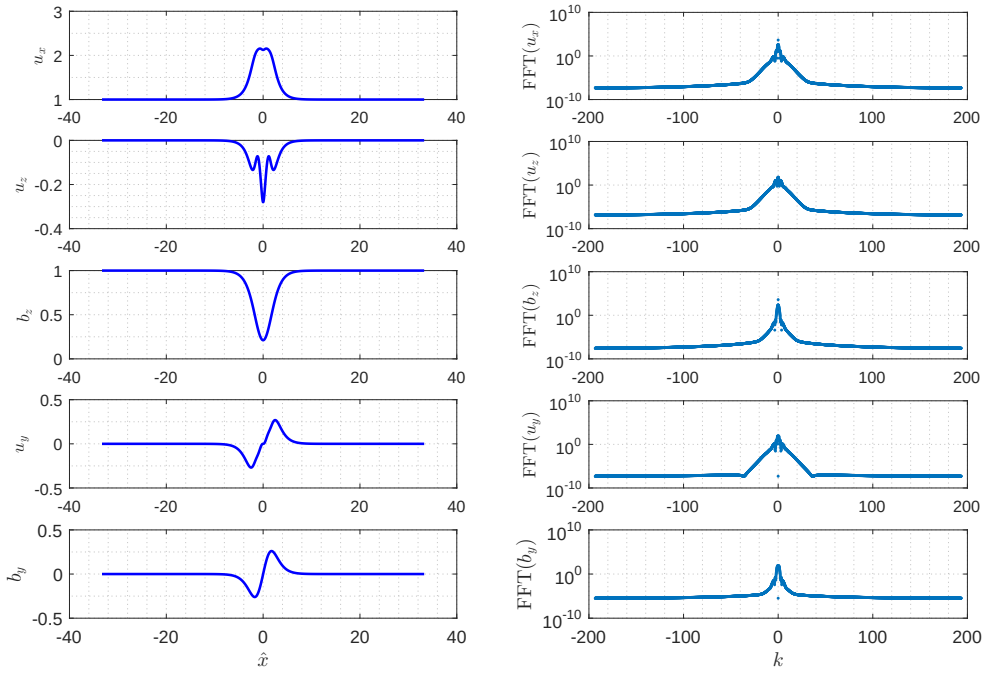

(a) State variables. (b) Fast Fourier Transform

Figure 4.18: Solitary wave solution suitable for time evolution simulations. $a_p = 1.24$, $v_\perp/v_A = 0.4$, $v_{se}/v_\perp = 1.19$, $\theta = 85^o$ and $C/v_A = 0.792359815$.

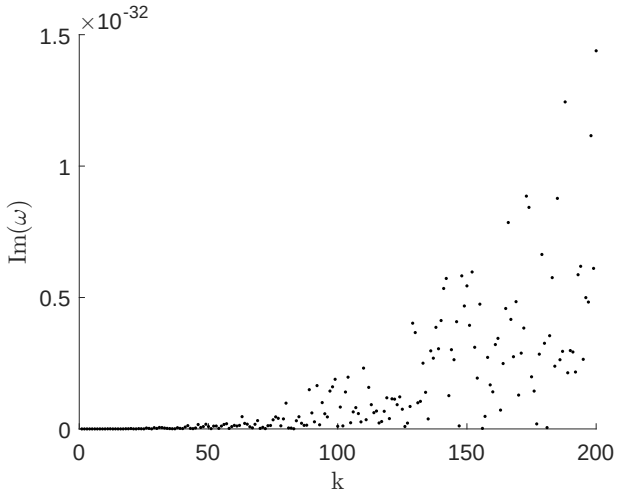

Figure 4.19: Maximum absolute value of all $\omega = \omega(k)$ relations. Parameters are the ones used in Figure 4.18.

4.2.5 Dimensional example of solitary wave

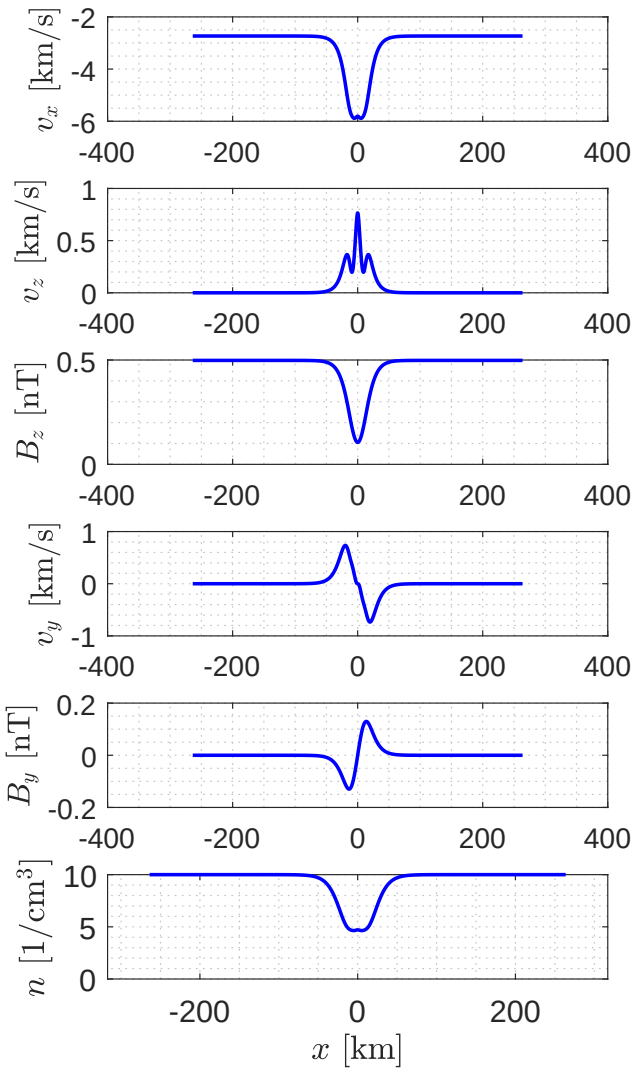

Figure 4.20: Solitary wave example in Figure 4.18, with dimensions.

Although the problem has been solved in non-dimensional form, it may interesting to see an example of a solution with dimensions. To be precise, the typical longitudes of solitary waves may be important in the design of an hypothetical space mission for the observation of these phenomena in space. In order to re-dimensionalize one solution, reasonable values of the ambient magnetic field B_0 and upstream number density of ions n_0 have to be assumed. They have been taken from space observations reported in the literature. Other data, such as the electron charge or the speed of light, have well-known values. Since Gaussian units are being used in this project, the magnetic field should be expressed in G, the electric charge in statC and the rest of data in terms of centimeters, grams and

seconds, in order to keep coherence with the units. The constants

$$e = 4.8032 \cdot 10^{-10}\ \text{statC}$$

$$m_i = 1.6726 \cdot 10^{-24}\ \text{g}$$

$$c = 3 \cdot 10^{10}\ \text{cm s}^{-1}$$

can be used, together with

$$B_0 = 0.5\ \text{nT} = 5 \cdot 10^{-6}\ \text{G}$$

$$n_0 = 10\ \text{cm}^{-3}$$

and the corresponding values of θ and C/v_A to compute the Alfvén speed, the characteristic velocity v_{0x} and the characteristic longitude ℓ. Velocities are dimensionalized with $v_{0x} = -(C/v_A)\, v_A$, magnetic fields with $B_0 \sin\theta$ and density with ρ_0. The characteristic velocity v_{0x} is negative, as long as the solitary wave moves in the positive x direction.

In Figure 4.20 the example in Figure 4.18 is plotted with dimensions. It has been decided to plot number density instead of mass density —they relate by means of the ion mass. The dimensional results in Figure 4.20 gives the expected order of magnitude of the solitary wave longitude and the dimensional state variables.

Chapter 5

Scientific Space Mission

In this chapter, a hypothetical space mission oriented to magnetic holes measurement is discussed. Including an overview on the instruments needed to take the required data. Finally, some of the regulatory and socio-economic aspects of the project will be exposed.

The objective of the proposed mission is to detect and measure magnetic holes and to try to characterize them as solitary waves. Moreover, it would be interesting to keep exploring the Sun at other latitudes than the ecliptic plane —continuing with the observations made by Ulysses. Once magnetic hole data have been recorded it would be very interesting to compare them with the results computed using FLR Hall MHD equations. Moreover, in the case of conditions leading to saddle-center stability, the assumed model predicts the existence of solitary wave solutions at some specific conditions —e.g. propagation angle θ and velocity C/v_A. Therefore, one objective is to verify whether the conditions when magnetic holes are detected coincide with the predictions or not. According to [5], the magnetic holes observed so far belong to saddle-saddle and focus-focus equilibrium conditions. Unfortunately, numerical results have not been obtained yet in this parametric regions in the FLR Hall MHD model. Whether real magnetic holes exist in saddle-center equilibrium conditions or not is still not known.

Additionally to the existence problem, the stability of solitary wave solutions is still an open subject. No conclusions have been obtained so far. Some aspects have been commented in this thesis, but there are a lot of work to do in this field. In models, the existence of solutions can be mathematically demonstrated independently of their stability. However, unstable solitary wave solutions are not expected to appear in nature. On the other hand, stable solutions may act as attractors and the flow evolve to such solitary wave solutions. Once the stability of solitary waves is assessed, it would be interesting to analyze if the observed solution are related to stable solution to the model.

The proposed space mission involves a constellation of at least two spacecraft. According to the definition of solitary wave, they are structures that propagate without deforming inside a medium in equilibrium. If magnetic holes are solitary waves in solar wind, several probes in the constellation should detect the same

magnetic structure at different times.

The constellation layout and the orbit of the spacecraft must be decided and this is a complex task, out of the scope of this work. There would be a lot of work to do regarding orbital mechanics. The most simple configuration consists on placing two probes aligned with the plasma stream, i.e. two spacecraft orbiting around the Sun and aligned with it. However, this layout cannot be maintained in time. The orbital velocity of the inner spacecraft would be higher and, thus, both spacecraft will separate gradually.

Considering such simple configuration do not lead to promising conclusions. Another possibility is to play with the gravity interaction of the Sun and a planet. This system is much richer in terms of dynamics and possible trajectories. As it was mentioned in Chapter 1, the Lagrange points are of especial importance in space observations —Earth's L1 in the case of solar missions. There are plans for future spacecraft constellation missions orbiting in Lagrange points. This is the case of Laser Interferometer Space Antenna (LISA), an ESA's project composed of three spacecraft, that is intended to measure gravitational waves in space[1]. An arrangement of spacecraft forming a triangle and placed in a Lagrange point, similar to the LISA constellation could be used.

Another good example of space mission involving a spacecraft constellation is Cluster, which consist of four probes orbiting the Earth. Its objective is to study the Earth's magnetosphere and its interaction with solar wind, three-dimensionally. Solitary waves have already been measured by Cluster, with observations of the same undeformed structure at several points in the constellation. The mission proposed in this project is intended to observe this kind of events in the interplanetary space —without interacting with planet's magnetospheres. Therefore the Cluster mission could be a good reference point to start the design of the spacecraft constellation and solve the orbital problem.

It has been shown that it is not possible to have a constellation of probes permanently aligned with the solar wind. Although in this project the computations are made in 1D, real magnetic holes have longitudinal and lateral dimensions. Therefore, it is not required that probes are aligned to measure the same magnetic hole. However, if the lateral separation, with respect to the propagation direction, of two probes is greater than the lateral longitude of the magnetic hole, the event will not be measured at both points. Unfortunately, the 1D analysis gives no information about the lateral longitude of the structures. This information would be very useful for the design of the constellation layout. In fact, the expected order of magnitude of the longitudinal longitude of solitary waves must also be taken into account. From the results in this thesis an estimation of the longitudinal distance

[1] Gravitational waves have been already detected by LIGO, an Earth-based observatory. The first detection was made on 14 September 2015, confirming the existence of these kind of waves, predicted by Einstein's general relativity. The key of space-based observatories is that they can be of sizes that are not possible on Earth. Increasing in this way the sensitivity to large wavelengths.

covered by one solitary wave can be obtained, as it has been shown in Section 4.2.5

Apart from the orbital details of the mission, the space probes must be equipped with the proper experimental measurement equipment. In order to take the required measurements, the spacecraft should be equipped with instruments capable of measuring the magnetic field vector and the plasma macroscopic properties —mainly the velocity vector and the density. There are a lot of types of instruments and techniques that can be used. The probe Ulysses has been taken as the starting point for the selection of the equipment, due to the similar type of data in Ulysses mission and the proposed one. Of course, experimental equipment should incorporate up-to-date versions of the instruments and telemetry systems in Ulysses. Some of the are described below:

- Magnetometer. The device responsible of measuring the magnetic field. Two types can be distinguished: *scalar magnetometers* and *vector magnetometers*. Of course, the required data include magnetic field components, so that vector magnetometers are the ones to be used. An additional requirement for the sensor is to have enough sensitivity so that it is able to measure the weak interplanetary magnetic field. This factor was already taken into account in the design of Ulysses, which incorporates two different types of magnetometers: *Vector Helium Magnetometer* and *Fluxgate Magnetometer*. Using two magnetometers based on different principles has the advantage of self-validating the magnetic field data and compensating any background field or artificial field produced by the spacecraft itself.

  According to [16], Ulysses was able to sample two magnetic vectors per second. The factor limiting the sampling rate is not related to magnetometers but to telemetry. However, whenever sudden significant variation of magnetic field were detected an event was raised and the sampling frequency was increased by using additional channels. In this way, interesting phenomena are captured with more resolution. A similar system could be implemented in the proposed mission. It may not have sense to have an extremely good continuous sampling rate, but only when an event is happening. Of course, telecommunications —and technology in general— are today better than when Ulysses was designed and built, so that the sampling frequencies can be higher in a new mission.

- Channel Electron Multipliers (CEM). Sensors able to detect charged particles —as well as several ultraviolet radiation, hard and soft X-rays. The Ulysses spacecraft was equipped with 16 CEMs. These sensors can be employed in detecting ions and the recorded data can be used to compute velocity distribution functions of ions —just as the ones described in Chapter 2 but eliminating the dependency on the positions, since measurements are taken at certain location. As highlighted in Chapter 2, distribution functions contain a lot of physical information about the plasma. By knowing the distribution function of ions at several time instants, the evolution of average macroscopic density and velocity of the plasma can be computed. This is also interesting for the objectives of the mission. The type of data recorded

by the CEM sensors is very heavy. For this reason Ulysses was able to obtain samples every 4 minutes when transmitting and every 8 minutes when storing the data.

The instruments used by Ulysses devoted to plasma measurements can be taken as a starting point, from which the details of a new mission of similar characteristics can be specified.

5.1 Regulatory frame — The Space Law

Human activities in space are submitted to regulation: the *space law*. There exist international treaties and agreements governing and limiting them. The existence of space law is a necessity and it will become more and more important and complex in the future, as the human presence in space continues growing. The term *space law* refers not only to international law but also to any law regulating space activities that may be defined at national level. Since the space law applies in outer space, a rigorous definition of *outer space* is required —although the lack of it has not been a problem so far in history. The transition from Earth's atmosphere to space is gradual —i.e. there is no clear boundary—, which makes the definition of outer space is problematic. It seems that most lawyers agree on the Kármán line as the border to outer space.

The *Kármán line* was defined by Theodore von Kármán as the altitude beyond which the speed of an aircraft required to fly leveled exceeds the orbital velocity —for typical wing loading values. As the aircraft flies higher the density decrease has to be compensated with an increase in the true airspeed, so that lift is able to compensate the weight —without taking into account the wind or the centrifugal force due to curvature in the aircraft trajectory, which follows the Earth's surface. At the altitude corresponding to the Karman line, the value of the required speed matches the orbital velocity of that particular altitude. This calculation provides a value close to 100 km, but the value 100 km is used because it is easier to remember. This boundary from Earth to outer space is accepted by the Fédération Aéronautique Internationale (FAI) and serves also to separate aeronautical from astronautical activities.

The space law organizes around five treaties and five principles, whose objective is to promote international cooperation and peaceful space activities. The authority in charge of regulating the space law is the Committee On the Peaceful Uses of Outer Space (COPUOS), created in 1959 and dependent on the General Assembly of the United Nations. The main treaty is the *Outer Space Treaty*. Some of the subjects that it addresses are: the right of every nations to explore space and space exploration as source of enrichment for all nations, the prohibition of weapons in space or in any celestial body other than Earth and liability of nations for any damage caused by space objects. The other four treaties have the purpose of giving support to the Outer Space Treaty in subjects such as: rescue and support to astronauts —the *Rescue Agreement*—, details of the liabilities in case of damages or astronaut deaths —the *Liability Convention*—, the registry

of space objects —the *Registration Convention*— and the usage and ownership of the Moon and other celestial bodies —the *Moon Agreement*. The five principles, in turn, support the mentioned treaties.

An hypothetical space mission for studying solar wind and magnetic holes should take into consideration the space regulations, in order to maintain an international environment of mutual enrichment among nations and promote the sustainable and responsible use of the outer space. In addition, cooperation and coordination is needed in order to carefully prepare the mission and avoid damaging existent and planned space objects. Failure in fulfilling the international agreements and treaties could also lead to diplomatic conflicts.

5.2 Socio-Economic environment

As it was pointed out in Chapter 1, one of the motivations of this thesis is to keep expanding the knowledge about solar wind phenomena. It is important to understand the physical processes of heliophysics since it affects humans in a wide variety of aspects. One of them is the effect of solar wind on spacecraft. Those that orbit close to the Earth are partially protected by the Earth's magnetic field. This natural protection may not suffice and it is not always available, depending on the location of the spacecraft. One of the threads of solar wind to space probes is that different parts may become charged, creating differences in potential that can end in a fast discharge from which some components may result damaged. Moreover some energetic particles may go through the spacecraft skin and reach electronics. Solar wind may have also effects noticed on the Earth, since may telecommunication systems rely on communication satellites. Of course, preventions and shielding against solar wind are already included in spacecraft, but a better solar wind understanding will help to the research and development of more efficient or advanced techniques.

The development of solar wind shielding technologies has a socio-economical perspective. Space missions suppose an incredible money investment. If a key component is damaged —for example, as a result of an encounter with highly energetic solar wind particles— once the spacecraft is already in space the complete mission or an important part of it may become ruined. Space agencies are funded with public money, that brings along with it certain social responsibility. In addition, any funds invested in space exploration and wasted due to a mission failure have attached bad advertising, which may negatively affect to the budget of subsequent years. On the other hand damage caused on commercial satellites has also an impact on the economy.

5.2.1 Project expenses

Apart from the socio-economic aspects discussed so far regarding the study of the physics of the Sun, other economical concerns are the expenses generated by this particular project. They are listed below:

- Complete MATLAB academic license —provided by Universidad Carlos III: 405€.
- Amortization of the computer used to do the computations. The complete cost of the computer, together with the screen, keyboard and mouse, was 810€. The duration of the project has been approximately one year. Considering linear depreciation and a computer useful life of five years, the cost of the computer equipment associated to this project is: 81€.
- Visit of one week in Nice Observatory to continue the part of the project related to time evolution and stability of solitary waves, in collaboration with Drs. Thierry Passot and Dimitri Laveder. The expenses of the visit can de divided in:
  - Flight tickets MAD-NCE and NCE-MAD: 193€
  - Accommodation: 200€

The total cost of the project is approximately 879€. About 46% of the cost corresponds to the MATLAB license. UC3M provides the license to every university researcher and student, so that it is not a cost directly linked to this particular project. However, if a MATLAB license is not available, cost can be significantly reduced by using an alternative numerical software. A good alternative is the Python distribution Anaconda, which is free and includes all the tools necessary to run Python code and the main scientific computation packages.

Chapter 6

Conclusion

The main subject addressed along this thesis is the existence of solitary waves in the Magnetohydrodynamic model with Hall and Finite Larmor radius effects. A topic that has received attention due to recent observations of magnetic field depressions in the solar wind. This type of structures are denominated magnetic holes. They have been tried to be explained in terms of solitary wave solutions to MHD models. Solitary wave arise as solutions to systems of partial differential equations and are important in may fields of physics and engineering.

This study takes up the torch of [5] by E. Mjølhus, who derived the dynamical system associated to the FLR Hall MHD model, making the hypothesis of travelling one-dimensional wave solution. In addition, in [5] some details about the suitable numerical methods are given, as well as some numerical solitary-wave-like solutions. However, it is stated in the discussion of the results of [5], that its results should not be taken as a proof of solitary wave existence. The present work gives a formal existence criteria and demonstrate the existence of solitary wave solutions in saddle-center equilibrium conditions.

This research is made in the frame of a better understanding of the solar wind plasma phenomena and a hypothetical space mission devoted to magnetic holes detection is proposed in Chapter 5. Therefore, it has been considered convenient to introduce some topics related to plasmas, the Sun, magnetic holes and space missions. In Chapter 2, the subject of plasma models is the main topic. This a very complex subject, so that the theory in Chapter 2 is very summarized. Different approaches exists to plasma models. The approach used in this thesis is to consider the plasma as a conducting fluid in which the plasma state is defined by its macroscopic properties. The resultant set of equations consist of macroscopic fluid equations coupled with Maxwell's equations of electromagnetism. From these equations, several MHD models are obtained, depending on the assumptions made. The model chosen for solar wind is the FLR Hall MHD model with double adiabatic model for the ion pressure.

Apart from the plasma physics, some notions on dynamical systems and solitary waves have been required, which are exposed in Chapter 3. Article [2] by A.R. Champneys gathers certain interesting properties of reversible even-dimensional

dynamical systems. The concepts of reversibility and symmetric section are key in order to understand the solution proposed to the concerning problem. In Section 3.2, the importance of the stability of the equilibrium point and reversibility in solitary wave existence is highlighted. The main conclusions from [2] applicable to the FLR Hall MHD system are: solitary waves cannot exist if the equilibrium is center-center, they are expected to exist as a continuum –codimension zero— in focus-focus and saddle-saddle parametric regions, and as branches of solutions —codimension one— in saddle-center areas.

The results in this thesis focus on the existence of solitary waves on saddle-center equilibrium. This work defines a rigorous criterion for solitary wave existence in saddle-center regions. If a solution is found departing from equilibrium along an unstable direction and intersecting the symmetric section, it can be guaranteed that the state-space trajectory will return to the equilibrium. This is translated into $u_y = 0$ and $b_y = 0$ simultaneously at some $\hat{x}$. An algorithm looking for this intersection has been explained in detail in Chapter 4. The results obtained seems to be coherent with the conclusions extracted from [2], i.e. solitary wave solutions are organized in branches in saddle-center regions of the parametric plane. Also in this chapter an algorithm for branch computation is described. In every process, the existence of a singularity hypersurface defined by $\Gamma(\mathbf{u}, \mathbf{b}) = 0$ must be taken into account. However, the problem of solitary wave existence is not completely solved but partially. Mathematical evidences of solitary wave existence in saddle-saddle and focus-focus stability are still to be obtained. Although it is expected to have solitary wave solutions for every combination of parameters within these regions, the lack of a suitable numerical method —according to [5]— make no possible to verify it, so far. But all the work, conclusions and acquired experience when solving the saddle-center problem provides an invaluable background that will help, for sure, in solving the solitary wave existence problem in other stability conditions. An example of this experience is the way used to deal with the singularity hypersurface.

Finally, in Chapter 5 an hypothetical space mission for study of solitary waves in the solar wind is discussed. The proposed mission would consist on several space probes forming a constellation. The choice for the constellation shape and the orbital problem are complex and need still to be solved. The space missions LISA and Cluster involve spacecraft constellations, so they may be a good example that serve as initial guide. Descriptions on the required experimental equipment are also given, based on the instruments used in the Ulysses mission. The two basic required types of instruments are magnetometers and Channel Electron Multipliers. On the other hand, the main concepts of space law are introduced, as the main regulatory frame affecting human activities in space. At the end of the chapter the economical benefits and social concerns of a better understanding of solar wind are discussed, together with a summary of the expenses of the project. The potential benefits of studying the solar physics are mainly related to the mitigation and prevention of detrimental effects caused by solar phenomena.

6.1 Future challenges

As already mentioned, this thesis has solved in part the problem of existence of solitary wave solutions. There is work to do on solitary existence, but not only. This thesis opens the window to other research topics. The main points are summarized here:

- A numerical method must be developed that is suitable to demonstrate solitary wave existence in the FLR Hall MHD model for saddle-saddle and focus-focus stability. In the case of saddle-saddle, the starting point should be the numerical method described in [5]. The author states that the method did not lead to satisfactory results, but the reasons should be investigated.

- The current branch computation algorithm can be substituted by an arc-length continuation algorithm, capable to deal with any shape of branch curves.

- There are saddle-center parametric regions that could not be explored due to the numerical error. Although solving this problem is not a priority, it is still a way of improving current results in saddle-center parametric regions.

- There is also work to do on the topic of stability of solitary wave solutions. This document includes some comments on time evolution simulation and small-amplitude stability related to dispersion relations. The stability may be assessed from the results of simulations or using an analytical approach.

- It was pointed out in Section 2.2 that the double adiabatic equations for parallel and perpendicular pressure assume the magnetic induction equation without the Hall term and neglects Finite Larmor Radius terms on the energy equation. These assumption seems to be contradictory. Hall dispersion is kept in the magnetic induction equation in both the Hall MHD and FLR Hall MHD model. Moreover, the momentum equation of the FLR Hall MHD system accounts for FLR effects.

  Instead of assuming simplified pressure models, the evolution of $p_{\parallel}$ and $p_{\perp}$ could be obtained as solution to the energy equation with partial differential equations. Without neglecting Hall and FLR effects. However, in this case the problem of solitary wave existence is much more complex. The dimensions of the dynamical system is increased in 2, being $p_{\parallel}$ and $p_{\perp}$ new state variables. Taking into account the invariant $H(\mathbf{u}, \mathbf{b}) = 0$, the new dynamical system is 6D. This is still coherent with the theory in [2]. However, when including $p_{\parallel}$ and $p_{\perp}$ as state variables the reversibility of the system is broken so that conclusions from [2] do not apply, and neither the basis of the current algorithm. A new method would have to be designed to localize solitary wave solutions and the nonexistence of the symmetric section, together with the increased number of dimensions, make the task harder.

  Although the complexity of the dynamical system increases significantly by introducing partial differential equations for $p_{\parallel}$ and $p_{\perp}$, a numerical code

solving the unsteady equations require only to include new expressions for pressure evolution. One possibility is to give as initial condition solitary wave solutions computed with double adiabatic equations from the dynamical system and observe the evolution with the new set of PDEs. Maybe, if the solitary wave is stable it will self-adapt to a new solitary wave, solution to the system with dynamical equations for pressure.

Bibliography

[1] E Mjølhus. Velocity–amplitude relationships and polarizations in families of MHD solitary waves. *Physica Scripta*, 2006(T122):135, 2006.

[2] AR Champneys. Homoclinic orbits in reversible systems and their applications in mechanics, fluids and optics. *Physica D: Nonlinear Phenomena*, 112(1-2):158–186, 1998.

[3] JM Turner, LF Burlaga, NF Ness, and JF Lemaire. Magnetic holes in the solar wind. Technical report, National Aeronautics and Space Administration, Greenbelt, MD (USA). Goddard Space Flight Center, 1976.

[4] D Winterhalter, M Neugebauer, BE Goldstein, EJ Smith, BT Tsurutani, SJ Bame, and A Balogh. Magnetic holes in the solar wind and their relation to mirror-mode structures. *Space Science Reviews*, 72(1-2):201–204, 1995.

[5] E Mjølhus. Finite Larmor radius influence on MHD solitary waves. *Nonlinear Processes in Geophysics*, 16(2):251, 2009.

[6] U Feldman, E Landi, and NA Schwadron. On the sources of fast and slow solar wind. *Journal of Geophysical Research: Space Physics*, 110(A7), 2005.

[7] A Rees, A Balogh, and TS Horbury. Small-scale solitary wave pulses observed by the ulysses magnetic field experiment. *Journal of Geophysical Research: Space Physics*, 111(A10), 2006.

[8] K Baumgärtel. Soliton approach to magnetic holes. *Journal of Geophysical Research: Space Physics*, 104(A12):28295–28308, 1999.

[9] J. A. Bittencourt. *Fundamentals of plasma physics*. Springer Science & Business Media, 3rd edition, 2004.

[10] R. M. Kulsrud. *Plasma physics for astrophysics*. Princeton University Press, 2005.

[11] GF Chew, ML Goldberger, and FE Low. The Boltzmann equation and the one-fluid hydromagnetic equations in the absence of particle collisions. In *Proceedings of the Royal Society of London A: Mathematical, Physical and Engineering Sciences*, volume 236, pages 112–118. The Royal Society, 1956.

[12] N Yajima. The effect of Finite ion Larmor Radius on the propagation of magnetoacoustic waves. *Progress of Theoretical Physics*, 36(1):1–16, 1966.

[13] Al Macmahon. Finite gyro-radius corrections to the hydromagnetic equations for a Vlasov plasma. *The Physics of Fluids*, 8(10):1840–1845, 1965.

[14] G Sánchez-Arriaga. Structure of intermediate shocks in collisionless anisotropic Hall-magnetohydrodynamics plasma models. *Physics of Plasmas*, 20(10):102102, 2013.

[15] G Sánchez-Arriaga and E Siminos. Relativistic quasi-solitons and embedded solitons with circular polarization in cold plasmas. *Journal of Physics A: Mathematical and Theoretical*, 50(18):185501, 2017.

[16] A Balogh, To J Beek, RJ Forsyth, PC Hedgecock, RJ Marquedant, EJ Smith, DJ Southwood, and BT Tsurutani. The magnetic field investigation on the Ulysses mission-instrumentation and preliminary scientific results. *Astronomy and Astrophysics Supplement Series*, 92:221–236, 1992.

[17] SA Ledvina, Y-J Ma, and E Kallio. Modeling and simulating flowing plasmas and related phenomena. *Space science reviews*, 139(1-4):143–189, 2008.

[18] RG Littlejohn. Gaussian, SI and other systems of units in electromagnetic theory. http://bohr.physics.berkeley.edu/classes/221/1112/notes/emunits.pdf, 2016.

[19] Electromagnetism in Gaussian (cgs) units. http://www.physicspages.com/2014/11/06/electromagnetism-in-gaussian-cgs-units/.

[20] SJ Bame, DJ McComas, BL Barraclough, JL Phillips, KJ Sofaly, JC Chavez, BE Goldstein, and RK Sakurai. The Ulysses solar wind plasma experiment. *Astronomy and Astrophysics Supplement Series*, 92:237–265, 1992.